Investigating the initial condition of mantle models using data assimilation

Matthew Price

School of Earth and Ocean Sciences

Cardiff University

Submitted in partial fulfilment of the requirements for the degree of

Doctor of Philosophy

November 2016

ABSTRACT

Mantle convection models are computational models that utilise the equations defining the convective processes taking place in a terrestrial planet's mantle. Mantle circulation models (MCMs) are a subclass of mantle convection models that constrain mantle flow by imposing a boundary condition that uses plate reconstructions. Time dependent assimilation of plate velocities generates structures within the mantle that have been shown to correspond with present day Earth observations. Inferences of past mantle structures in MCMs are however more difficult due to the lack of initial condition for models. Without access to an initial condition for MCMs, pseudo initial conditions are used in MCM studies. MCMs therefore contain some error due to this uncertainty in initial condition. This thesis addresses the uncertainties in MCMs caused by the lack of knowledge of the initial condition, and attempts to improve the initial condition for Earth models.

Utilising perturbed twin experiments we show that assimilating plate reconstructions deters any chaotic growth over the assimilation period, minimising the influence of the initial condition at present day.

We also investigate and utilise advanced assimilation techniques that constrain mantle flow back in time, using a method known as an adjoint. Running a series of synthetic test cases using the adjoint we determine its efficiencies and effectiveness at constraining initial condition estimates. We find the adjoint is an excellent method for reconstructing initial conditions.

Using the adjoint, we conclude by running high resolution MCMs to construct initial conditions for differing viscosities, and compare these to the

standard method of obtaining an initial condition in MCM studies. We find that this yields mantle flow patterns markedly different from past studies, implying the adjoint can provide an alternate perspective for past mantle flow studies.

DECLARATION

This work has not been submitted in substance for any other degree or award at this or any other university or place of learning, nor is being submitted concurrently in candidature for any degree or other award.

STATEMENT 1

This thesis is being submitted in partial fulfilment of the requirements for the degree of PhD.

STATEMENT 2

This thesis is the result of my own independent work/investigation, except where otherwise stated, and the thesis has not been edited by a third party beyond what is permitted by Cardiff University's Policy on the Use of Third Party Editors by Research Degree Students. Other sources are acknowledged by explicit references. The views expressed are my own.

STATEMENT 3

I hereby give consent for my thesis, if accepted, to be available online in the University's Open Access repository and for inter-library loan, and for the title and summary to be made available to outside organisations.

Signed _____ (candidate) Date _____

Acknowledgements

Completing this doctoral research has been hard work, and *lots* of work, but has been an experience that I will cherish immensely. I have learnt so much throughout this journey and I would not be in the position of being able to submit my thesis without the help of many brilliant people.

First and foremost I have to thank my supervisor and friend, Huw Davies. The guidance and support he has given to me over the course of my PhD has helped me produce a thesis that I am proud to present.

I recognise the TERRA community for maintaining the base TERRA code. I also thank Ian Merrick for computer support at Cardiff and for getting me running back at the start of my PhD.

I acknowledge the role of Fujitsu, for making it possible for me to conduct this research through their financial support. I also thank the people behind HPC Wales, who have given me an enviable amount of usage of a HPC resource for this project. In particular I acknowledge the help of Ade Fewings for being understanding on the numerous occasions I filled entire disk spaces.

Within the Earth and Ocean science department at Cardiff I have made many life long friends who have provided fruitful discussions on so many things, including the occasional rock. My thanks go to my previous office companion Rebekah who helped me see the path to completing a PhD; as well as Josh, Kim, Miros; and to Bethan, Henry and Bob, for the many procrastinating tea breaks.

Closer to home are of course the people outside of work; Luke, Matthew, Pete and Yasmin, who helped me keep perspective.

I am of course thankful to all my family, for being there and for maintaining the pretence that they understood what I was talking about. In particular to my parents-in-law, Phil and Julia, for their time and effort in proof readings, and to my own parents for their constant support and encouragement.

Finally I wish to thank my best friend and wife Katherine. She has been my partner in this as with all things, sharing in my joy when things were going well, and providing support when things didn't go as planned. Thank you for keeping me on track and helping me get over the finish line.

To my uncle Roger, for inspiring
and encouraging me.

TABLE OF CONTENTS

List of figures

Chapter 1

Introduction

The planet we call home, Earth, is comprised of many complex systems that have arisen over the course of its existence. This body of work aims to contribute new understanding to one of these systems, mantle dynamics. In this introductory chapter we shall provide the context for our interest in this topic, together with the relevance of the subject to the larger research field. Before delving into the current state of mantle dynamics in particular, we begin with a brief primer on our planetary body of interest, Earth.

1.1 Earth

Earth formed from the coalescence of dust into small bodies - planetesimals, in the accretionary disk left after the formation of the Sun around 5 billion years ago. Eventually these pieces became large enough to exert their own gravity field. These planetesimals continued to gather together, experiencing ever more violent collisions as the sizes grew, resulting in the large molten mass of a planetary body we know as Earth. The densest materials in the volume sank and settled at the centre forming the metal core, whilst the lighter materials remained separate from this and began to cool forming the mantle. On top of this formed the crust, created from the cooled rock at the surface; the hardened exterior skin of our planetary body.

At present day these three layers remain: the crust, the mantle and the core. Of course as our understanding of the processes has grown, so too have further categories been made to accommodate the differences observed in these layers. In fig. 1.1 we see a cross section through Earth showcasing in detail these layers.

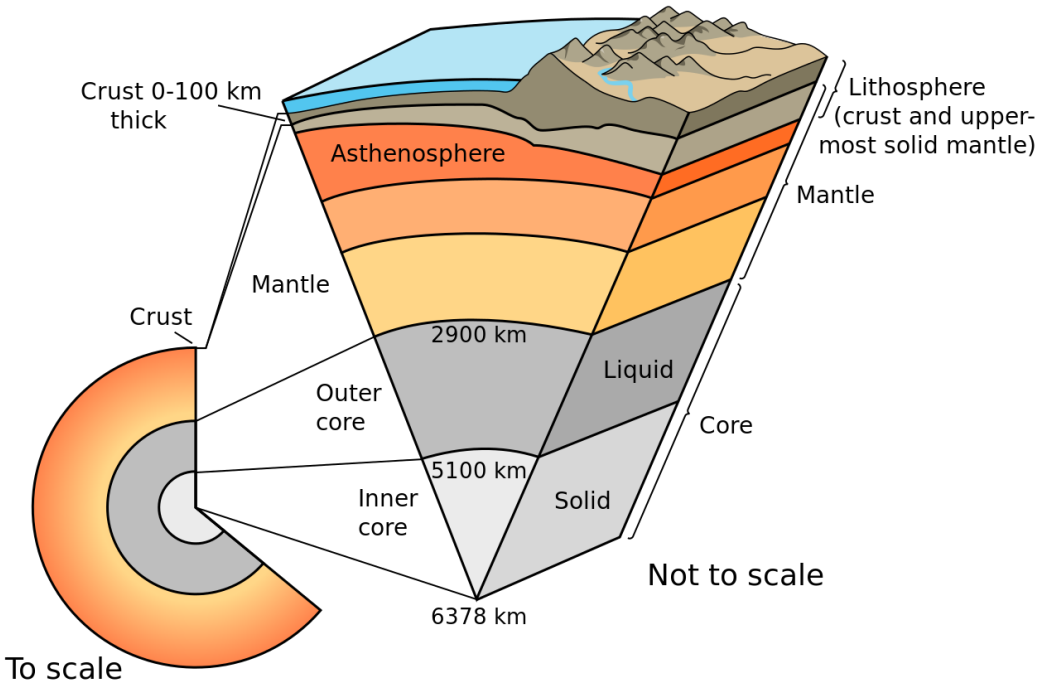

Fig. 1.1 The internal structure of Earth. Figure from *http://pubs.usgs.gov/gip/dynamic/inside.html*

1.1.1 The crust

The crust, the outermost layer and end product of differentiation of mantle convection constitutes less than half a percent of the total mass of the planet. Of the total radius of Earth ($\approx$ 6371 km), the crust extends 5 km to 50 km from the surface. The differences in crustal depth are attributed to the two different types of crust observed; continental and oceanic. Continental crust is the long lasting crust with a typical age of 2000 Myr. Due to these extreme ages, the continental crust has seen a range of geological processes and are an excellent source for understanding the planet's history. Oceanic crust is the crust formed at mid ocean ridges (MORs). This crust is denser than the continental crust and continues cooling after its formation, eventually becoming dense enough that it is recycled back into the mantle. Due to this fact, oceanic crust is many orders younger than the continental crust with typical ages of 80 Myr.

The process of creation and destruction of oceanic crust is part of a larger system known as plate tectonics. As the crust and the uppermost mantle form a mechanically strong outermost shell for Earth (approximately the top

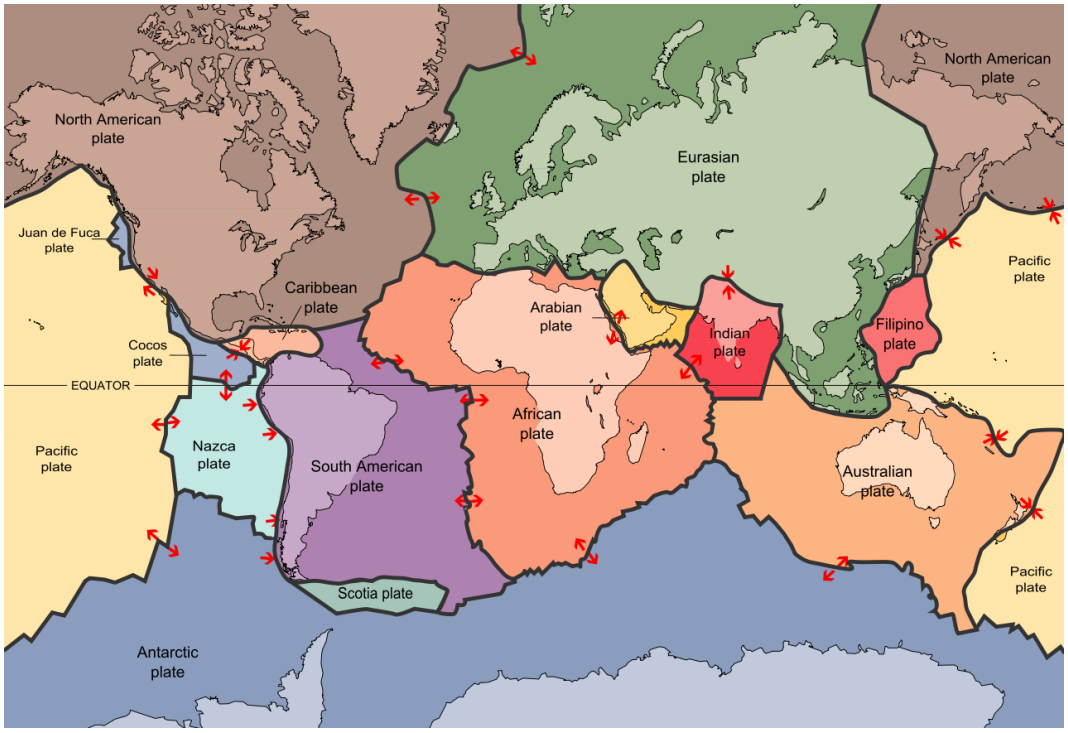

Fig. 1.2 The tectonic plates of Earth. Red arrows denote the direction of motion for the plate at the boundary. Figure from *http://pubs.usgs.gov/gip/dynamic/slabs.html*

100 km of Earth's radius), they can be grouped together as a single region. This region is known as the lithosphere, and it is here where plate tectonics occurs. Put simply, the idea of plate tectonics is that the lithosphere is split into a series of plates which are carried across the surface. This results in ever changing positions of the continents as they move together to form 'supercontinents', before breaking apart once more. The current arrangement of tectonic plates for Earth can be seen in fig. 1.2.

Where two or more plates meet is known as a plate boundary, and these can be categorised into three types.

1. Divergent - These boundaries are where two plates are moving away from one another and lithosphere is created. As these plates separate, hot material from below rises to the surface and cools generating new plate material. Divergent boundaries are most common at the MORs such as in the Atlantic.

2. Convergent - Plates that move towards each other form convergent boundaries, resulting in the loss of lithospheric material. Most often this occurs at the interface where oceanic and continental plates meet,

an example being where the Nazca and South American plates collide. Here the cooler, less buoyant oceanic material is forced down under the continental material in a process known as subduction. Alternatively two continental plates can collide, typically as a result of the end of oceanic plate subduction. An example of this would be the collision between the Eurasian and Indian plates following the closing of the Tethys ocean between them. In both instances, the collision of two plates results in significant surface expressions such as the Himalayas and the Andes.

3. Conservative - Named as such due to the fact that lithospheric material is neither destroyed (convergent) nor created (divergent). Instead, at this type of boundary the plates move parallel to one another, with the frictional forces between them a common source of earthquakes, with an example being the San Andreas Fault on the west coast of the USA.

As mentioned, these plates (consisting of the crust and uppermost mantle) sit on the underlying mantle, with the spreading and subduction of material from the lithosphere part of the large convective cells of mantle convection.

1.1.2 The mantle

The mantle extends from below the crust to a depth of 3480 km from Earth's centre, making up 84% of its volume and consisting of $\approx 70\%$ the mass. As there is no direct way to observe the mantle we rely on indirect observations to determine its structure and composition. Seismology, geodesy, numerical models, geochemistry and mineral physics experiments are all branches of Earth science that allow us to probe the mantle.

Analysis from these data sources reveals that the mantle is not a single uniform region but can be broadly broken down into the upper and lower mantle. The upper mantle is characterised by much less viscous flow ($\mathcal{O}(10^{21})$Pa s), whilst the lower mantle is much stiffer being orders of magnitude more viscous. Such high viscosities mean that at human timescales the mantle appears as a solid volume, however the mantle is deforming by a process of viscous creep. When viewed over geological timescales, the mantle is a highly convective body with a Rayleigh number (a non-dimensional measure of the strength of convection in a fluid) $\mathcal{O}(10^9)$. This translates to typical flow speeds of $5\,\mathrm{cm\,yr^{-1}}$ to $10\,\mathrm{cm\,yr^{-1}}$ with the convective cells that

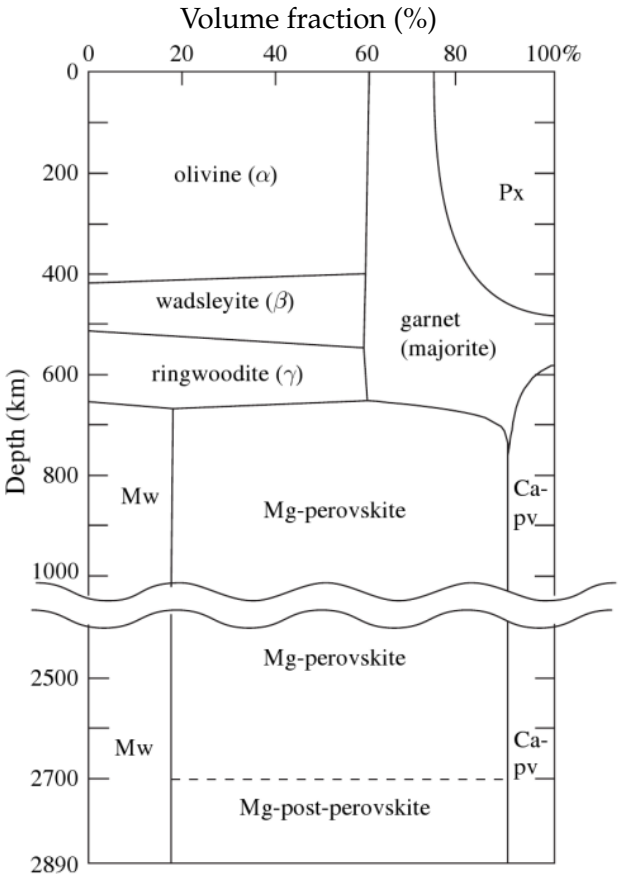

Fig. 1.3 The main mineralogical components of Earth's mantle for a pyrolitic mantle composition (Px – pyroxenes, Mw – magnesiowustite, Ca-pv – calsium silicate perovskite). Figure from Karato (2008).

form mantle convection linking with the plate tectonic boundaries (Davies 1999).

The upper mantle, as previously discussed, is linked with the crust at shallow depths forming the lithosphere. Directly below this is a region referred to as the asthenosphere, the very mobile layer which the lithosphere moves over. Beneath the asthenosphere, in the lower part of the upper mantle, we begin to see the effects of phase changes in the minerals, with two significant phase change boundaries located at 410 km and 660 km depth. These changes in mineral structure have been imaged by seismology, and replicated in lab experiments and are known to result in both density, and endothermic and exothermic changes as the minerals transition. Due to these phase changes, the region between 410 km and 660 km is typically referred to as the transition zone (Kennett and Bunge 2008).

Below this depth is the lower mantle, which is more homogenous than the region above it. There is however a final phase change boundary located near the base of mantle around 2700 km depth, as well as potentially chemically distinct reservoirs. Figure 1.3 highlights the main mineralogical phases in Earth for a single chemical composition model of the mantle, where we see the effects of the phase change boundaries at the various depths (Karato 2008).

Despite the major differences observed and expected in the mantle being radial due to increases in temperature and pressure, we also see lateral variations. These variations are linked with the convective cells of the mantle with the cold downwelling, and hot upwelling material resulting in lateral differences in densities and viscosities (Schubert et al. 2001).

The mantle is heated both internally from radiogenic decay and from the core beneath it. The internal heat is generated by the decay of a number of radioactive isotopes (predominantly isotopes of uranium, thorium and potassium), with half lives of the order 1 Ga to 10 Ga. Due to this radioactive decay, the total heat production of the Earth is decreasing. Roughly 3 billion years ago heat production was double the present rate, with the result that convection will have slowed over this period (Davies 1999).

At the mantle's base the interface with the core is known as the core-mantle boundary (CMB). It is near the CMB that seismological observations have picked out both Large Low Shear Velocity Provinces (LLSVPs) and ultra low velocity zones (ULVZ) rising off of the boundary (Garnero et al. 2016).

1.1.3 The core

The core occupies the region from Earth's centre to the CMB at 3480 km, making up the last 16 and 30% of the volume and mass respectively. It can be further separated into an inner and outer core, which are solid and liquid respectively as revealed by seismic studies. Because of the significant differences in outer core and mantle viscosities, the CMB is one of the most dramatic boundaries in Earth. The boundary between the inner and outer core, known as the inner core boundary (ICB), is located around 1200 km from the centre. This is thought to be expanding due to the solidifying of the outer core (Alfè et al. 2002).

The core plays a crucial role in the habitability of Earth thanks to the vigorous convection in the liquid outer core. This convection generates the

magnetic field that shields the surface from the charged particles of the solar winds and cosmic rays. This magnetic field has been observed to have flipped several times through Earth history as evidenced by the alternating magnetic pattern in the rock record. This observation can be used in reconstructing the plate tectonic movements (Müller et al. 2016).

1.1.4 Geodynamics

Geodynamics is the study of the dynamics of the mantle. Very simply it is concerned with understanding the driving force in the system, with the hot material rising and cold material sinking in the volume, not unlike the movement of material in a lava lamp. This process however is linked together with many other processes including: the rheological makeup of the material, changes in phases as materials experience different temperatures and pressures at depth, the chemical composition of materials and the coupling to surface processes like plate tectonics.

The mantle is a system with numerous complexities, with an active and exciting research field attempting to understand the processes that occur under our feet. To this end, investigations to improve the understanding of mantle processes occur with knowledge obtained through a number of avenues: from mineral physics based lab experiments, seismology, geodesy, geochemistry, and numerical modelling. In this work we take a particular interest in the computational experiments. These allow us, providing the underlying mathematical model is adequately defined, to explore mantle convection problems in detail and for a large parameter space. The only constraint on these models being the availability of computational resources.

Mantle convection models rely on describing the mantle as a fluid, with an appropriate equation set being outlined in Mckenzie et al. (1974), with the system being defined by the conservation equations for mass, momentum and energy. A number of sophisticated models have been developed that solve these equations and the many complexities predicted in both two-dimensions (with many recent models outlined in the benchmarking paper of Tosi et al. (2015)), and in three-dimensions. Particularly useful are the models which solve the equations in a spherical volume that attempt to capture the global effects of mantle convection. Models such as TERRA (Baumgardner 1985), CitcomS (Zhong et al. 2000; Tan et al. 2006), StagYY

(Tackley 2008) and ASPECT (Kronbichler et al. 2012) fall into this class of global mantle models.

These mantle convection models are like any other mathematical model; by providing an initial condition together with boundary conditions, the governing equations can be solved through time for a chosen numerical method. Results from these convection models are related back to the observations from other branches of Earth sciences, and it is the research linking the models and observations that we shall move on to explore in greater detail.

1.2 The present understanding in mantle dynamics

As we have previously mentioned, the mantle makes up 84% of Earth's volume, yet there are a number of areas of uncertainty in our understanding of this domain.

Despite being beneath the surface of Earth, thanks to seismic tomography we are able to image the many structures within the mantle. In brief, seismic tomography collates the seismic wave data and inverts this data to create a three dimensional image of the seismic velocities of Earth (see Liu and Gu (2012) for a comprehensive review). As these seismic waves are sensitive to the elastic properties of the medium they are travelling through, differences in density and temperature will affect the speed of the wave as it passes through the region. This in essence allows us to see the current convective structures in the mantle and reveals a great number of features that would otherwise be obscured from observation.

In fig. 1.4 we see some of the features imaged by one such shear wave tomography model, S40RTS (Ritsema et al. 2011). In this image the red regions correspond to seismically slower than average features. The large nature of these two slower than averages volumes, occupying an area consisting of 30% of the CMB and extending up to 1200 km above the CMB, has led rise to the term LLSVP when referring to them in the literature. A recent review into reconciling these observed features with our current understanding of mantle processes is available in Garnero et al. (2016).

There are currently many open questions regarding the LLSVPs in geodynamics, with possibly the most prominent one being whether they are

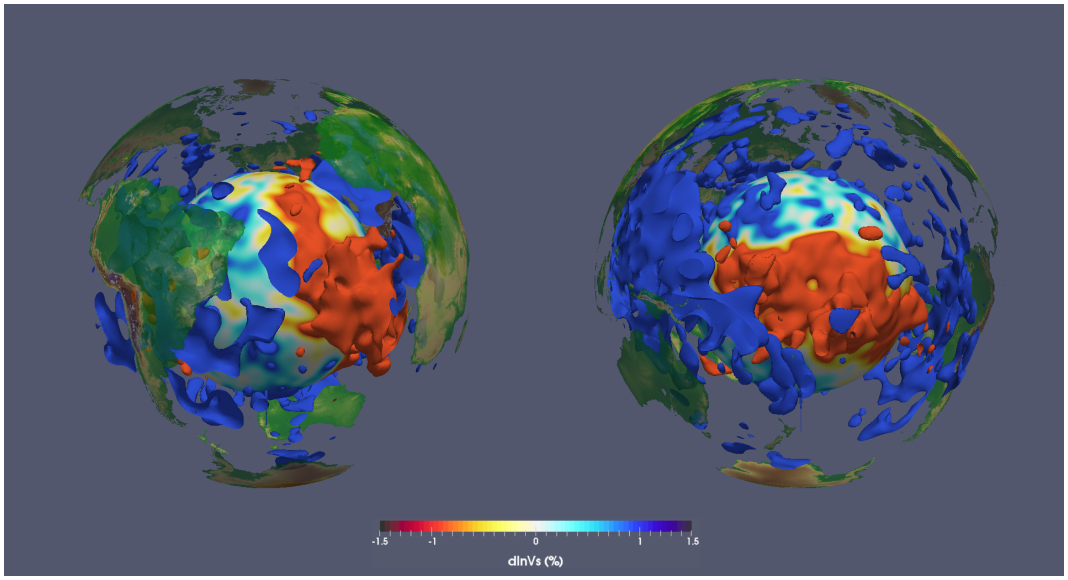

Fig. 1.4 A global view of shear wave seismic velocity perturbations (dV_S) in the S40RTS model (Ritsema et al. 2011), focused on the Atlantic (left) and Pacific (right). Images include a radial surface located at 2800 km with the ± 1 % dV_S isosurface, with positive anomalies not shown above 500 km depth and negative anomalies not shown above 1000 km depth.

thermal upwellings or thermo-chemically dense piles that have gathered in the region (see Davies et al. (2015a) and Deschamps et al. (2015) for two recent reviews). For purely thermal iso-chemical upwellings, it is not expected that these would be single, large 'megaplumes' as suggested in Thompson and Tackley (1998), but rather collections of finer plumes, which due to resolution limitations in the tomography are imaged as single large features (Schuberth et al. 2009a; Bull et al. 2009). While it has been argued that large thermo-chemical piles are not required for reconciling with the observed LLSVPs (Davies et al. 2012; Glišović and Forte 2015), a number of studies advocate the presence of thermo-chemical piles (McNamara and Zhong 2005; Bull et al. 2014). If these are thermo-chemical features, then their formation is also open for debate; they may be from a primordial reservoir, having formed from a differentiation event (Tolstikhin et al. 2006; Labrosse et al. 2007); or the material that they consist of has accumulated over time (Hirose et al. 1999; Brandenburg and van Keken 2007).

Further to these arguments for different makeups of these LLSVPs are a number of other open questions that can be explained by either a thermal or thermo-chemical explanation for LLSVPs. The longevity of the two masses as two distinct bodies has been investigated through the use of mantle cir-

culation models, and the likelihood of whether they could be created from a single large body (McNamara and Zhong 2005; Bower et al. 2013; Bull et al. 2014). Meanwhile the shape of the LLSVPs has been shown to be influenced by the plate motion reconstructions and the initial condition that is used (Zhang et al. 2010; Shephard et al. 2012a). We note that the plate reconstructions prior to 150 Ma are less well constrained due to the lack of paleomagnetic data, as there is little oceanic crust older which has not been subducted (Torsvik et al. 2008; Seton et al. 2012; Müller et al. 2016). This introduces some uncertainty in the results from studies that use plate reconstructions that extend beyond the Cretaceous period. Further linked to the nature of the LLSVPs structure is the question of any correlation between the large igneous provinces (LIPs) and volcanic hotspot locations at Earth's surface to the LLSVPs. Various studies have put forward arguments that these surface features are preferentially located above the margins of the LLSVPs (reinforcing an argument for a thermo-chemical composition) (Torsvik et al. 2006; Steinberger and Torsvik 2012), or that there is no preference to being located above their margins, and therefore not strengthening the case for thermo-chemical LLSVPs (Austermann et al. 2014; Davies et al. 2015b).

Also unveiled by seismic tomography is the presence of long since subducted material at both the plate boundaries and deeper into the mantle (denoted by the blue features of fig. 1.4). Subducted material is observed as a faster than average seismic feature, being colder denser material. These cold, narrow structures have been traced from the present day convergence zones of plate boundaries to a range of depths in the mantle; in some instances extending down to near to the CMB (van der Hilst et al. 1997), while in others it is seen to stagnate at the mid mantle phase transitions (Li et al. 2008; Fukao et al. 2009). The mixed observations of how subducted material transitions through the mantle emphasises that there are extra complexities within the mantle. Specific subduction studies have linked these differing types of subduction behaviour to the relationship between the age of the overriding and subducting plates (Garel et al. 2014).

Observations of Earth's gravity field equally highlight the structures seen in tomographic images, with gravity anomalies highlighting the varied distribution of mass in the mantle. Recent global gravity data obtained from the ESA satellite mission, GOCE (Johannessen et al. 2003), has been used by Panet et al. (2014) to construct maps of global gravitational gradients which match the features identified in tomography models. An expression of the

observed differences is to the dynamic topography (i.e. flow induced topography) of the crust; in essence a buoyant feature in the mantle will deflect the boundaries near it, either up or down depending on whether it is positively or negatively buoyant. Dynamic topography is used to describe the anomalous elevations observed that are not caused by isostasy. An example of this would be the positively buoyant African superswell (Lithgow-Bertelloni and Silver 1998), or the negatively buoyant western North Atlantic due to the previously subducted Farallon slab (Conrad et al. 2004) .

From data sources like the geoid it is possible to infer the complex rheological structure of Earth. While there is consensus on the overall average viscosity value across the mantle, $\mathcal{O}(10^{21})$Pa s (Haskell 1937), geoid data implies that the mantle also contains radial viscosity contrasts. While the long wavelength sensitivity of the geoid is more attuned to large features and the viscosity changes of the lower mantle, at finer length scales the presence of upper mantle material such as subducted plates is recognised within the data (Hager 1984; Panasyuk and Hager 2000; Forte and Mitrovica 2001; Rudolph et al. 2015). A number of studies have inverted geoid datasets to yield a radial profile for the viscosity structure of the mantle (Hager et al. 1985; Forte and Peltier 1991; Mitrovica and Forte 2004; Rudolph et al. 2015). Laterally, the mantle is also expected to have viscosity contrasts, though the effects of datasets such as the geoid are not significant (Moucha et al. 2007). A recent review collating current knowledge from both experimental and geophysical observations can be found in King (2016). Mantle convection models have also been conducted that cover the whole gamut of radial and lateral viscosities observed, with a variety of different rheologies seeing matches to present day observations (Bunge et al. 1996; Tackley 1996; Zhong et al. 2000; Glišović and Forte 2015). These various matches to observations, lead to further questions on our understanding of mantle rheology.

Considering the wealth of active areas of study in geodynamics, it is clear that a number of these research areas can be improved through better understanding of both the present, and the past, mantle flow. Gaining knowledge from the past mantle however is difficult as we recall that mathematical models need both initial and boundary conditions. Whilst we know our boundary conditions fairly well due to progress in plate reconstructions (Müller et al. (2016) for a review), we simply do not know what the initial condition for the past mantle flow is. Therefore any models of the mantle and conclusions made are borne from of an unknown and so must contain some error. It

has been shown that the assimilation of plate reconstructions constrains, and in fact helps, generate a mantle flow at present day that matches what others have observed (Bunge et al. 2002). Such methods however, cannot help estimations of the mantle flow at the models beginning. This initial condition issue has not gone unnoticed, and several attempts to address this problem through the use of various techniques have been made (Conrad and Gurnis 2003; Bunge et al. 2003; Liu et al. 2008; Ismail-Zadeh et al. 2009; Spasojevic et al. 2009; Shephard et al. 2010; Horbach et al. 2014; Glišović and Forte 2014).

Recognising the advantage of constraining our estimates of past mantle flow, and the initial conditions for mantle convection models, to addressing the current questions in geodynamics we can now begin to focus our research. To this end, we consider these questions when framing the work to be conducted in this thesis.

How accurate are our current methods of calculating mantle flow?

First, we must consider how accurate our current methods of mantle modelling are and is there any sensitivity to how these models are initiated. Having established this we can then go on to consider our second question:

In what ways can we better constrain our understanding of past mantle flow?

As we have outlined, there are numerous present day observations of the convective flow in the mantle, yet standard methods do not allow us to use this information to better understand mantle flow in the past. We therefore endeavour to investigate potential methods to overcome this disconnect, and that allow us to feed our extensive present day knowledge into our mantle models to infer past flow. By investigating such methods we then turn our attention to attempt to address some of these issues with our third question:

Are these methods an improvement over current techniques in helping understand current questions in geodynamics?

By developing a method that utilises the wealth of data available to us for present day mantle observations, we have to ask does such a method have any merit compared to standard mantle modelling practices.

1.3 Thesis outline

The body of work presented in this thesis follows a natural path towards addressing these questions raised. While each chapter forms a part of the larger narrative of this thesis, each is self contained and can be read independently of one another. There is therefore some small repetition as methods are outlined in each chapter.

To begin, in Chapter 2 we present an introduction to the methods that form the background of mantle convection and mantle circulation modelling. We detail the equations that govern the dynamics of the mantle, together with the computational code used to model this system, TERRA. A discussion of how these models can be related to Earth, through the use of data assimilation of reconstructions of past plate motions to generate structures similar to Earth; as well as what and how we can convert and compare the final output from these models in order to validate results. We conclude our introduction to mantle modelling by presenting an example of a typical mantle model. This is started from a guessed initial condition and then progressed to present day, whilst assimilating 200 Myr of plate motion histories. The final output from this model is then compared to a tomographic model noting the similarities and differences between them.

Following this introduction to mantle modelling, in Chapter 3 we begin by investigating how discrepancies in the mantle modelling process may affect the final outputs, with an aim to address our first question of how accurate current methods are. Previous work has shown that even small differences in the initial condition for a mantle convection model can influence the final solution due to the chaotic nature of convection. We therefore look to apply the theory of error growth to models that assimilate a known surface boundary condition, such as you might find with plate reconstructions, in order to test whether this constrains the error growth from differing initial conditions.

Having demonstrated that through assimilating a known surface boundary we can constrain the error growths from differing initial conditions, we address our second question regarding how to constrain our understandings of past mantle flow, by investigating how the initial condition itself can be constrained. To this end, in Chapter 4 we discuss potential methods of incorporating the wealth of Earth observations available, in order to achieve

a more informed initial condition for our models. We present in detail the concept of an adjoint model, a method that assimilates known present day information, and how it can be implemented into the forward modelling process employed thus far in this thesis. A detailed guide on the computational process is discussed, as no such source of information is available in the current literature. With the adjoint method implemented in TERRA, we finish this chapter with a small synthetic test case in order to verify that the iterative forward-adjoint process can reconstruct past mantle structure.

With the positive results obtained for our forward-adjoint test case, in Chapter 5 we begin a more robust profiling of the method. While some pieces of the adjoint method for mantle convection have been looked at in other studies, we look to build on this work in this chapter through the use of additional tests that use synthetic data. Due to the computational expense required to run forward-adjoint models, we look at potential places where efficiencies can be made in the method that do not alter the convergence of solutions. We also use the availability of 200 Myr of plate reconstructions together with the forward-adjoint method to determine over what time intervals the method performs to an acceptable standard.

With our aim to improve the initial condition of mantle models relevant to Earth, incorporating real Earth data when performing the adjoint calculation is a necessity. Therefore, we move on from our synthetic models of the previous chapter and look to incorporate shear wave tomography in our models in Chapter 6. Because of the resolution differences between mantle models and tomographic models in this chapter we investigate differing methods of comparing these two datasets, looking in detail how this affects the convergence of any solutions.

We conclude our research in Chapter 7, where we look to combine all the information we have found thus far in this thesis, and by applying it to high resolution forward-adjoint models, observe any differences between adjoint derived initial conditions and classic initial conditions. To understand how the two types of initial conditions alter mantle flow patterns, we construct MCMs with different viscosities that use these two types of initial condition. By monitoring the two different models we hope we can answer the final question of whether the adjoint method improves our understanding of Earth based problems.

The final chapter in this work (Conclusions), summarises the main results of the thesis, reviewing these in the context of the plan lain out in the introduction.

At the end of the thesis are a number of appendices that include: a glossary of common terms (Appendix A); a detailed derivation of the adjoint equations for incompressible flow (Appendix B), together with the adjoint equations for compressible flow (which are not considered in this thesis), as well as musings on how the adjoint method may be used for thermochemical models.

All code advancements from the base TERRA code required for this thesis, including the implementation of the adjoint equations and workflow as outlined in chapter 4, and code required to run the twin experiments of chapter 3 have been implemented myself.

CHAPTER 2

METHOD - MANTLE MODELLING, DATA ASSIMILATION & TERRA

2.1 Introduction

Before presenting the findings of this thesis, we will first give a short overview detailing the methodology involved in modelling the mantle convection both in general, and how this can be related to the case of convection in the Earth. First we will present a brief outline of the mathematical equations that define convection, leading into the details of the computational code used in this study. Following this an outline of how we relate our models to the Earth by conditioning the models with plate reconstructions, together with how we can then validate our results to the Earth is described. To finish we then present an example of a mantle model from start to finish, to allow the reader to view the entire process.

2.2 Mantle convection modelling - The numerical formulation

The mathematical formulation for mantle convection involves the equations for conservation of mass, momentum and energy prescribed in a spherical shell with an upper boundary S and lower boundary C with the mantle contained in the volume V with boundaries $\partial V = S \cup C$. As the convection is time dependent, the equations apply over a time interval $I = (t_0, t_1)$. So for $x \in V$, $t \in I$ the following equations prescribe mantle flow (Jarvis and Mckenzie 1980).

Firstly mass conservation is ensured by

$$\frac{\partial \rho}{\partial t} + \nabla \cdot (\rho \boldsymbol{u}) = 0, \tag{2.1}$$

where $\boldsymbol{u}$ denotes the fluid velocity and ρ the density. The time dependency in this equation can be set to zero. This is because changes in the mantle density over short time scales are represented as seismic waves, and so are not considered a solution to the equation on the time scale of mantle convection. Thus we arrive at the anelastic approximation for the conservation of mass:

$$\nabla \cdot (\rho \boldsymbol{u}) = 0. \tag{2.2}$$

Conservation of momentum ensures the balance of the buoyancy and viscous forces present in the mantle. This is described mathematically as

$$\nabla \cdot \sigma + \Delta \rho \boldsymbol{g} = 0, \tag{2.3}$$

with $\Delta\rho$ being any density anomalies and $\boldsymbol{g}$ the gravitational acceleration. σ denotes the stress tensor which can be broken down to the deviatoric and non-deviatoric stresses

$$\sigma = \tau - P\mathbb{I}. \tag{2.4}$$

P is the non hydrostatic pressure giving the non-deviatoric stress and τ is the deviatoric stress relating the stress field to the velocity, which assuming a Newtonian fluid the constitutive equation is

$$\tau = \eta \left\{ \nabla \boldsymbol{u} + (\nabla \boldsymbol{u})^T - \frac{2}{3}\mathbb{I}(\nabla \cdot \boldsymbol{u}) \right\} \tag{2.5}$$

where η is the dynamic viscosity. With both eqs. (2.4) and (2.5) we can then expand the general definition of our momentum equation eq. (2.3) to obtain

$$\nabla \cdot \left(\eta \left\{ \nabla \boldsymbol{u} + (\nabla \boldsymbol{u})^T - \frac{2}{3}\mathbb{I}(\nabla \cdot \boldsymbol{u}) \right\} \right) - \nabla P + \Delta \rho \boldsymbol{g} = 0 \tag{2.6}$$

Equation (2.6) then relates the balance of forces (reading from left to right) between viscosity, pressure and buoyancy.

Considering the conservation of energy in the system introduces the time dependency in the mathematical formulation of mantle convection.

Conservation of energy is described as

$$\frac{\partial T}{\partial t} + \boldsymbol{u} \cdot \nabla T + \gamma T \nabla \cdot \boldsymbol{u} - \frac{1}{\rho c_V}(\tau : \nabla \boldsymbol{u} + \nabla \cdot (k \nabla T)) - H = 0, \tag{2.7}$$

where T is the temperature, γ is the Grüneisen parameter, k is thermal conductivity, H is radiogenic heat production and c_V is the specific heat at constant volume.

Equations (2.2), (2.6) and (2.7) are therefore our set of equations that describe compressible mantle flow.

Furthermore there are some simplifications which can be made to our full set of compressible equations, which we will briefly detail also.

If we assume that the mantle is incompressible, that is the volume does not change with changes in pressure and temperature, then the divergence of the velocity can be set to zero such that

$$\nabla \cdot \boldsymbol{u} = 0. \tag{2.8}$$

We see this term appear a number of times across our compressible equations eqs. (2.2), (2.6) and (2.7), all of which vanish under this assumption.

Furthermore we can employ a number of equation of state approximations. If we assume a Boussinesq equation of state then we have

$$\Delta \rho = \alpha \rho (T_{\text{av}} - T), \tag{2.9}$$

where α is the coefficient of thermal expansion and T_{av} the reference radial temperature profile, which then assumes that density is held constant other than in the buoyancy term of the momentum equation.

We can therefore obtain the simplified set of equations eq. (2.10) for mantle convection

$$\nabla \cdot \boldsymbol{u} = 0 \tag{2.10a}$$

$$\nabla \cdot \left(\eta \{ \nabla \boldsymbol{u} + (\nabla \boldsymbol{u})^T \} \right) - \nabla P + \alpha \rho (T_{\text{av}} - T) \boldsymbol{g} = 0 \tag{2.10b}$$

$$\frac{\partial T}{\partial t} + \boldsymbol{u} \nabla \cdot T - \kappa \nabla^2 T - H = 0, \tag{2.10c}$$

where $\kappa = k / c_V \rho$ denotes thermal diffusivity. Assumptions on the viscosity structure of the mantle (such as thermal, radial or constant) can vary the level of complexity of the system of equations needing to be solved.

Of course initial (eq. (2.14)), and boundary (eqs. (2.11) to (2.13)), conditions are required in order to obtain a particular solution using these equations. The mantle has two boundaries: at the bottom where it contacts the outer core C, and at the top where the surface touches the crust S. Since the length scales of the crust are small compared to the mantle we typically include this as a part of the mantle in our models and assume the top boundary is at the surface or the Earth.

For the velocity field at the CMB, a good approximation of the flow behaviour is to assume there is no shear stress; this is due to the very low viscosity of the liquid metal in the outer core. Therefore we prescribe a free-slip boundary condition (eq. (2.11a)), which sets the tangential component of the shear stresses to zero,

$$\left(\left(\nabla \boldsymbol{u}(x,t) + (\nabla \boldsymbol{u}(x,t))^T - \frac{2}{3}\mathbb{I}(\nabla \cdot \boldsymbol{u}(x,t))\right) \cdot \boldsymbol{n}(x)\right)_{tan} = 0 \quad x \in C,\ t \in I \tag{2.11a}$$

where $\boldsymbol{n}$ is the normal vector. At the surface boundary we can apply the same boundary condition. However, we can also make use of the knowledge of plate motion histories as a kinematic boundary condition to allow our models to better capture Earth dynamics. To do this we assign the relevant tangential velocities described in a plate motion model, $\boldsymbol{u}_P$ at the surface boundary,

$$\boldsymbol{u}(x,t) = \boldsymbol{u}_P(x,t) \quad x \in S,\ t \in I \tag{2.11b}$$

We also apply the no-penetration condition on the flow to ensure there is no radial flow at either boundary,

$$\boldsymbol{u}(x,t) \cdot \boldsymbol{n}(x) = 0 \quad x \in \partial V,\ t \in I. \tag{2.11c}$$

In reality the situation is slightly more complex, as the boundary is not fixed but also allows vertical movement (for example the building of mountain ranges show this). However, due to the length scales of our models ($\mathcal{O} \sim$ 3000 km) we ignore this.

For the pressure field, due to the gradient of P we prescribe the following boundary condition at the surface

$$P(x,t) = 0, \quad x \in S, t \in I. \tag{2.12}$$

For the temperature field we assign a value at the two boundaries S and C;

$$T(x,t) = T_S(x,t) \quad x \in S,\ t \in I \tag{2.13a}$$
$$T(x,t) = T_C(x,t) \quad x \in C,\ t \in I \tag{2.13b}$$

together with an initial condition that we prescribe for the whole temperature field

$$T(x,t_0) = T_0(x) \quad x \in V. \tag{2.14}$$

It is in (2.14) that the main obstacle in mantle convection codes is found, as there are simply no measurements for the temperature structure of the mantle back through time (Bunge et al. 2003).

2.3 TERRA, a three-dimensional, spherical mantle convection code

2.3.1 Background

A number of codes exist that solve the system of equations governing mantle convection; such as CitcomS (Zhong et al. 2000; Tan et al. 2006) , ASPECT (Kronbichler et al. 2012), StagYY (Tackley 2008). The code that will be used for this project is TERRA, which was originally the work of Baumgardner (1985).

Since its inception it has seen many noticeable improvements. The first main improvement was being parallelised (Bunge and Baumgardner 1995), overcoming the limitations of single processor machines. Sharing the problems over many processors results in improved computational speed for problems at more realistic resolutions with greater accuracy.

Following this, variable viscosity (both temperature and pressure dependent) was introduced into the code (Yang 1997) Due to the inferences from

many areas of earth science on the structure of the mantle, this was a crucial addition.

The assimilation of plate motion history models as a kinematic surface boundary condition has also been incorporated into TERRA (Bunge et al. 1998). Whilst this does not account for lithospheric deformation, it nonetheless allows a generic convection model to accurately recreate the large scale tectonic features that have formed the unique structure of Earth's mantle. Models using these boundary conditions are referred to as mantle circulation models as opposed to mantle convection models.

Finally, tracer particles which allow models to consider thermo-chemical convection in the mantle are also available (Stegman et al. 2002). This allows investigations into the geochemical nature of the mantle to be undertaken; an area that is currently of significant debate.

TERRA has been benchmarked to ensure accuracy (Davies et al. 2013). These improvements leave TERRA as a highly capable mantle convection code, that can approach any number of current problems in the geodynamics community.

2.3.2 The TERRA grid

The TERRA grid has remained unchanged since its inception. Within this thesis we concern ourselves only with the main details of the grid structure to aid understanding the scalability and increase of resolution and demands of the code. A full description of the grids discretisation and indexing may be found in both Baumgardner (1983) and Baumgardner and Frederickson (1985).

An ideal grid for a given computation would consist of as near to equal area as possible discretisation of the domain. In TERRA the sphere is initially discretised by projecting a regular icosahedron onto the sphere such that the twelve vertices of the icosahedron define the base grid constructed of twenty equal triangles; i.e. fig. 2.1a. These twenty triangles can also be thought of as ten diamonds, with each diamond containing one of the triangles with a vertex located at one of the poles. With this simple grid in place, further refinements to the grid are easily achieved by joining the midpoints of the sides of each triangle with geodesic arcs, creating four smaller triangles. This process of refinement can be be repeated to obtain any resolution and allows the grid to remain virtually uniform irrespective of how fine the resolution.

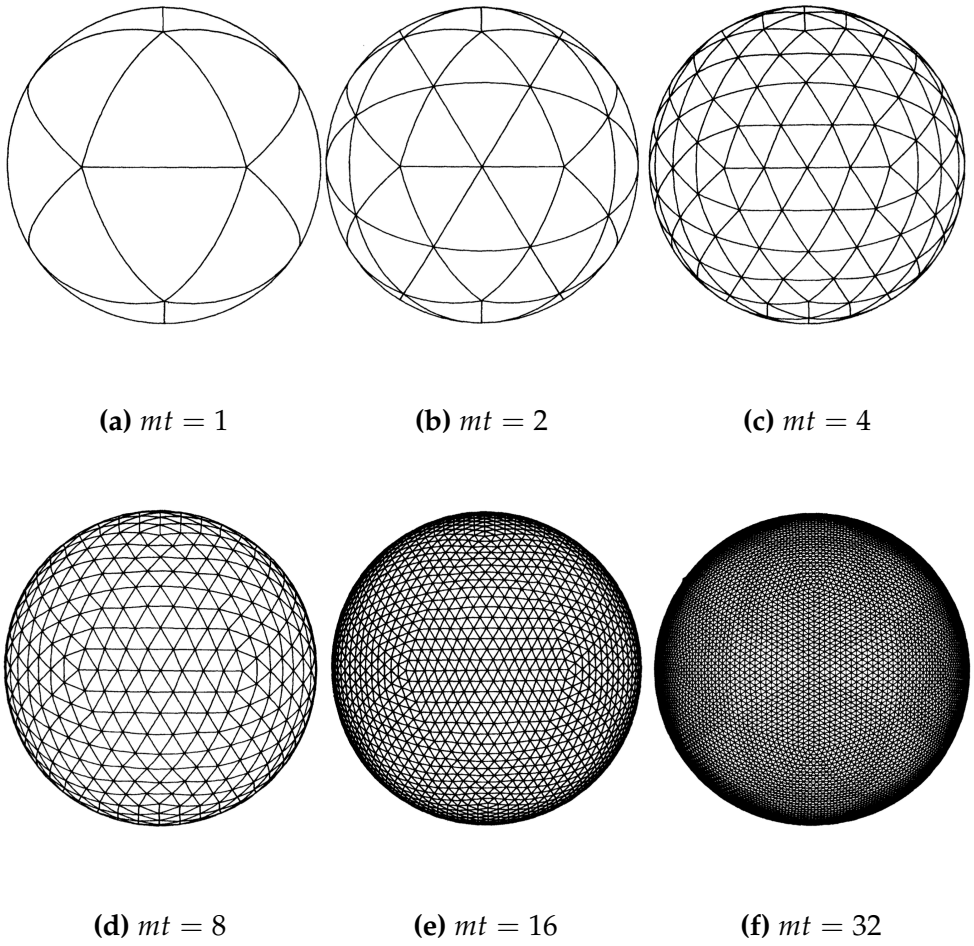

(a) $mt = 1$ **(b)** $mt = 2$ **(c)** $mt = 4$

(d) $mt = 8$ **(e)** $mt = 16$ **(f)** $mt = 32$

Fig. 2.1 (a) The TERRA grid created from projecting an icosahedron onto a sphere. (b)-(f) successive refinements for mt.

Also an advantage for this type of grid discretisation is that it does not suffer from an over sampling of points on the poles that can occur with rectangular grids projected onto the sphere.

The parameter that defines the number of refinements to the basic grid is known in TERRA as $mt = 2^k$, $k \in \mathbb{N}$; an example of the first few refinements can be seen in fig. 2.1.

To extend the mesh radially so that it encompasses the three dimensional domain of the sphere we simply repeat the spherical mesh at different radii from a central coordinate. The result is a volume discretised by cells that are triangular prisms that have spherical ends.

The choice in how many radial layers to use is dictated by the parameter nr. The choice in nr however, should ideally create finite element cells that

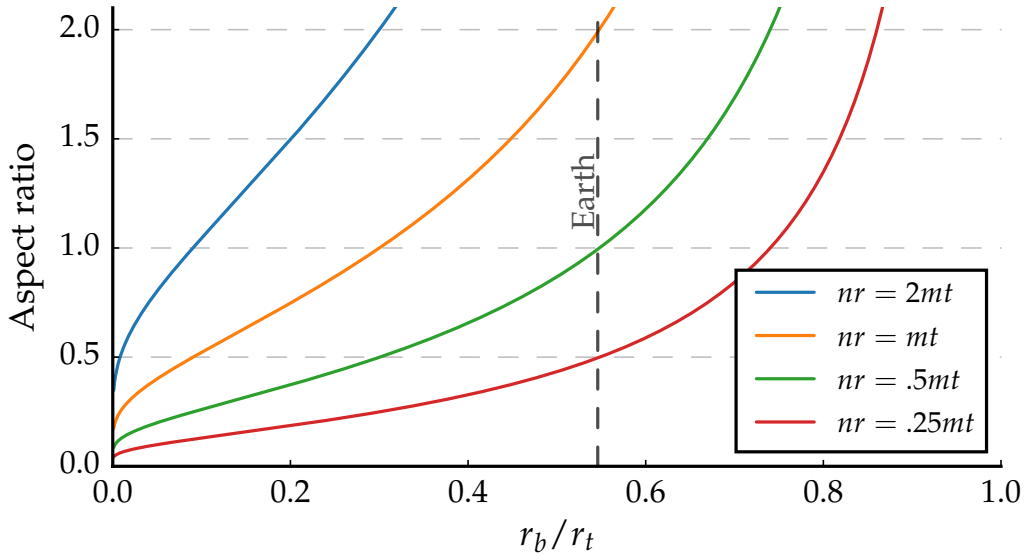

Fig. 2.2 Aspect ratio of finite element cells vs. inner/outer radius ratio r_b/r_t for different nr/mt values, where $mt = 512$. The ratio $r_b/r_t \approx 0.546$ for the Earth is highlighted. Reproduced from Yang (1997).

have an aspect ratio as near to 1 as possible as discussed in Yang (1997). Figure 2.2 shows various choices of nr for different factors of mt. From this it can be seen that the ideal choice of nr for the Earth to achieve an aspect ratio of 1 would be $nr = \frac{1}{2}mt$.

With both choices in mt and nr defined the number of nodes can be found. Each shell contains $10mt^2 + 2$ nodes and $nr + 1$ radial layers of shells. Table 2.1 shows how an increase in mt translates to both the total size of the problem being solved and the refinement in the resolution of the grid.

2.3.3 Computational requirements

The computational resources required by TERRA depend on a number of factors. The number of processes required for a model depends on the value given by the following formula:

$$\#\,\text{proc} = \left(\frac{mt}{nt}\right)^2 \frac{10}{nd} \tag{2.15}$$

where $mt = 2^m$, $nt = 2^n$ with $m \geq n$; $m, n \in \mathbb{N}$ and $nd = 5$ or 10. nt, is the number of grid intervals along the edge of a local subdomain (a division of

mt	# global nodes	Average lateral spacing (km)		Radial spacing (km)
		Surface	CMB	
16	23,058	479.4	261.9	361.2
32	174,114	239.8	131.0	180.6
64	1,351,746	119.9	65.6	90.3
128	10,649,730	59.9	32.7	45.2
256	84,541,698	30.0	16.4	22.6
512	673,710,594	15.0	8.2	11.3
1024	5,379,195,906	7.5	4.1	5.6

Table 2.1 Growth and refinement of the TERRA mesh used when modelling the Earth

each diamond) and *nd*, the number of diamonds from which subdomains will be mapped onto the processors.

Problems for $mt \leq 64$ therefore can take between 1 and 16 processes to run, amounts that are not uncommon in current desktop hardware. These problems therefore run with relative ease locally, whereas these values were at the limit of computational power when TERRA was first introduced (Baumgardner 1985). Current global mantle models typically run at resolutions that translate to a TERRA *mt* values in the range of $256 \leq mt \leq 512$ (Schuberth et al. 2009b; Davies et al. 2012; Bower et al. 2013). Models achieving a resolution of this order will typically require from 128 to 512 processors, and so currently require high power computing (HPC) resources.

Of course running at these high resolutions does come with some restrictions. The Courant-Friedrichs-Lewy (CFL) condition limits the time stepping of the model such that the flow speed does not exceed half a grid cell per time step to prevent calculations from becoming unstable. Since the size of the cells reduces as the grid is refined, this has a secondary effect of reducing the length of each time step to ensure the CFL condition is held. Therefore a single increase in *mt* will result in requiring 2^3 (since each grid cell is halved in size in three dimensions) $\times 2$ (since the time step is halved) longer to run.

Another effect of refining the grid is that the total number of data points increases by the same 2^3 value. This can put a strain on storage if not careful, as coupled with the longer run times the increased storage requirement for one step in resolution can quickly swamp disk space with 10 GB to 1000 GB of output data.

However, despite these negatives there are obvious benefits to the increased resolution. First and foremost, the finer resolution allows mantle features to be resolved to a much finer degree; far beyond any tomographic models. The finer grid spacing also allows reference viscosities much closer to those predicted for the Earth to be prescribed, as well as more complex radial and lateral viscosity profiles to be set.

2.3.4 HPC Wales

As discussed previously, high resolution MCM models will require the use of HPC facilities in order to perform the computations. For this project we make use of the HPC Wales computing facility, which is Wales' national supercomputing service provider. It is host to the UK's largest distributed general purpose supercomputing network, a 17,000 core, 320 Tflop capacity system.

The system consists of the main two large computer hubs in South Wales, together with a number of Tier 1 and Tier 2 sites at Universities and business centres across Wales. These hubs are all connected by a dedicated network featuring a 10 GBit/sec link between the main hubs, and 1 GBit/sec and 100MBit/sec links connecting the lesser sites.

This project predominantly makes use of the computing resources available on the flagship hub systems; located in Cardiff and Swansea.

2.3.5 Solution scheme

With the equation set (e.g. eq. (2.10) for incompressible flow) defined, the basic strategy for solving the set of equations as computed in TERRA is:

1. Compute the pressure field from the density and temperature fields via the equation of state

2. Solve the equations for conservation of mass and conservation of momentum simultaneously for $\boldsymbol{u}$ and P.

3. Solve equation for conservation of energy for the rate of change of T.

4. Take a time step and update the density and temperature fields.

A detailed explanation on the technical setup of TERRA is beyond the scope of this work, whilst being covered extensively in other work so is not

included here. If the reader requires further information on topics including; the underlying indexing of the numerical grid; a derivation of the discretised Galerkin finite element formulation; the computational operators in terms of the finite element shape functions; a detailed description of the solution strategies; an explanation of the time stepping strategies employed; how parallelisation of the problem translates to the TERRA grid; then they are encouraged to consult the theses of both Baumgardner (1985) and Davies (2008, Appendix E).

2.4 Data assimilation of plate motion histories

In the mathematical outline for mantle convection in section 2.2 we detailed that the surface boundary condition for the velocity can be prescribed as plate motion histories (eq. (2.11b)) by means of data assimilation. By assimilating the tectonic reconstructions of Earths surface, a convection model can replicate features across the mantle that are seen in seismic tomography observations (Bunge and Davies 2001; Bunge et al. 2002; McNamara and Zhong 2005; Shephard et al. 2012a). These range across all the main features seen in the mantle; the Large Low Shear Velocity Provinces (LLSVPs), subducting and subducted slabs (e.g. Farallon) and a range of mantle plumes and hotspots.

Plate motions are incorporated into TERRA by assigning values at the surface layer of the computational grid, applied in discrete stages. TERRA has two ways of handling the plate velocities. The first is by breaking the plate reconstruction into a number of plate stages based upon important geological changes. One such plate reconstruction used in TERRA is the Lithgow-Bertelloni and Richards (1998) plate reconstruction that was used in Bunge et al. (1998). This reconstruction consists of 11 discrete plate stages spanning 120 Myr, where each stage consists of a discrete number of plates with their motions defined by a rotation vector and its magnitude. A caveat of this setup is the large time period between plate stages ($\mathcal{O}$ ∼15 Myr) can result in large jumps in plate boundaries instantaneously when plate stages update. This can be countered by linearly interpolating between plate stage rotation poles of successive plate stages. An unwanted effect of interpolating is the plate boundaries can become ill defined, with the expected sharp edged boundaries between plates becoming broad regions.

Alternative to this, the plate reconstruction velocities used in TERRA can be uniquely defined at each grid point using the GPlates package, an open-source, interactive tool for plate reconstructions (Boyden et al. 2011; Cannon et al. 2014). GPlates allows the user to construct plate motion models that contain evolving and intersecting plate boundaries which separate Earth's surface into discrete plates throughout the geological time frame (Gurnis et al. 2012; Seton et al. 2012; Zahirovic et al. 2015). An advantage of this setup is that the plate stages are defined by default over a regular and finer time period (1 Myr intervals) with no issues with plate boundaries as velocities are assigned to each node. Plate files generated in this way however, lack the portability of the previous method. This is because since the plate files are assigned at each node, a change in the model discretisation (changing nt or nd, whilst keeping mt the same) which changes the number of processes used, will require a new set of plate files regardless of keeping the resolution fixed. This therefore requires a non-trivial amount of disk space to store each set of plate files (4 GB for a 200 Myr $mt = 256$ model). The number of files can create issues interacting with them using a command line interface.

Since the aim of this study is to improve the TERRA models predictions of the Earth, the choice of plate reconstruction is key, and next we shall discuss the choice of plate reconstruction used in this work.

2.4.1 The Seton et al. (2012) plate reconstruction

The plate motion model of Seton et al. (2012) is a global set of continuously closing topological plate polygons with the associated plate boundaries and velocities, based on the method outlined by Gurnis et al. (2012); spanning from the breakup of Pangea (200 Ma) to present day (fig. 2.3).

Briefly, the model uses plate motions found from reconstructing the spreading history of the seafloor using gravity and magnetic anomaly data to construct seafloor spreading isochrons for each major oceanic plate. To account for oceanic crust from plates that has since been subducted over the 200 Myr, evidence of subduction, slab windows and anomalous volcanism from onshore geology, and the rules of plate tectonics is used in line with the approach of Muller et al. (2008). Finally the model utilises a hybrid absolute reference frame; for 100 Ma to present the reference frame is based on a moving Indian/Atlantic hotspot model (O'Neill et al. 2005), and for the 200 Ma to 100 Ma period a true-polar wander corrected paleomagnetic

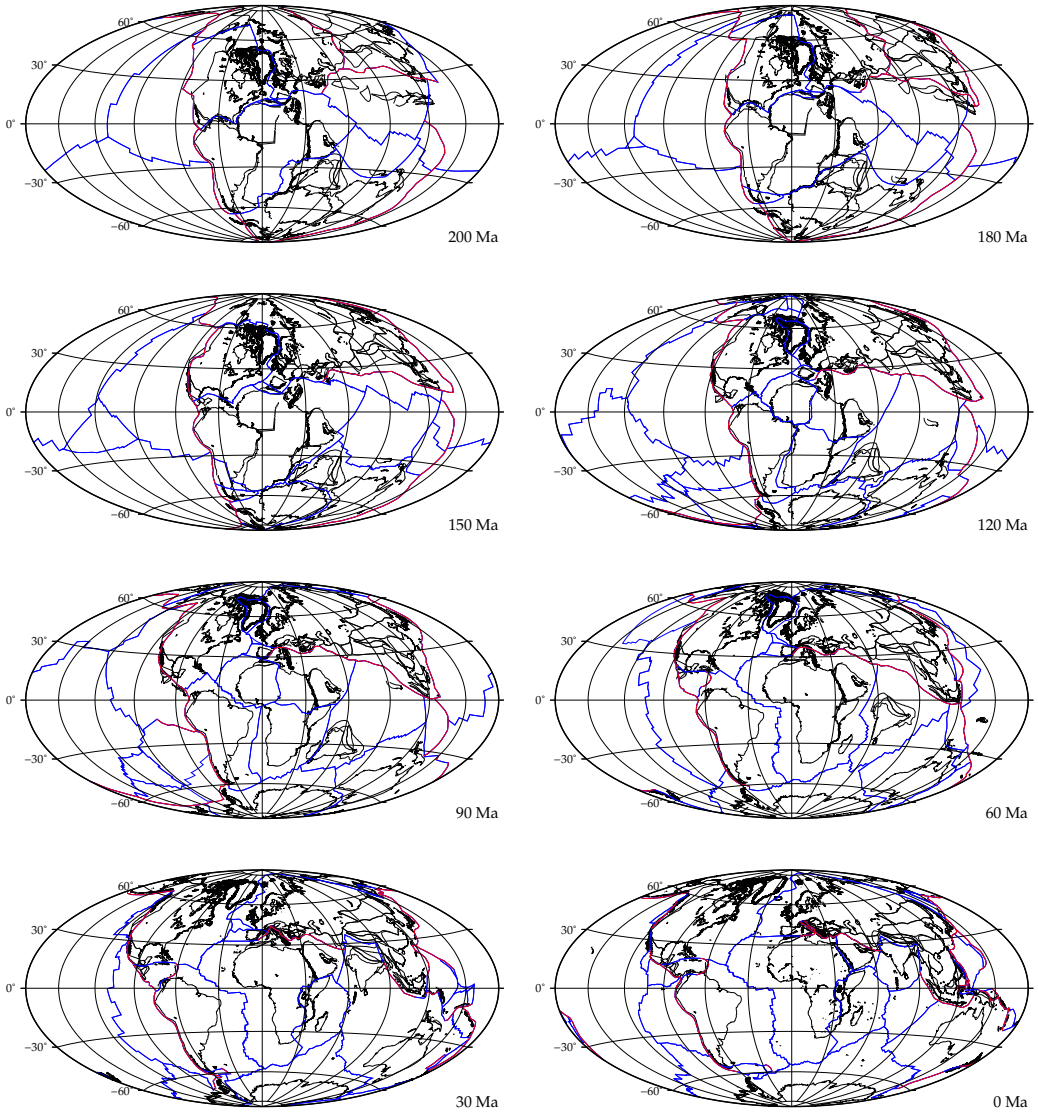

Fig. 2.3 Snapshots of the plate tectonic reconstruction from Seton et al. (2012). Coastlines (black), ridges and transform faults (blue) and subduction zones (red) are included for geographic reference.

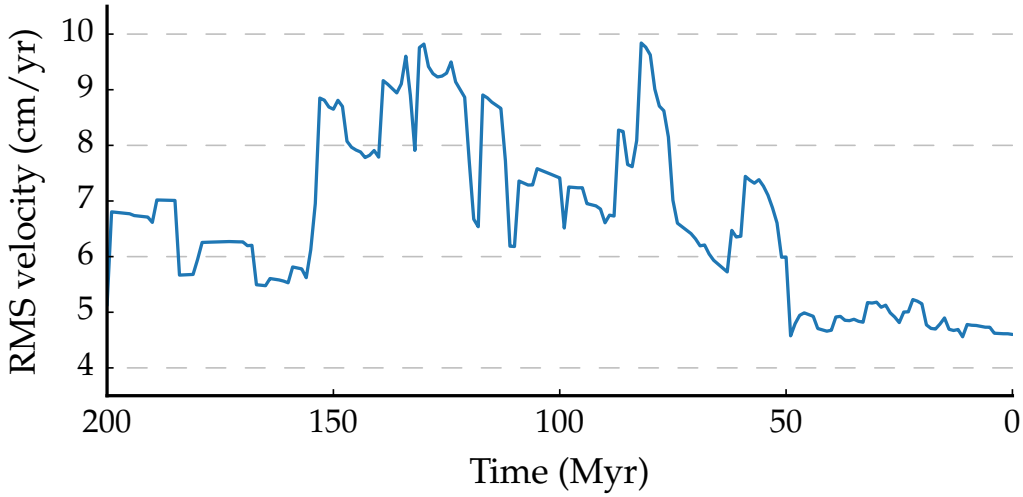

Fig. 2.4 Global plate RMS velocities of the Seton et al. (2012) plate motion model.

model is used (Steinberger and Torsvik 2008). Combining all this results in a set of dynamically closed plate polygons spaced at 1 Myr intervals which continually evolve thanks to the computed dynamic plate boundaries. For a full detailed explanation on the data methods used to construct this model the reader is encouraged to read Seton et al. (2012).

Having a reconstruction extending back to the Jurassic is advantageous compared to previous models that only extended to the Cretaceous period (Lithgow-Bertelloni and Richards 1998). Previous studies (Bunge et al. 2002) found that whilst upper mantle features are replicated well; the shorter length plate reconstructions failed to generate structures seen in the deepest regions of the mantle (below 1500 km).

Figure 2.4 shows the root mean square (RMS) velocities for the entirety of the Seton plate model. Mantle circulation models can run at a differing convective vigour compared to the actual pace of Earth due to scalings of certain parameters. It is worthwhile to account for this when applying the plates as a boundary condition to ensure a smooth transition from the boundary layer to the volume below. This can be achieved by applying a scaling factor to the plate velocities. The scaling factor α is obtained using the plate model RMS velocity, V_p and the underlying RMS velocity of the TERRA model, V_m such that

$$\alpha = \frac{V_p}{V_m}.$$

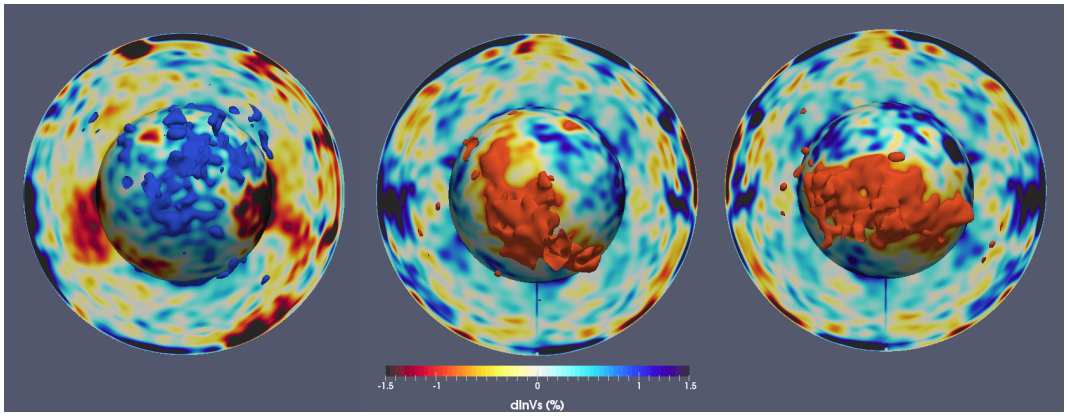

Fig. 2.5 Global view of shear wave seismic velocity perturbations (dV_s)in S40RTS focused on (left to right) Asia; Africa; Pacific. Images include a radial surface located at 2800 km with ± 1 % isosurfaces clipped above 2000 km depth.

If for instance the convective vigour of the underlying model was one order of magnitude slower than predicted for Earth, then $\alpha = 10$. Applying this would result in the plate boundary conditions being slowed by a factor of ten, with the model running for ten times the length; which in the case of the Seton et al. (2012) plate model would result in the model running for 2000 Myr.

2.5 Model validation

In order to learn from the outputs of numerical models, it is worthwhile employing some form of validation for the model. The availability of global seismic tomography for both S wave (Becker and Boschi 2002; Ritsema et al. 2004; Simmons et al. 2010; Ritsema et al. 2011) and P wave (Li et al. 2008) velocities allows the best insight into Earth's interior. These tomographic datasets reveal a wealth of detail on the mantle's present day internal structure. The main fast and slow anomalies as seen in the S40RTS model can be seen in fig. 2.5. The work of Schuberth et al. (2009b) and Schuberth et al. (2009a) present an excellent workflow for making the comparison of TERRA outputs to seismic tomography studies such as these.

From TERRA the modelled fields output are of pressure and temperature (P, T), and so can not be immediately compared to the tomographic models. These fields can be converted to elastic parameters by the way of mineral physics derived lookup tables (Stixrude and Lithgow-Bertelloni 2011). These

tables take account of the sensitivities of the seismic velocities to the range of parameters from temperature and pressure, to the phase changes present at various depths in the mantle. Furthermore, these conversions can be extended to account for a composition field (X), included from a thermo-chemical convection model, though this is beyond the scope of this work.

These seismic velocity fields are not entirely compatible with the tomography studies since the coverage of seismic observations is not uniform; depending on the uneven geographic coverage (few seismic stations based in the oceans, less robust coverage in poorer countries); the parameterisation for the tomography model; and the damping and smoothing effects of the tomographic inversion (Ritsema et al. 2007). The difference in resolution between modelled and observed seismic velocities has been made by a number of studies (Mégnin et al. 1997; Ritsema et al. 2007; Schuberth et al. 2009a; Bull et al. 2009). Because of this when we compare our models to tomography we will endeavour to account for this bias by applying the relevant resolution filter $\mathcal{R}$. The effect of these filters are two fold; firstly the data will be smoothed, and secondly any structure in the data above the maximum spherical harmonic degree of the resolution filter will be removed since this is the highest power wavelength in the respective model.

Currently such a filter is only available for the shear wave tomography model S20RTS (Ritsema et al. 2004), and its successor S40RTS (Ritsema et al. 2011) which has a higher spatial resolution due to being derived from a dataset that is an order of magnitude greater. These filters do not however, account for any systematic errors in the tomography model such as anomalous crustal corrections, or the effects of anisotropy (Ritsema et al. 2011). Therefore quantitive comparisons between TERRA and tomography can only be made with these models.

The typical workflow to compare to tomography would be as follows:

1. Run TERRA model to present day assimilating plate motion histories, outputting pressure and temperature fields (P, T).
2. Convert the output TERRA fields to seismic velocities V_s using the lookup tables of Stixrude and Lithgow-Bertelloni (2011).
3. Filter these velocities using the appropriate resolution filter $\mathcal{R}$.
4. Compare the filtered model output of TERRA $\mathcal{R}(V_s)$ to the observed tomography model $\mathcal{R}(V_s)$.

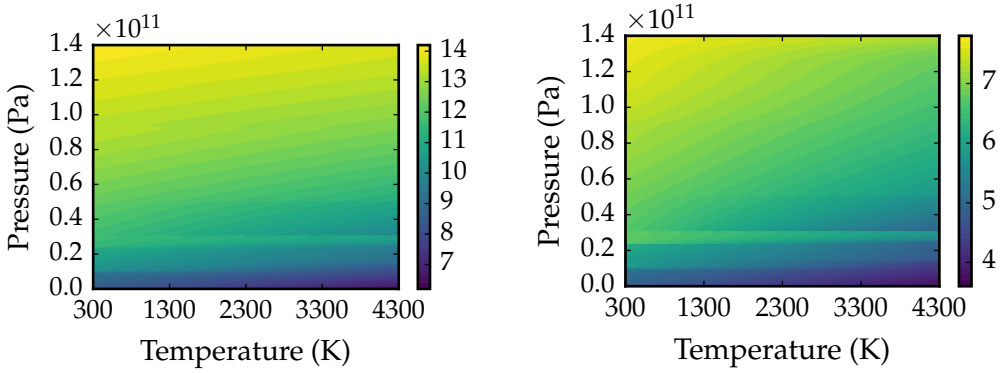

(a) V_p **(b)** V_s

Fig. 2.6 Contour plots of the respective velocity fields for the (P, T) lookup tables of Stixrude and Lithgow-Bertelloni (2011).

Of course this does not render the other seismic properties such as V_p redundant and when appropriate we would consider these.

2.5.1 Converting velocities to temperature structures

Whilst having the output from our TERRA model in the form of a velocity structure is useful, there may be occasions when we would like to take a velocity field and use it as a basis for a temperature structure in our models. To do this we would need to convert the velocities back into a temperature profile. We can see from the visualisation of the (P, T) lookup tables in fig. 2.6, that the mappings $(P, T) \mapsto V_p$ and $(P, T) \mapsto V_s$ are non-unique. This means that for a given velocity value, there are multiple points on the surface that could correspond to it.

As the mappings are non-unique we simply cannot reverse our conversion using an inversion of the same lookup tables. Instead we will briefly investigate a simple one-dimensional conversion with depth such as in Bull et al. (2010) for deriving the temperature field. This conversion utilises the equation

$$T = T_{ref} - \frac{1}{\alpha} R \left(\frac{\delta V_s}{V_s} \right) \tag{2.16}$$

where T_{ref} is the reference temperature for a given layer, α is the coefficient of thermal expansion, $R = \delta \log \rho / \delta \log V_s$ is a density-velocity scaling relationship derived from mineral physics studies, and $\delta V_s / V_s$ is the horizontal shear velocity perturbation.

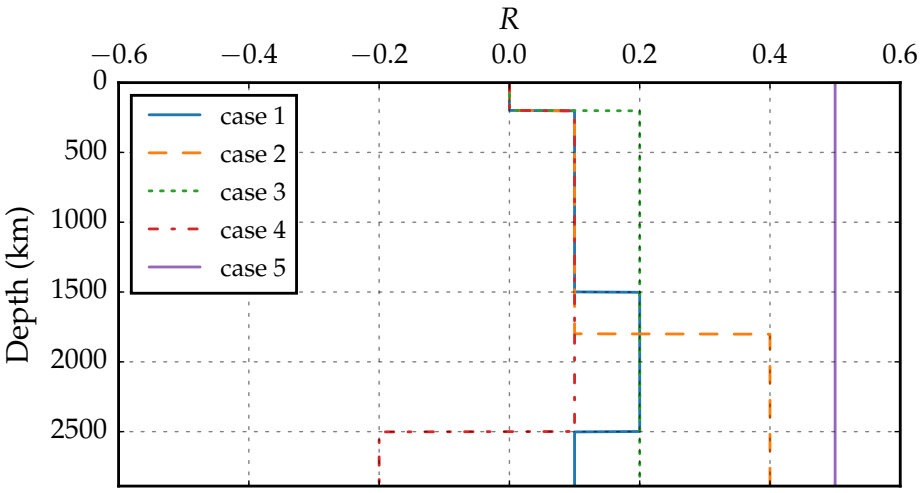

(a) R values gathered from previous studies in Bull et al. 2010 (case 1 Gurnis et al. 2000; case 2 Karato and Karki 2001; case 3 Steinberger and Calderwood 2006; case 4 Steinberger and Holme 2008). Case 5 is a single fixed value.

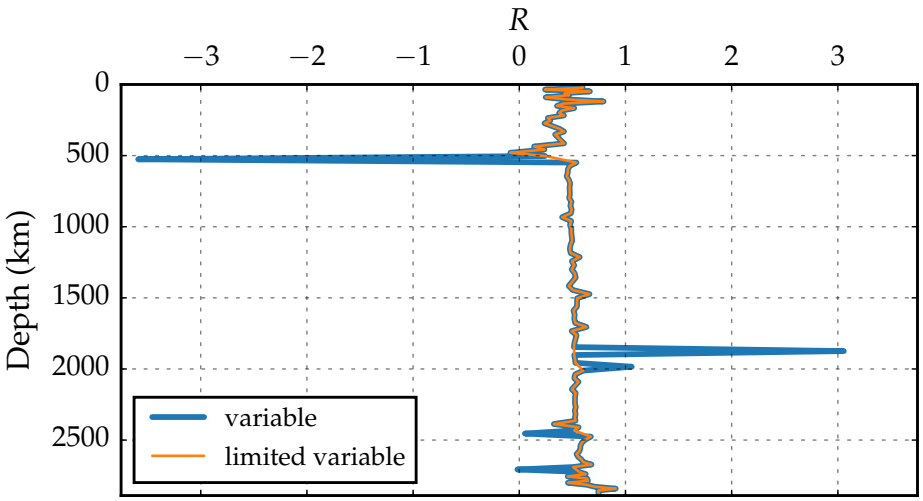

(b) R values calculated using radial average ρ and V_s values from the mantle circulation model used in the forward conversion. Limited variable is the same as variable but with extreme values replaced.

Fig. 2.7 Various choices for the depth dependent velocity-density scaling parameter R.

We see in eq. (2.16) that the controlling parameter for the conversion is R, which dictates the amplitude of the perturbation applied to the radial average temperature. Values for R recommended in previous studies lie in the range $-0.2 \leq R \leq 0.4$ with the depth profiles shown in fig. 2.7a (cases 1-4). For the top 200 km these four cases assume $R = 0$ under the assumption that compositional differences are likely to cancel out the observed high-velocity anomalies (Jordan 1978; Forte et al. 1995). We supplement the R values taken from the case studies with an R value calculated using $\delta \log \rho$ and $\delta \log V_s$ values from an MCM run. As can be seen in fig. 2.7b this derived value of R shows variation in the first 200 km where the previous case studies assume $R = 0$. Beyond this the calculated R shows minor variation with depth apart from a few outlying extreme values. We also test a second choice for this calculated R which has these extreme values replaced with the average value of the two adjacent layers. We define a value as extreme if $|R(r) - R(r-1)| > 0.4$ and $|R(r+1) - R(r)| > 0.4$, where r is the current radial layer. Finally we have case 5 which is a fixed value of 0.5, which loosely corresponds to the average value of the variable values.

To test the seven choices for the R parameter, we take the final output from an MCM and perform the conversion $T_{pre} \mapsto V_s \mapsto T_{post}$. Furthermore we perform the conversion using two different choices for the reference temperature T_{ref}. Our two choices are; one the radial average temperature for each layer from the end final output of our MCM calculation (fig. 2.8a); the other using the reference temperature calculated for the underling model based on its boundary temperature and assumed equation of state (fig. 2.8b). For these fourteen cases we compare the post conversion temperature,T_{post}, to the temperature prior to applying the conversion, T_{pre}, and calculate a volume averaged L^2 norm for the whole mantle, the upper mantle (0 km to 660 km) and the lower mantle (660 km to 2890 km).

We present the resulting norms for the differences in fig. 2.8. It can immediately be seen that using the radial average temperature profile results is a better fit to T_{pre} in all seven cases, and so we will only consider these. The effect of the extreme values present in the variable case are apparent with the upper mantle norm (and by extension whole mantle norm) over twice as large as the next nearest test case. By filtering out the extreme values of the variable case we see that the norm values are brought in line with other studies.

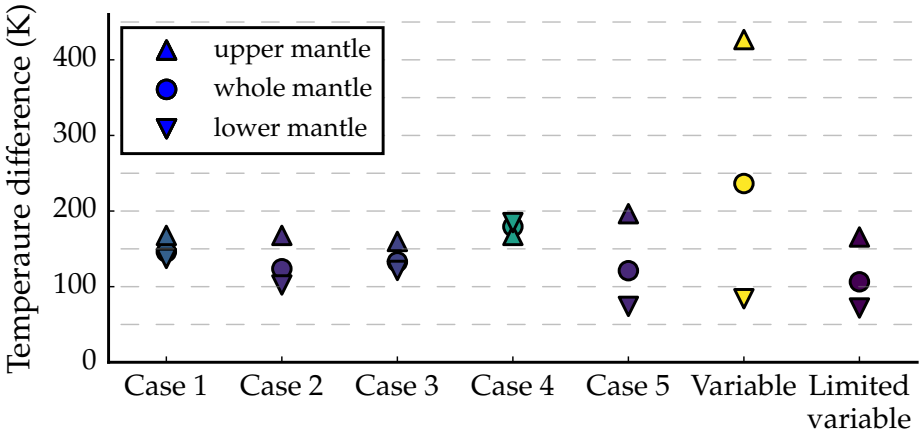

(a) T_{ref} = model average temperature

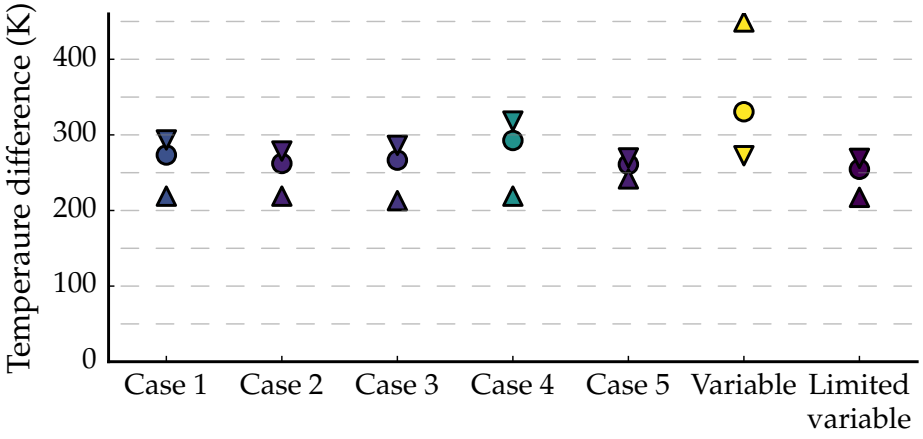

(b) T_{ref} = reference temperature

Fig. 2.8 L^2 norm of the difference between the temperature profile from a MCM before and after applying the conversion $T_{pre} \mapsto V_s \mapsto T_{post}$ (upper/lower mantle is calculated for layers above/below 660 km).

We see that the choice of whether $R = 0$ or not in the uppermost 200 km does not have a noticeable effect on the upper mantle norms, as cases 1-4 ($R = 0$) and the limited variable case ($R \neq 0$) have almost identical norm values. It is also possible that the slightly negative values of R around 500 km in the limited variable case are also erroneous as the best match is case 3 where $R = 0.2$.

In the lower mantle we see that all the case study values of R do not help us accurately perform the mapping $T_{pre} \mapsto V_s \mapsto T_{post}$ with all of them performing worse than our variable case. In particular the negative values in case 4 have a noticeably detrimental effect, being the only case where the lower mantle norm is worse than the upper mantle norm. We also see that the fixed value of 0.5 in case 5 yields an almost identical match to the limited variable case. From this we conclude that, at least in this example, that the values of R recommended from previous studies provide a weaker signal for the temperature structure than required. Furthermore we see that the extreme values in the variable case do not have as large an effect on the lower mantle norm, outperforming all the case studies also.

Overall we see that for this self consistent test case of the $T_{pre} \mapsto V_s \mapsto T_{post}$ mapping process, that using a limited variable R value determined internally provides the best results in virtually all regions.

2.6 Examples of TERRA models

2.6.1 Setup

To finish we present an example of a mantle circulation model. The model presented herein assumes incompressibility together with the Boussinesq approximation to obtain eq. (2.10). We define the model resolution such that we have an average grid spacing of 22 km.

The model parameters are detailed in table 2.2, with a viscosity profile that varies radially as follows:

$$\eta(r) = \begin{cases} 100\eta_0 & r \leq 100\,\text{km} \\ \eta_0 & 100\,\text{km} < r \leq 660\,\text{km} \\ 100\eta_0 & r > 660\,\text{km}. \end{cases}$$

Parameter		Value	Units
Surface temperature	T_S	300	K
CMB temperature	T_C	3000	K
Internal heating rate	H	6×10^{-12}	$\mathrm{W\,kg^{-1}}$
Reference viscosity	η_0	1×10^{21}	Pa s
Density	ρ	4500	$\mathrm{kg\,m^{-3}}$
Thermal expansivity	α	2.5×10^{-5}	$\mathrm{K^{-1}}$
Thermal conductivity	k	4	$\mathrm{W\,m^{-1}\,K^{-1}}$
Specific heat capacity	c_V	1134	$\mathrm{J\,kg^{-1}\,K^{-1}}$
Rayleigh number	Ra_H	$\approx 1 \times 10^8$	–

Table 2.2 Model parameters

At the surface we assimilate the 200 Myr plate reconstruction of Seton et al. (2012).

Before assimilating the plate reconstruction we first need to generate an initial condition for our first plate stage. Whilst TERRA can generate a number of spherical harmonic based initial conditions for the temperature field, these would not represent a realistic starting point for the model; as we could begin subducting material as described in the reconstruction, into a region that our initial condition has set as positively buoyant.

To remedy this we take a two step initialisation phase. First we run a mantle convection model with the surface boundary set as free-slip from a spherical harmonic initial condition. We run this until the mantle is well mixed and nominally reached a thermal steady state. At this point the oldest plate stage is then assigned as the surface boundary condition, and run for a length of time corresponding to 50 Myr after accounting for any RMS velocity scaling. This allows the features of the oldest stage to be conditioned into the mantle, with spreading ridges and subducting regions having the appropriate temperature material underneath them. Whilst this is by no means a perfect method of generating an initial condition, it does allow models to evolve more smoothly as sharp changes between differing temperature structures are not imposed. With this constructed initial condition, the plates are then applied and run from the oldest plate stage to present day.

At the models conclusion the temperature structure is output, together with seismic structure based on the lookup tables of Stixrude and Lithgow-Bertelloni (2011) which assume a pyrolitic compositional mantle.

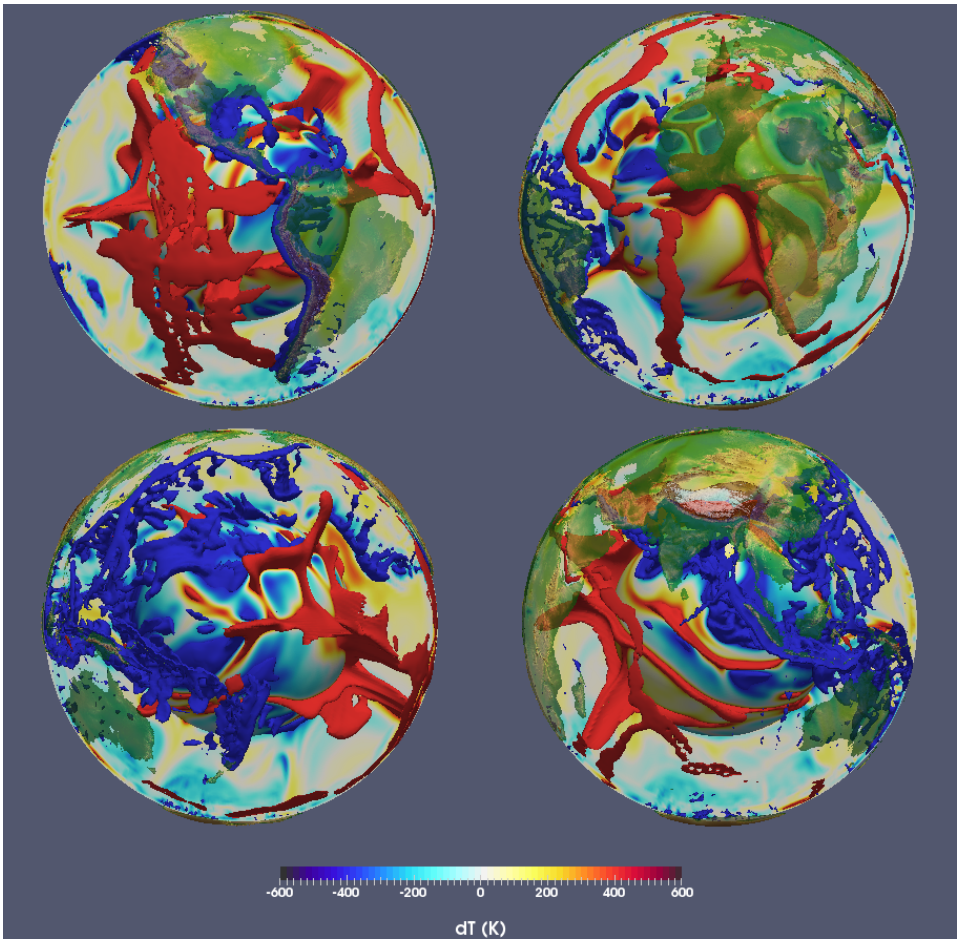

Fig. 2.9 Global view of lateral temperature variations centred on (clockwise from top left) $-90°$; $0°$; $90°$; $180°$. Images include a radial surface located at 2800 km with ± 400 K isosurfaces and present day surface topography.

2.6.2 Results

In fig. 2.9 we present the present day temperature structure with the radial average temperature subtracted from the field. This allows us to highlight the hotter and colder than average features of the volume.

The spreading ridges located in the Pacific and Atlantic are depicted by the 400 K isosurface located at the surface. The Pacific spreading ridge appears much wider compared to the atlantic, which can be attributed to the much faster spreading rate here. Looking deeper towards the CMB, we can see a number of plume like features depicted by the hot isosurface located in two main groups. Some of these plumes can be seen to extend almost the entire radial distance of the volume, predominantly in the regions beneath

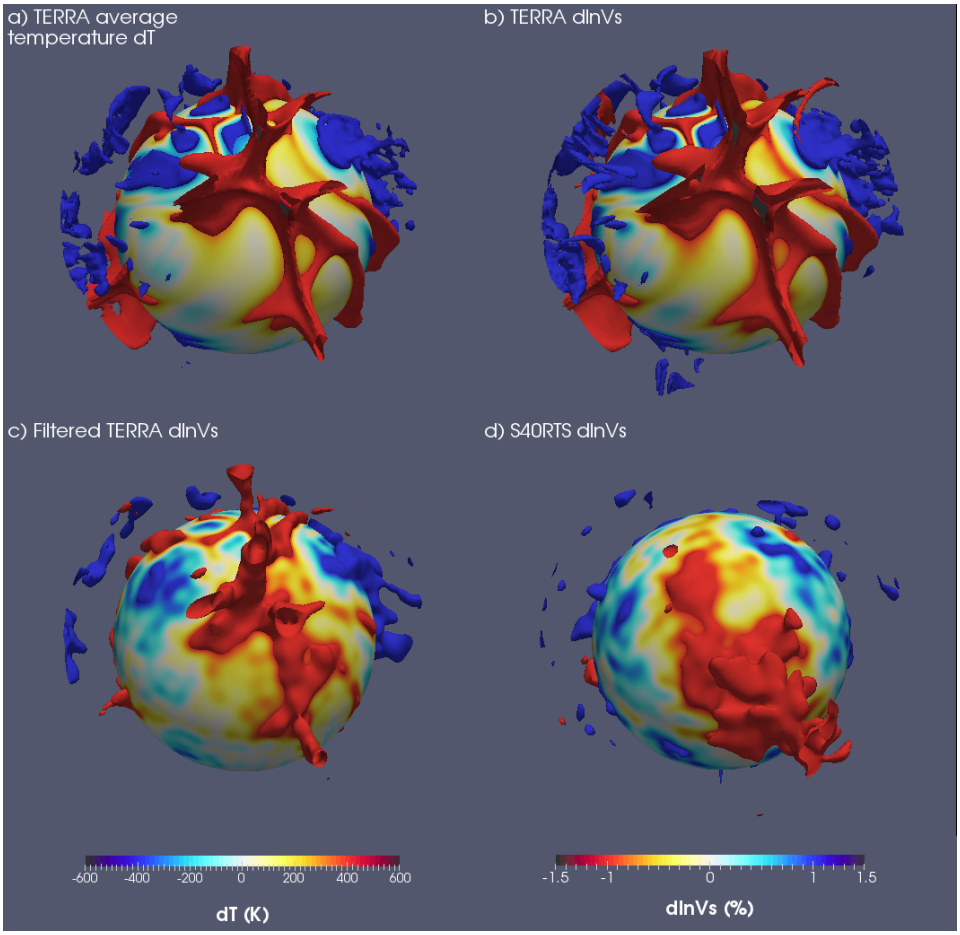

Fig. 2.10 View of (a) TERRA average temperatures, (b) converted shear wave velocity perturbations, (c) converted shear wave velocity perturbations after applying the corresponding resolution filter, (d) S40RTS velocity perturbations focused on the Atlantic seismic anomaly. Images include a radial surface located at 2800 km with ± 400 K isosurface for temperature and ± 1 % isosurface for seismic velocities.

spreading ridges. These two clusters are located in the general regions where we observe seismically slow regions in tomography models.

Looking at the -400 K isosurface we see many structures consisting of lines of cold material that are sinking. These features line up with the subducting regions on the Earth's surface, for example the continuous region lining up with the western edge of the Americas. Looking towards central and eastern Asia we can see a much larger volume of colder than average material; hinting towards the greater amount of subduction that has occurred in the region, with major events such as the closing of the Tethys and migration of the Indian subcontinent into Asia.

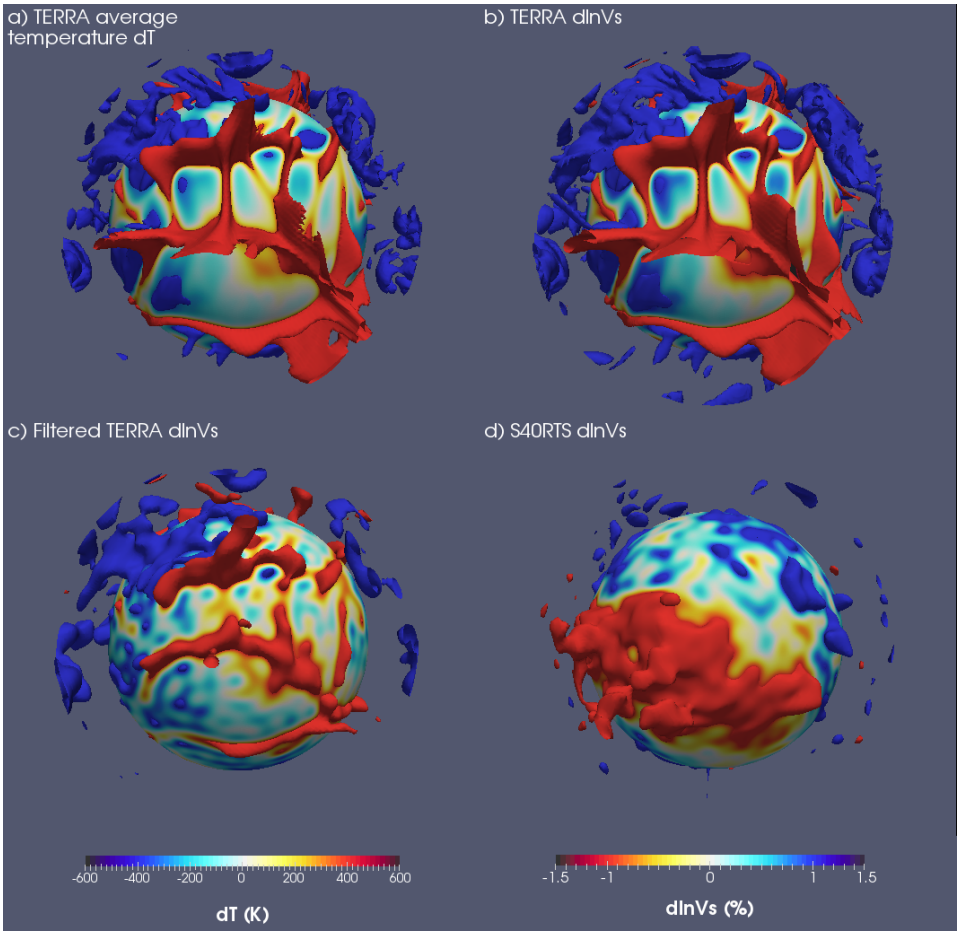

Fig. 2.11 View of (a) TERRA average temperatures, (b) converted shear wave velocity perturbations, (c) converted shear wave velocity perturbations after applying the corresponding resolution filter, (d) S40RTS velocity perturbations focused on the Pacific seismic anomaly. Images include a radial surface located at 2800 km with $\pm$400 K isosurface for temperature and $\pm$1 % isosurface for seismic velocities.

Moving on to compare our models to the tomography model of S40RTS we present views of; lateral temperature variations; lateral seismic velocity variations; lateral seismic velocity variations after applying the resolution filter of S40RTS; the S40RTS model in figs. 2.10 and 2.11.

The first point to note is the striking similarity between the temperature and unfiltered seismics. We can also see how the resolution of features captured in the numeric model compare to the tomography, with boundaries and features much sharper for the same velocity. With the filter applied we can directly compare our modelled output to the tomography. Despite some discrepencies, the -1% isosurface located under Africa is remarkably similar with the same NW-SE direction, and covers a similar region of slower

than average perturbations. In the Pacific however, we do not see the same dense collection of the -1% isosurface but rather a web of slower features that extends further west and north.

Over the entire volume the 1% isosurface which corresponds to the subducting material is more substantial in the TERRA output compared to S40RTS, but overall appears in the same regions in both.

Whilst this is by no means an exhaustive analysis between the modelled output and observed, this does allow the reader to view the merits of such an approach to modelling mantle convection.

2.7 Conclusion

In this chapter we have outlined the mathematical formulation and computational code TERRA which solves the equations for mantle convection. Following that we briefly discussed the assimilation of plate reconstructions to condition our models to the Earth and how these results can be compared to present day datasets of the Earth. Lastly we showed a typical TERRA simulation setup and the results obtained, together with how they compare to the tomographic dataset S40RTS.

Now the reader has an understanding of the base methodology behind mantle convection modelling we will begin to investigate the overarching problem being addressed in this thesis, the importance of accurate knowledge of the initial condition.

CHAPTER 3

INVESTIGATING THE LYAPUNOV TIME FOR MANTLE CIRCULATION MODELS

Abstract

Mantle convection models are an effective method for helping to test and develop theories for geological observations. However, as with any model an initial condition is required to begin a calculation and this is inherently unknown for the instance of Earth modelling. It has been suggested that as convection in the mantle is chaotic, small differences in the initial condition have a significant influence on the final mantle structure, with a 'limit of predictability' timeframe being in place. In this work we conclude that by having knowledge of the surface boundary condition (such as plate reconstructions) the limit of predictability for mantle convection models can be extended to much greater timeframes than previously thought.

3.1 Introduction

Earth's mantle has a dominant role in Earth dynamics due to its influence on surface processes such as plate tectonics. The mantle makes up $\approx 84\%$ of Earth's volume , as well as $\approx 68\%$ of its mass yet direct observations are difficult due to the presence of the crust and so understanding it is crucial for a variety of disciplines in Earth science. Earth's mantle although solid, convects by a means of viscous creep at a rate of $1\,\mathrm{cm\,yr^{-1}}$ to $10\,\mathrm{cm\,yr^{-1}}$, with a Rayleigh number (the measure of convective vigour of a system) of 10^6 to 10^8 (Schubert et al. 2001). Since over geological timescales we can consider the mantle to a be a readily convecting volume, it can be modelled as a fluid

dynamical system (Mckenzie et al. 1974). Key to solving this mathematical problem then is knowledge of the systems boundary and initial conditions. As Earth's mantle structure is not known in the past this is something that Geodynamiscists can only make assumptions at when conducting their models, although efforts are being made to constrain this uncertainty using complex techniques that hope to bridge this gap in knowledge (Bunge et al. 2003; Atkins et al. 2016). However, we note that due to the high Rayleigh number predicted for the mantle, we have a system that is chaotic in nature (Stewart and Turcotte 1989).

The idea of chaos in a dynamical system is simple; a small change in the systems conditions leads to unpredictable changes in the system such that they appear random in nature. For mantle models, this in essence corresponds to the idea that two mantle models started from a similar initial condition can and will diverge over time such that they are two uncorrelated mantles. This clearly creates an elephant in the room situation for research in modelling the mantle's evolution if even a slight variation in the starting condition can completely change the final result.

This presence of chaos in dynamical systems has been studied across a variety of numerical fields, with the earliest research being undertaken by Lorenz (1965), where the author looked at initial condition error growth for atmospheric models. This study of initial condition error growth was extended to mantle convection models in Bello et al. (2014). For an error on an initial condition of $\leq 5\%$, they showed that results from mantle models can only be reliably extended over a period of 95 Myr, beyond this time chaotic growth of differences in the system overwhelm the results. This time period would limit mantle convection models to within the breakup of Pangea to present day. However, plate reconstructions have been produced based on a variety of Earth observations that extend far beyond this window from the Cenozoic, with more recent studies even reaching into the Paleozoic (Lithgow-Bertelloni and Richards 1998; Seton et al. 2012; Müller et al. 2016). Such plate reconstructions have been used in mantle convection models as a surface boundary condition in many studies (Zhong et al. 2000; Bunge et al. 2002; Davies et al. 2012) to great effect. These studies and more have used these reconstructions in models that run far beyond the recommended 95 Myr limit, to generate mantle structures that correlate with other present day observations from studies in seismic tomography for instance (Schuberth et al. 2009b). This suggests that it is possible to extend this limit on predictability

for mantle models when we consider the assimilation of a known surface boundary condition.

Several previous studies have discussed the implications of the upper boundary of mantle convection models on the overall dynamical structure of the system. Both Tan et al. (2002) and Davies (2005) note how the presence of material subducted from the surface can organise the deep mantle plumes away from these locations, fixing plumes locations into a steady state pattern.

In this chapter we will endeavour to determine what effect, if any, assimilating a known surface boundary condition has on the limit of predictability, building on the method as lain out by Bello et al. (2014). Work into determining what effect this may have has already been touched upon by Colli et al. (2015). Further to this, we shall also break the problem of error growth down and investigate what effect the different heating modes present in Earth's mantle have on error growth.

3.2 Method

3.2.1 Numerical methodology

Our method closely follows that of Bello et al. (2014) and Colli et al. (2015) by applying the twin experiment method (Lorenz 1965) to mantle circulation models.

The twin experiment method utilises a reference model T and a second model that is perturbed by some degree from the reference, T_p. These two models are integrated forwards in time, and the differences between the two models as time progresses is used to calculate the Lyapunov exponent λ, a measure of the convergence or divergence of the dynamical system being analysed (Benettin et al. 1980). Knowing the value of λ we can then determine the Lyapunov time $\tau = 1/\lambda$, from which we infer the length of time before two initially similar temperature fields will have diverged to a point such that their solutions are uncorrelated.

For our investigations, T is taken from a quasi-steady thermal state mantle convection calculation, whilst the perturbed twin T_p has uniformly distributed random perturbations applied to this temperature field. The magnitude of the applied perturbations is up to $\pm 1\%$ of the average temperature for the given layer in the volume. We monitor the error, $E(t)$, between the

two models through time by

$$E(t) = \int_{V_\Omega} \frac{|T_p(\boldsymbol{x},t) - T(\boldsymbol{x},t)|}{T(\boldsymbol{x},t)} \frac{\mathrm{d}\boldsymbol{x}}{V_\Omega}. \tag{3.1}$$

The error $E(t)$ is related to the Lyapunov exponent λ by

$$E(t) \approx E(0)\exp(\lambda t), \tag{3.2}$$

where $E(0)$ is the initial temperature difference. From this we see that the errors are expected to change exponentially, though the direction of change in mantle convection models has been shown to depend on the surface boundary conditions (Colli et al. 2015). Colli et al. (2015) show that by assimilating surface velocities in both the reference and perturbed models the diverging of the two cases is limited, and in fact can converge to within small errors of one another which we shall investigate further here also.

Mantle circulation models are carried out using an adapted version of the three-dimensional finite element code TERRA (Baumgardner 1985; Bunge et al. 1996), on a mesh with 10 million finite elements, which corresponds to an average grid spacing of 50 km. TERRA solves the equations governing conservation of mass, momentum and energy (eq. (3.3)) for an incompressible fluid;

$$\nabla \cdot \boldsymbol{u} = 0 \tag{3.3a}$$

$$\nabla \cdot \left\{ \eta(\nabla \boldsymbol{u} + (\nabla \boldsymbol{u})^T) \right\} - \nabla P + \alpha\rho(T_{av} - T)\boldsymbol{g} = 0 \tag{3.3b}$$

$$\frac{\partial T}{\partial t} + \boldsymbol{u} \cdot \nabla T = \kappa \nabla^2 T + H, \tag{3.3c}$$

where η is the dynamic viscosity, α is the coefficient of thermal expansion, ρ the reference density, T_{av} the radial temperature profile, $\boldsymbol{g}$ gravitational acceleration, κ is the thermal diffusivity and H is radiogenic heat production.

3.2.2 Model configuration

Our model setup closely mirrors that of previous studies, with our models being incompressible, using the Boussinesq approximation such that density differences are neglected except in the buoyancy term. For our investigations we look at two viscosity profiles, one isoviscous, the other with a layered viscosity profile. For the radially varying profile, we prescribe a three layered

Parameter		Value	Units
Surface temperature	T_S	300	K
CMB temperature	T_C	3000	K
Internal heating rate	H	4×10^{-12}	$\mathrm{W\,kg^{-1}}$
Reference viscosity	η_0	3×10^{22}	Pa s
Density	ρ	4500	$\mathrm{kg\,m^{-3}}$
Thermal expansivity	α	2.5×10^{-5}	$\mathrm{K^{-1}}$
Thermal conductivity	k	4	$\mathrm{W\,m^{-1}\,K^{-1}}$
Thermal diffusivity	κ	1×10^{-6}	$\mathrm{m^2\,s^{-1}}$
Specific heat capacity	C_V	1000	$\mathrm{J\,kg^{-1}\,K^{-1}}$

Table 3.1 Model parameters used in this study.

mantle with $\times 100\eta_0$ in the uppermost 100 km to mimic the effects of a lithosphere; an upper mantle with the viscosity equal to the reference viscosity η_0; a stiffer lower mantle where the viscosity increases up to $\times 30\eta_0$ between 800 km to 1000 km. Having the viscosity transition for the lower mantle at this depth falls in line with the recent observations of Rudolph et al. (2015). Other key model parameters are outlined in table 3.1.

A free slip boundary condition is defined at the CMB, while the surface boundary condition for the perturbed twin are either prescribed by assimilating the reference models surface velocities or allowed to be free slip.

We will further break down the investigation by looking at the effects different heating modes have on the error growth. To achieve this we will look at purely basally heated, purely internally heated and mixed heating models.

To aid in the comparisons we define the Rayleigh number, a non-dimensional value which quantifies the convective vigour of the system, which for a basally heated volume is defined as

$$Ra_b = \frac{\alpha \rho \Delta T D^3 g}{\kappa \eta},$$

where D is our mantle radius and ΔT the total temperature contrast. We also define a second Rayleigh number which is appropriate for an internally heated volume that is defined as

$$Ra_H = \frac{\alpha \rho^2 H D^5 g}{k \kappa \eta}.$$

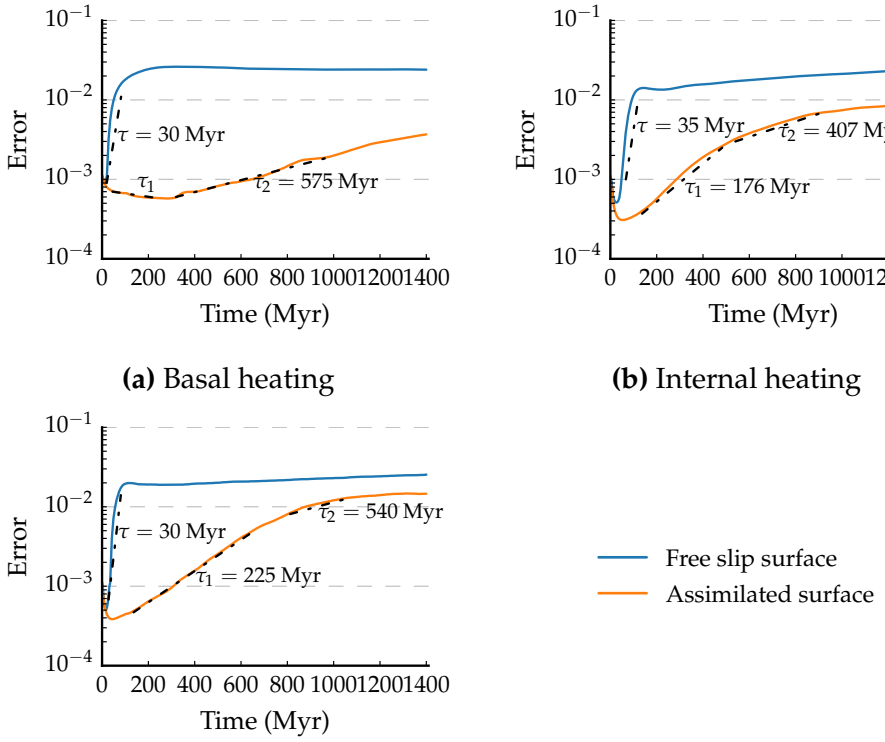

(a) Basal heating

(b) Internal heating

(c) Mixed heating

Fig. 3.1 The error growth experienced by isoviscous models heated by various heating modes. The inverse of the gradient of each curve gives the respective Lyapunov time τ for each case.

Using the values used in this study gives our models Rayleigh numbers $Ra_b \approx 5 \times 10^6$ and $Ra_H \approx 9 \times 10^7$, meaning we expect the vigour of convection in our models to be below what is expected for Earth. Because of this we scale the timescales of our models to allow a similar amount of convection to occur in the models presented here.

3.3 Results

3.3.1 Isoviscous models

The first set of results are for the isoviscous models using the three different choices in heating mode. In fig. 3.1 we see that the free slip models all show a very similar evolution. The models first experience a short period of decreasing errors, where the smallest perturbations are removed by diffusion effects as observed by Bello et al. (2014). This is followed by a large growth

in the errors before saturating around 2×10^{-2}. These free slip models all yield a Lyapunov time around 30 Myr.

In comparison, the evolutions of the various heating modes when coupled with an assimilated surface boundary condition show a contrasting picture. Each model experiences the same familiar pattern of error evolution, though over a much longer time frame compared to the free slip cases. Each model shows a much longer and greater period of decreasing errors before the errors rise to saturation. In fig. 3.1a we see that while the assimilated case has not reached a saturation level, the Lyapunov time of its error growth far exceeds that of the free slip case with $\tau = 575$ Myr. Both the internally heated (fig. 3.1b) and the mixed heating (fig. 3.1c) models do reach saturation, though at levels still below the free slip counterparts and with much larger Lyapunov times to match.

3.3.2 Layered viscosity

Here the error growth is noticeably different from the isoviscous cases when assimilating surface velocities, as shown in fig. 3.2. Whilst the free slip model errors saturate around 2×10^{-2} as in the isoviscous case, we observe that there are two distinct Lyaypunov times for each heating mode. These arise from the layers of the mantle present here, and the respective time scales of convection in the layers. Studies into the Lyapunov times of atmospheric models determine these the short and long scale Lyapunov times to be associated with short and long scale flow respectively (Boffetta et al. 1998). When considering this feature in our mantle models we view the shorter Lyapunov times as being associated with the lower viscosity upper mantle, where the growth of errors are less impeded by viscous flow. The other Lyapunov times meanwhile correspond to the more viscous lower mantle which slows error growth, yielding a correspondingly longer value for τ.

With a layered mantle, we see that incorporating a known surface boundary condition has a noticeable effect on the resulting Lyapunov times. Each case has an early period of error reduction beyond the expected window attributed to diffusion of the smallest perturbations. Because of this we conclude that the long scale Lyapunov times, associated with the long scale flow, are in fact negative when assimilating the surface boundary condition. Furthermore the second Lyapunov times, relating to short scale flow, all far

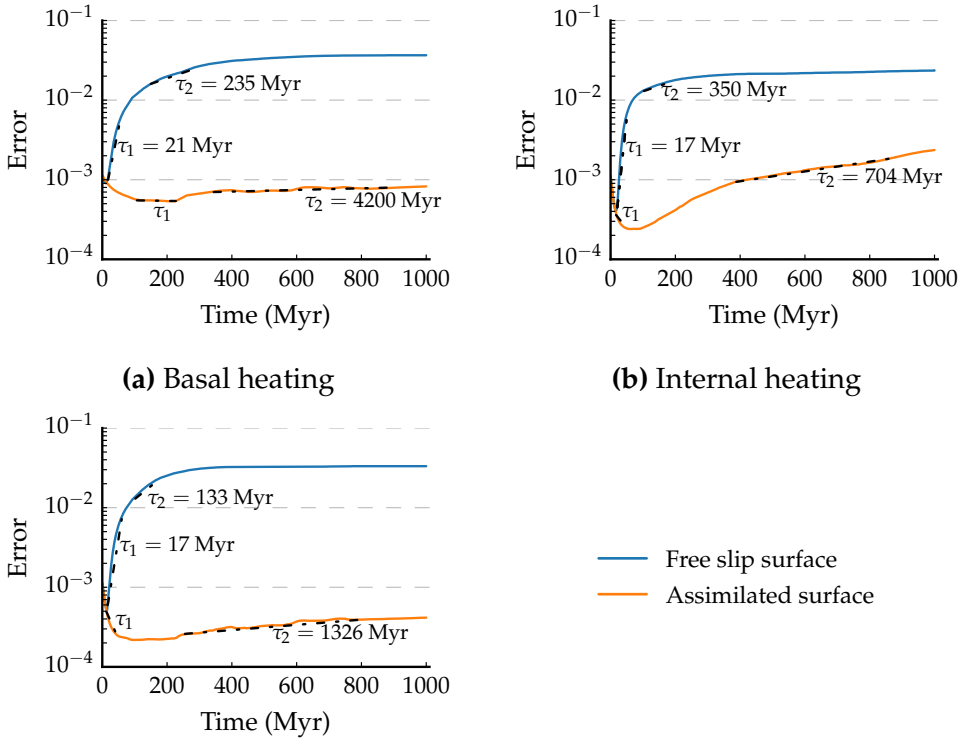

(a) Basal heating

(b) Internal heating

(c) Mixed heating

Fig. 3.2 As fig. 3.1 but for models with a layered viscosity profile.

exceed that of the length of mantle overturn; further supporting the case that assimilating surface boundaries is an adequate constraint on error growth.

In fig. 3.3 the pointwise temperature difference between the perturbed and reference models ($T_p - T$) is presented for the final time of the mixed heating models. Both models have a negative average value, for free slip this is -38 K and -0.1 K for the assimilated case. Similarly the median value for both cases is negative. The skew of the pointwise difference towards negative values implies that more regions of the perturbed model are colder than the reference model. As the initial perturbations applied were a normal distribution of hotter and colder temperatures over the whole volume we conclude that this skew is indeed due to the divergence of the two twin cases. The spread of the data is also noticeably different for the two surface boundary conditions, with the standard deviation for the two cases being 308 for free slip, and 20 for assimilated. This difference in standard deviations highlights the ability to constrain error growth using an assimilated surface.

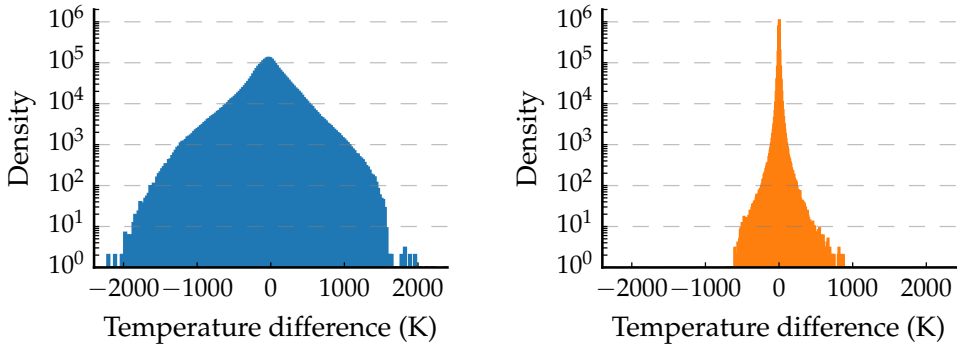

(a) Free slip surface

(b) Assimilated surface

Fig. 3.3 Histograms of the temperature difference $T_p - T$ at each grid point at the end of the mixed heating, layered viscosity cases.

3.3.3 Isolating the source of error growth for assimilated surface boundary conditions

Following on from our range of cases investigating the effect of heating mode and viscosity structure on the error growths of model, these final tests aim to shed light on the long term error growth of models from two of the main parts of the model; namely the effect of buoyancy and assimilating the surface boundary. To achieve this we ran two further cases for both the isoviscous and layered viscosity mixed heating models; one where we replaced the assimilated surface by a rigid surface (hereafter referred to as *R*+*B*) which could be run much longer than our assimilated period, and the other that has the assimilated surface boundary condition but without buoyancy forces (*A*-*B*).

The results for these models are shown in fig. 3.4. The most obvious observation is that the models with an assimilated surface and buoyancy forces (*A*+*B*) behave differently depending on the viscosity structure. We attribute this to the lack of viscous layers in the isoviscous model allowing errors to convect through the volume more readily, while when layered the viscosity impedes the growth of errors due to the two length scales of errors as discussed previously. The Lyapunov times for *R*+*B* models is slightly shorter in both instances compared to *A*+*B* with $\tau = 200$ Myr for isovicsous *R*+*B* and $\tau = 2500$ Myr for the layered viscosity *A*+*B* case.

Meanwhile the *A*-*B* models rather unsurprisingly see very large (isoviscous) or negative (layered viscosity) Lyapunov times. The driving forces of the assimilated surface on these models are clearly shown here to be the

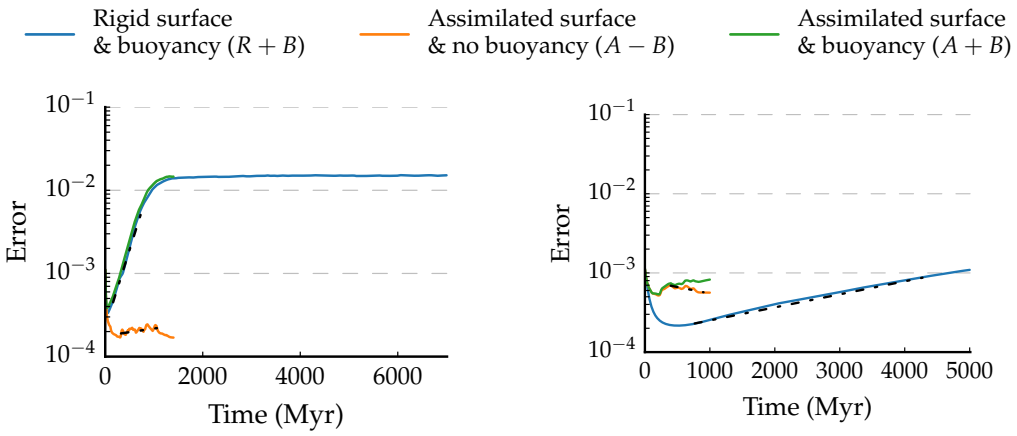

(a) Isoviscous

(b) Layered viscosity

Fig. 3.4 The error growth experienced by isoviscous and layered viscosity models with a mixed heating mode and various physical parameterisation setup.

source impeding error growth. Of final note, the small oscillation of the isoviscous *A*-*B* case is of little relevance as the error values are at a scale that corresponds to only single digit differences in temperature across the whole volume.

3.4 Discussion

The method of twin experiments clearly shows how different physical setups and parameterisations can alter the error growth of convection models.

Our results show general agreement with those of Colli et al. (2015). Assimilating a surface boundary significantly alters the error growth of a mantle convection model compared to when the surface boundary condition is taken as free slip as in Bello et al. (2014). We see that regardless of model setup that a free slip boundary condition sees error growth over short time spans. This agrees with the assessment of Bello et al. (2014) in that a purely free slip model, with no knowledge of the models time evolution (from sources such as plate reconstructions) will significantly limit the time frame in which meaningful conclusions can be drawn.

Looking at the error growth in our assimilated surface models we do, in comparison to the free slip cases, observe significant variation in Lyapunov times. We see that the influence of internal or basal heating on the error growths in models is dependent on the rheological structure of the volume.

For the isoviscous cases, basal heating yields the longest Lyapunov time ($\tau = 575\,\text{Myr}$). The longer Lyapunov time for the basally heated case can be explained by the presence of large thermal upwellings in the initial state, which even after experiencing a perturbation are still the dominant driving force in the mantle volume. For the internally heated case, large thermal plumes are not the dominant feature due to the lack of a lower thermal boundary layer (Hüttig and Breuer 2011). Coupled with the models higher Rayleigh number this results in a more complex time-dependent pattern compared to the basally heated model, with the convection cells being typically half the size of basally heated models (Wolstencroft et al. 2009; Deschamps et al. 2010). The mixed heating model sits between the Lyapunov times of the two end member heating modes.

Meanwhile when the model contains a layered viscosity profile, more typical of what would be expected in Earth, we see the negative Lyapunov times for a significant period of the calculations (between 10 and 20% of the model timespan). The differences between heating modes are less pronounced with only the internal heating mode showing any real error growth. As previously discussed we attribute this to the different length scales present in the layered viscosity models. Small scale errors applied to the perturbed model grow rapidly in the upper mantle of the internally heated case, with their effects limited by the higher viscosity in the rest of the volume. As the basally heated model is heated purely from the base of the volume, small scale perturbations do not grow in the lower viscosity region as readily as when internal heating is present.

Considering this we conclude that the internal heating has a much more pronounced effect on error growth, due in no small part to the fact that it is present across the whole mantle volume and so any any small deviation in the temperature field will be greatly influenced by this. In comparison the effect of a small deviation in the temperature field when in the presence of the large convecting plume features associated with basal heating will very quickly be smeared out.

There is a however a noticeable difference from the results observed here and those of Colli et al. (2015), with the development of error growth and reduction taking noticeably different paths. In their study they perform similar error analysis on internally and mixed heating models, and record consistent negative Lyapunov times across both isoviscous and three layered viscosity models. The internal heating rate Rayleigh number for the models

in their study, $Ra_H = 2.4 \times 10^7$, is over a factor of three lower than in this study. This difference in Rayleigh number can account for some of this difference as Bello et al. (2014) have shown that increasing the Rayleigh number reduces the resulting Lyapunov time of the model. A further reason for the difference could be the difference in initial error perturbation applied to the perturbed twin. In this study the initial perturbation results in a discrepancy of $\approx 1 \times 10^{-3}$, while in Colli et al. (2015) the initial perturbations create a discrepancy $\approx 8 \times 10^{-3}$. Subsequent error reductions they observe end at values still above those observed for the layered cases in this study. Considering this, we do not believe our results represent a significantly different conclusion from Colli et al. (2015) in that assimilating the surface boundary greatly reduces the effect of the chaotic drift from the reference model.

The knowledge that assimilation techniques can overcome the effects of initial errors has been known for some time with various studies that have used long timescale plate reconstructions in their studies observing excellent matches to other present day observations. This is corroborated by the results of the calculations that do not include the effects of buoyancy forces as the assimilation of the surface boundary in this situation results in negative Lyapunov times. Considering this we note that a number of studies (e.g. Schuberth et al. (2009a) and Davies et al. (2012)) have found that with the appropriate parameter setup, after an assimilation period over 100 Myr or more the present day structure can yield an excellent match to deep Earth seismic structures.

Knowing that mantle circulation models converge to a solution without seeing error growth due to the assimilated surface boundary is of limited use in studies looking at past mantle flow however. As an example, studies that look at the long term stability of the large low shear velocity provinces (Zhang et al. 2010; Bower et al. 2013; Bull et al. 2014) would see limited benefits from the conclusions of this study. This is because even with the reduction in errors over the entire calculation, the choice of the initial condition will have an influence at the models initiation that cannot be overcome by these assimilation methods.

This initial condition issue is being overcome by various techniques, including variational data assimilation techniques (Bunge et al. 2003; Liu and Gurnis 2008). This method relies on iterating a convection model forward and backwards in time and so the results of this study on error growth suggest

that this technique can be used without fear of errors being introduced. This corroborates the results of Vynnytska and Bunge (2014), where they applied a free slip and an assimilated surface to variational data assimilation models. They found that their results show convergence for assimilated surface conditions and diverged for the free slip case. Our results together with those of others all clearly point to data assimilation of the surface boundary significantly reducing the divergence of solutions compared to free slip models.

3.5 Conclusion

In this study we have built on previous work investigating the Lyapunov times for mantle convection models. We have shown that irrespective of viscosity profile or heating mode, assimilating known surface velocities greatly increases the Lyapunov time of a calculation far beyond the timescales of plate reconstructions. The implications of this is that results from mantle models that incorporate a known surface velocity can be trusted over much longer timescales. With this knowledge it is possible to place greater confidence in techniques that project present day mantle structure back in time by variational assimilation techniques. Given the lack of certainty of the initial condition for mantle convection models it is a natural step to go on to investigating the framework of such methods to determine their robustness towards the initial condition problem.

In our work we have not considered the effects of compressibility nor temperature dependent rheologies. Both of these would be expected to further alter the Lyapunov time as the errors introduced in the twin experiment method would influence the evolution of these two physical properties. Further studies should be conducted investigating these properties as both are expected for Earth's mantle.

Taking the knowledge that the assimilation of a known surface boundary reduces the sensitivity of models to the initial condition we turn our attention to improving the initial condition. In the next chapter we will look in detail at the methods of performing such a feat.

CHAPTER 4

METHOD - ADJOINT MODELS & TERRA

4.1 Introduction

During the derivation for the equations of mantle convection in Chapter 2, we showed that the models require an initial condition. We recall that to obtain this initial condition, we rather arbitrarily precondition the thermal structure by running the oldest plate stage for an extended length of time (typically $\mathcal{O} \sim 100\,\text{Myr}$). We also saw that the application of a plate motion history model, to create what we call a mantle circulation model (MCM) (Bunge et al. 1998), allows our models to match the general large scale features observed in Earth.

Whilst MCMs generate outputs that can draw good comparisons to present day observations (Bunge et al. 2002), we have seen in Chapter 3 the effect that small scale perturbations can have over the time scale of a typical mantle circulation model. The work of Bello et al. (2014) presented the idea that the choice in initial condition can alter the final outcome. While the work presented here as well as in Colli et al. (2015) show that by assimilating a plate reconstruction the growth of errors is limited and can, instead of diverging, show a converging solution.

Despite these results, there is still an accuracy issue present at the calculations initiation and early evolution. With this in mind, we cannot disregard the importance of our initial condition when hoping to investigate the long term evolution of the mantle. Because of this we now look to implement optimisation techniques that allow known data to be incorporated into models to improve forecasting by minimising the errors.

As we have discussed, information of Earth in the past is extremely limited, whereas at present day we have copious amounts of information

ranging from; the geoid, seismic tomography, topography, heat flow values and more. However, this is of no use in our mantle models as none of this information is carried back into the past. The only data assimilation that does influence a model is the plate motion histories that we can apply as a boundary condition. Although these also suffer from the same drawback as they are explicitly assimilated forwards in time, and so again, information only influences the future structure.

With all of this in mind it is clear that a method that uses this information and propagates its information backwards in time could provide a new avenue of exploring past mantle evolution. We will now turn to look at the methods available to achieve this goal, before developing our chosen method and applying it to improve our initial conditions in a rigorous manner; leaving behind the ad-hoc constructions that have been the norm previously.

4.2 Inverse theory for mantle convection

Early attempts at using present day information to infer prior Earth properties were performed by Steinberger and O'Connell (1997) to investigate true polar wander. They performed their investigation by taking present day shear wave velocity heterogeneities, converting these to density anomalies and using this as an initial condition. Their model was then run backwards in time by reversing the time stepping such that the energy equation runs backwards. Such a method is known as 'backwards advection' (BAD). The issue with the BAD method is that the thermal diffusion, $\nabla^2 T$, becomes unstable when run in reverse. To take account of this the authors ignored the diffusive term in their calculations, while limiting their calculations to 64 Myr. Furthermore, in Steinberger and O'Connell (1998) the authors look at the errors associated with running BAD models. They conclude that outside of the thermal boundary layers, the effects of thermal diffusion are not pronounced since advection, not diffusion, is the main method of heat transportation. In both Steinberger and O'Connell (1997) and Conrad and Gurnis (2003) calculations are limited by the effects of diffusion, limiting reliable calculations to ~ 75 Myr when looking across the whole mantle.

In order to overcome the effects of the diffusive term in a time reversed calculation, geodynamicists have looked to other fluid mechanical branches to borrow techniques they use for inverse problems. In meteorology, Ta-

lagrand and Courtier (1987) and Courtier and Talagrand (1987) apply a variational method (VAR) to incorporate present observations into their models to predict the initial state consistent with those present day observations. This method of variational assimilation of observations is also known as an adjoint, and involves formulating a complementary set of equations for the forward model, known as the adjoint equations. The method attempts to minimise the distance between the modelled and observed fields of interest (i.e. temperature for the mantle) by determining the 'gradient of the misfit' between these fields with respect to the initial condition of the model. A correction to the initial condition is then applied by a descent algorithm to minimise the distances at the final stage, with the whole process continuing iteratively to determine the initial condition that minimises the gradient. Courtier and Talagrand (1987) found that implementing this variational method in their models produced results consistent with meteorology, and produced non obvious, yet useful results from the assimilated observations.

Similar methods have been employed across a number of branches in other geoscience disciplines, including mantle dynamics beginning with Bunge et al. (2003). In mantle dynamics, the VAR method has been split into two categories depending on how it is applied; either solving an adjoint energy solution, or solving the adjoint for the full system of equations.

The simpler method involves computing an adjoint solution to the energy equation, as this is the only equation that is time dependent. Ismail-Zadeh et al. (2004) investigated using the adjoint energy equation on a cuboid domain to investigate the ability to reconstruct mantle plumes, determining that the adjoint method produced much smaller errors compared to the BAD method. Further work using an adjoint solution for the energy equation include; Liu et al. (2008) to investigate the subduction history of the Farallon slab back to $\sim$ 100 Ma, Shephard et al. (2010) and Shephard et al. (2012b) where the influence of dynamic topography on the drainage of water in South America was tested. These three studies utilised regional three-dimensional regions and incorporated present day seismic tomography as their observed field.

The more complex application of the VAR method involves solving all three of the forward equations backwards in time using their complementary adjoint equations. This is the method outlined by Bunge et al. (2003), where the authors solved the system of equations on a global domain over 100 Myr. Here they attempted to reconstruct an initial condition for a synthetically calculated observed state. They equally found their VAR solutions to be

vastly superior to BAD solutions when comparing the RMS of temperature residuals between the modelled and observed fields. In Horbach et al. (2014) the full adjoint equations are once more tested, and the authors found that regardless of the initial guess for the initial condition, that given a prescribed surface velocity boundary condition the VAR method would yield the same best guess initial condition. Vynnytska and Bunge (2014) established the link to convergence for a VAR model if the models are run with assimilated surface veloctity boundary conditions. The difference between these two VAR method formulations means that the approach that only calculates the adjoint solution for the energy equation is much less computationally expensive, as it does not involve solving the Stokes equation.

Another method for solving our inverse problem is through the quasi-reversibility (QRV) method (Lattès and Lions 1969). This method involves introducing an additional term into the backwards energy equation, which allows the problem to be well-posed. This additional term consists of a higher order derivative on the temperature field together with a small regularisation parameter to ensure the term is small in comparison to the other terms. The inclusion of this extra term also requires extra boundary conditions to allow the problem to be solved. Solutions of this QRV energy equation are stable and can converge to the forward energy equations solution in certain spaces. Ismail-Zadeh et al. (2007) analyse the QRV method to both BAD and VAR finding that the BAD method only produces accurate reconstructions in advection dominated regions, whereas both VAR and QRV yield results everywhere. Furthermore, they find that regardless of method used, the time interval over which we can accurately reconstruct past mantle structures are limited by the characteristic thermal diffusion time $t \approx D^2/\kappa$, where D is the characteristic length of a feature, and κ the thermal diffusivity. This system is again simpler to solve than the full adjoint system, as again no solution is required for the Stokes system in the backwards calculation. Beyond the cartesian box synthetic tests of Ismail-Zadeh et al. (2007), Glišović and Forte (2014) employ the QRV method in three-dimensional spherical geometry to reconstruct the past 65 Myr mantle history to investigate the dynamics of deep mantle structures over that time period. They found good match between their final modelled and observed states, with errors between the two states falling within 10%.

Developing the QRV method into numerical codes, in comparison to both VAR (broadly the same as the forward code) and BAD (altering the

sign/omitting terms in the energy equation), requires significant changes to existing numerical codes to incorporate it into a forward-inverse workflow. With this in mind, we elect to develop the variational method for solving the inverse problem. We will focus on the full adjoint system, as whilst the adjoint energy only method is computationally simpler, it ignores a significant portion of the problem by discounting the mass and momentum equations. In the following section we shall outline the equations and workflow for the full adjoint equations for mantle convection.

4.3 The full adjoint equations for mantle convection

We recall from section 2.2 that the equations for incompressible mantle convection are;

$$\nabla \cdot \boldsymbol{u} = 0 \tag{4.1a}$$

$$\nabla \cdot \left(\eta\{\nabla \boldsymbol{u} + (\nabla \boldsymbol{u})^T\}\right) - \nabla P + \alpha\rho(T_{\text{av}} - T)\boldsymbol{g} = 0 \tag{4.1b}$$

$$\frac{\partial T}{\partial t} + \boldsymbol{u} \cdot \nabla T - \kappa \nabla^2 T - H = 0, \tag{4.1c}$$

with boundary conditions on the velocity field

$$\boldsymbol{u}_{tan}(x,t) = \boldsymbol{u}_P(x,t) \quad x \in S,\ t \in I \tag{4.2a}$$

$$\left(\left(\nabla \boldsymbol{u}(x,t) + (\nabla \boldsymbol{u}(x,t))^T\right) \cdot \boldsymbol{n}(x)\right)_{tan} = 0 \quad x \in C,\ t \in I \tag{4.2b}$$

$$\boldsymbol{u}(x,t) \cdot \boldsymbol{n}(x) = 0 \quad x \in \partial V,\ t \in I, \tag{4.2c}$$

pressure field

$$P(x,t) = 0 \quad x \in S, t \in I, \tag{4.3}$$

and temperature field

$$T(x,t) = T_S(x,t) \quad x \in S,\ t \in I \tag{4.4a}$$

$$T(x,t) = T_C(x,t) \quad x \in C,\ t \in I; \tag{4.4b}$$

together with the initial condition for the temperature

$$T(x,t_0) = T_0(x) \quad x \in V. \tag{4.5}$$

It is from this set of equations that the set of adjoint equations used in this work are formulated. As previously mentioned the full set of adjoint equations for mantle convection have been derived using Lagrangian multipliers (Bunge et al. 2003; Vynnytska and Bunge 2014) and more recently using an operator approach in Hilbert spaces for both incompressible (Horbach et al. 2014) and compressible (Ghelichkhan and Bunge 2016) mantle convection. While the full derivation of the adjoint equations for incompressible flow is not presented here, the derivation as detailed in Horbach et al. (2014) is reproduced in appendix B.

We will present the results of this derivation now, including the required boundary and initial conditions. For a more complete understanding of the assumptions taken in the formulation of the adjoint system, including to see where the adjoint equation boundary conditions stem from, the reader is encouraged to look through the derivation.

The complementary set of adjoint equations for incompressible mantle convection are as follows

$$\nabla \cdot \boldsymbol{\phi} = 0 \tag{4.6a}$$

$$\nabla \cdot \left(\eta \{ \nabla \boldsymbol{\phi} + (\nabla \boldsymbol{\phi})^T \} \right) - \nabla \psi + \tau \nabla T = 0 \tag{4.6b}$$

$$\frac{\partial \tau}{\partial t} + \boldsymbol{u} \cdot \nabla \tau + \kappa \nabla^2 \tau + \alpha \rho \boldsymbol{g} \cdot \boldsymbol{\phi} = \partial_T \chi(T), \tag{4.6c}$$

where $\boldsymbol{\phi}$ can be seen as the adjoint velocity, ψ the adjoint pressure and τ the adjoint temperature. $\partial_T \chi(T) = (T_\mathrm{t} - T_\mathrm{m})\delta(t - t_1)$ is the gradient of the misfit function χ, where T_m is the temperature structure from a mantle *model* and T_t the *true* temperature state inferred from sources such as seismic tomography.

Equation (4.6) has its own boundary conditions; for the adjoint velocity field

$$\boldsymbol{\phi}_{tan}(x,t) = 0, \quad x \in S, t \in I \tag{4.7a}$$

$$\left(\left(\nabla \boldsymbol{\phi}(x,t) + (\nabla \boldsymbol{\phi}(x,t))^T \right) \cdot \boldsymbol{n}(x) \right)_{tan} = 0, \quad x \in C, t \in I \tag{4.7b}$$

$$\boldsymbol{\phi}(x,t) \cdot \boldsymbol{n}(x) = 0, \quad x \in \partial V, t \in I, \tag{4.7c}$$

the adjoint pressure field

$$\psi(x,t) = 0, \quad x \in \partial V, t \in I, \tag{4.8}$$

the adjoint temperature field

$$\tau(x,t) = 0, \quad x \in \partial V, t \in I. \tag{4.9}$$

We also impose an initial condition for the adjoint temperature structure

$$\tau(x,t_1) = 0, \quad x \in V. \tag{4.10}$$

The similarities between the forward and adjoint systems are readily apparent. First the mass equation for both forward (eq. (4.1a)), and adjoint (eq. (4.6a)) are identical.

For eqs. (4.1b) and (4.6b), the momentum equations, we again note that the first two terms are identical. The term analogous to the buoyancy term in the forward equation is present in the adjoint energy equation, and instead a term that couples the adjoint equations to the forward equations through the use of the forward temperature field is involved in this equation.

The two energy equations (eqs. (4.1c) and (4.6c)) also display considerable similarity. We note that the sign of the adjoint diffusion term is reversed, which allows the adjoint energy equations solution to remain stable through the backwards time integration. There is also the presence of the forward velocity field $\boldsymbol{u}$ in the second term, further coupling the adjoint equations to the forward equations. The fourth term here can be viewed as a 'buoyancy like' term, whilst on the right hand side of the equation we have the term $\partial_T \chi(T)$. This can be interpreted as a forcing term involving the residual of the present day modelled and true temperature states, and in essence applies this residual as an initial condition on the adjoint calculation.

The boundary conditions on the forward and adjoint equations also show a striking similarity. For the velocity field we assume the same free slip on the CMB boundary (eq. (4.7b)), no-penetration condition at both boundaries (eq. (4.7c)), while for the surface we assume that there are no errors in our plate motion history model from the forward model and so set these velocities to zero for the adjoint calculation (eq. (4.7a)). Similarly for the adjoint temperature field, we assume that our fixed boundary values from the forward model are perfect and therefore as we have no errors to minimise on the boundary, set these to zero (eq. (4.9)).

The overall similarity between the forward and adjoint equations means that implementing the adjoint equations in a mantle convection code is

fairly straightforward. Of course the presence of terms from the solution of the forward equations in the adjoint equations means that the two systems are intimately linked. This means that we are required to run a forward calculation, saving the velocity and temperature fields as we go for use in the following adjoint calculation. As this method looks to minimise the errors on the temperature field we look to perform successive forward-adjoint calculations to achieve this.

With the adjoint equations derived, we can now look to implement them into an iteration scheme for solving the coupled forward-adjoint system within the TERRA framework.

For the remainder of this thesis we shall adopt certain notation for variables to denote iteration numbers, the time point in the calculation, and the source of the data. The convention for indexing of variables $\cdot_m^n$ is as follows; superscripts denote the iteration number of the forward-adjoint calculation with $n \in \mathbb{N}_1$ and N denoting the final, optimal iteration; subscripts meanwhile denote the initial $m = 0$ or final $m = 1$ point in time of the model relative to the forward calculation. That is to say $m = 0$ refers to some point in the past from present day, regardless of whether discussing forward or adjoint variables. Surplus to this subscripts may also take the letter m or t; where m refers to the *model* data source obtained from a forward calculation; and t refers to the external *true* data source which is used as the target field.

4.4 The adjoint implementation in TERRA

A general overview of the necessary workflow when running a forward-adjoint is shown in fig. 4.1. We see that in essence an iteration can be broken down into four stages; a forward calculation, computation of the residual, the adjoint calculation, and updating the initial condition. We will now proceed to go into depth how each step is handled within TERRA, as simply implementing the adjoint equations is only half the battle to achieving a successful forward-adjoint iteration scheme.

Performing the forward-adjoint also requires many different outputs of data for use at different points of the calculation. Table 4.1 outlines the different I/O files that are required, and during the following discussion it is highlighted when each file type is used.

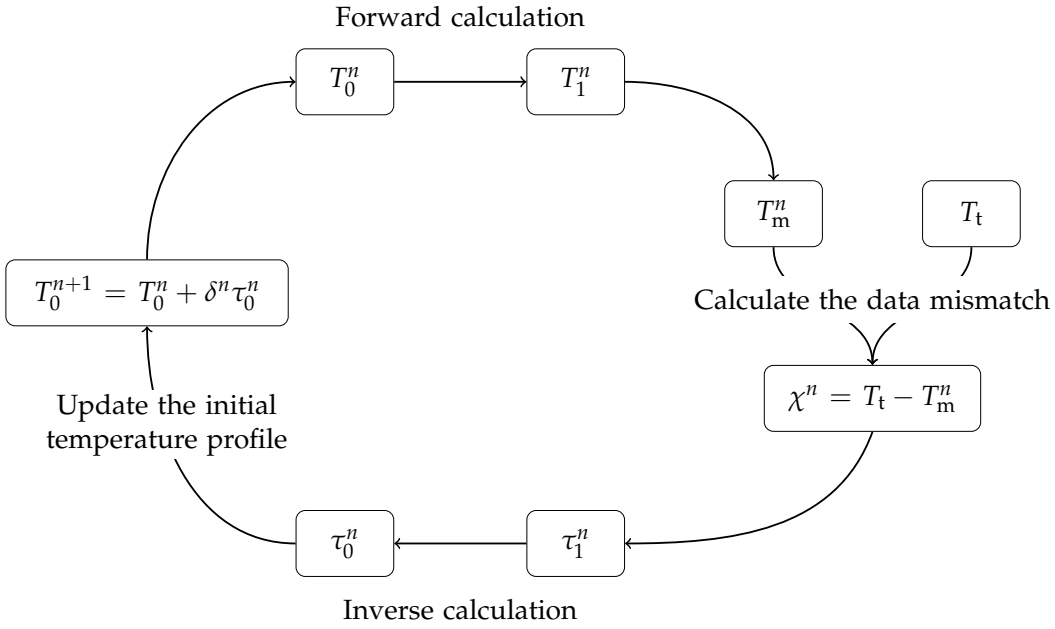

Fig. 4.1 The generic adjoint workflow

Type	Full filename structure	# outputs per iteration
Adjoint files *a-files*	`a<casenum>.<adj_iter>_<dump_number>.<nproc>`	100 to 10 000
Backward files *b-files*	`b<casenum>.<adj_iter>_<nproc>`	1
Difference files *d-files*	`d<casenum>.<adj_iter>_t<endpoint>.<nproc>`	2/3
Endpoint files *e-files*	`e<casenum>.<adj_iter>_t<endpoint>.<nproc>`	2
Residual files *r-files*	`r<casenum>.<adj_iter>_<nproc>`	1
True files *t-files*	`t<casenum>_t<endpoint>.<nproc>`	none

Table 4.1 Summary of different input and output files used during a forward-adjoint iteration

4.4.1 The forward model

To begin a new forward-adjoint calculation we initialise a TERRA forward model with some temperature field T_0^1. This temperature field is saved in what TERRA calls *e-files*, as it will be used later when updating the initial temperature field. This is then run forward to present day like a normal circulation model using eq. (4.1) together with plate motion histories. Extra to the standard MCM setup, at the end of each time step the following additional information is also output:

- The three-dimensional velocity field $\boldsymbol{u}$ which is required in eq. (4.6c)
- The one-dimensional temperature field T which is needed in eq. (4.6b)
- The length of the current time step and the current age of the model at that point. This is because the adjoint model must progress back to the starting age at the same rate as the forward model progressed such that the $\boldsymbol{u}$ and T fields are used at the same point in the adjoint. From this it can be deduced that an adjoint calculation will contain the same number of iterations as the forward calculation that came before it.

At the upper limit, during a standard circulation run a TERRA run could be outputting up to two hundred data files in ascii format containing velocity, temperature, pressure and other parameters totalling $\approx 100\,\mathrm{GB}$ at $mt = 256$. For the forward-adjoint calculation the number of outputs required extends from the thousands to tens of thousands. Outputting $\boldsymbol{u}$ and T at this rate puts a substantial strain on storage space on a system, and so requires this data to be output in binary to be as lean on space as possible (outputting files as binary saves between a factor of 4 to 8 on disk space). These files are referred to in TERRA as *a-files*. At $mt = 128$ a single time step of *a-files* requires $\approx 0.36\,\mathrm{GB}$ of storage, while at $mt = 256$ we require $\approx 3\,\mathrm{GB}$. A 200 Myr mantle circulation calculation typically takes $\sim$5000 time steps at $mt = 128$, and $\sim$10 000 at $mt = 256$. Therefore we require $\approx 2\,\mathrm{TB}$ or $30\,\mathrm{TB}$ of disk space respectively for storage of a single iteration.

4.4.2 Mismatch calculation

At the completion of the forward iteration we now have the temperature profile $T_1^n = T_\mathrm{m}^n$. which is output to a second set of *e-files*. Of course, we

also need our true data source T_t to calculate the residual. At this point the temperature field T_t is read in from an external file, typically a temperature field which is contained in what we call *t-files*.

As the forward-adjoint method can be used with any data source, so long as the mismatch calculation is sufficiently thought out, there are many potential options to use as the present day observation data (e.g. geoid, heat flux, seismic tomography). For this body of work we interest ourselves in two different sources for T_t. The first uses a temperature profile from a second independently run MCM calculation which then follows the iteration outline of fig. 4.1. Alternatively we may use a temperature structure derived from seismic tomography. When using seismic tomography as our data source we need to account for the resolution smearing that is present in the tomography in our model temperature T_m, and so extend our workflow to accommodate this. An outline of this expanded workflow can be seen in fig. 4.2, with the details of the new mismatch workflow as follows.

1. Convert the TERRA temperature T_1^n to seismic velocities $V_{s,1}^n$ using the (P, T) lookup tables of Stixrude and Lithgow-Bertelloni (2011) (see section 2.5)

2. Filter these velocities to account for first, the model parametrisation, and secondly the uneven geographic data coverage and the damping and smoothing applied in the tomographic inversion. As previously discussed (section 2.5) such a resolution filter is currently only available for the S-wave tomography models of S40RTS (Ritsema et al. 2011) and its lower resolution predecessor, S20RTS (Ritsema et al. 2004).

3. With both $\mathcal{R}(V_{s,1}^n)$ and $\mathcal{R}(V_{s,t})$ (where $\mathcal{R}$ denotes the resolution matrix of the tomography) we then convert these back to a temperature field. For this we use a one-dimensional conversion with depth using the equation

$$T = T_{ref} - \frac{1}{\alpha} R \left(\frac{\delta V_s}{V_s} \right) \tag{4.11}$$

where T_{ref} is the reference mean temperature for a given layer taken from the circulation model, α is the coefficient of thermal expansion, $\delta V_s / V_s$ is the horizontal shear velocity perturbation. The value $R = \delta \log \rho / \delta \log V_s$ a density-velocity scaling relationship which controls the amplitude of the perturbation applied to the radial average temperature. Its value may be derived from mineral physics or can be calculated

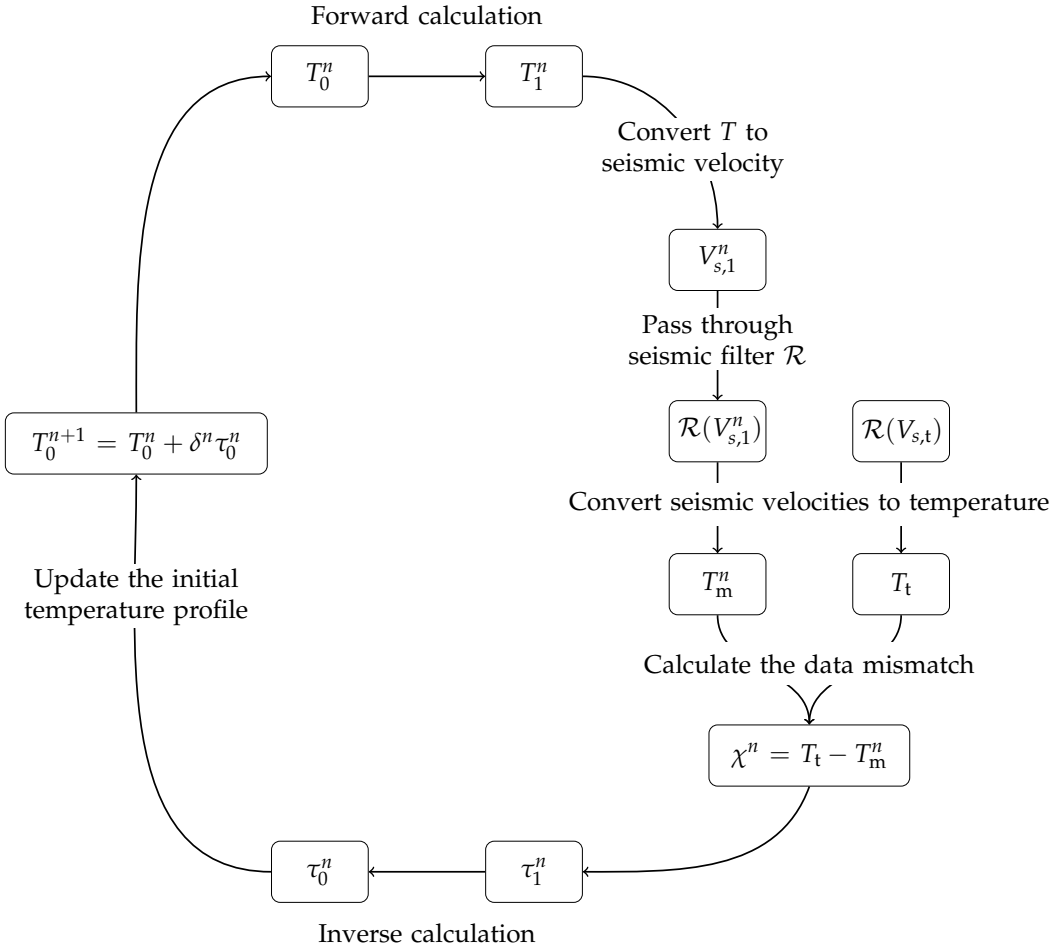

Fig. 4.2 The adjoint workflow using seismic data as the data source

dynamically from the proceeding MCM run (see section 2.5.1). A more complex conversion would be to use the same (P, T) lookup tables to map back from the seismic velocities to a temperature field. However, as previously discussed, as the mapping $(P, T) \mapsto V$ is non-unique the inverse is not straight-forward to calculate.

With both a temperature profile for the forward model $T_1^n = T_m^n$ and the true data source temperature profile T_t now available, the misfit for the current iteration, χ^n can be computed by

$$\chi^n = T_t - T_m^n. \tag{4.12}$$

The difference between the two sets of data is then output to *d-files*, and we compute L^2 norms of the difference, the difference in the upper mantle, and the difference in the lower mantle. If the L^2 norm of the whole domain

difference falls below some user determined threshold then the forward-adjoint iteration is considered converged. One final adjoint calculation is run and the initial condition that results from this is considered the optimal initial condition.

If we do not fall below this threshold then the iterations are not terminated and another forward calculation will follow the next adjoint iteration.

4.4.3 The adjoint model

At the start of the adjoint model the residual temperature field contained in the *d-files* is read in, as through the forcing term in eq. (4.6c) it is in essence used as the initial condition of the adjoint backward integration, together with the imposed temperature boundaries eq. (4.9). The age of the model and current time step length is then set to match that of the final iteration of the forward model and the adjoint calculation is carried out using eq. (4.6) and the matching *a-files*. Each time step length is set according to the corresponding forward time step length.

Once the adjoint model has progressed back to t_0, the adjoint calculation is completed and the adjoint solution is output to *b-files*.

4.4.4 Updating the initial condition

With the gradient of the cost function obtained we look to update our initial temperature profile T_0^{n+1} using a conjugate gradient approach (Fletcher and Reeves 1964). The first step involves

$$p^n = \begin{cases} \tau_0^n & \text{if } n = 1 \\ \tau_0^n + \left(\dfrac{||\tau_0^n||}{||p^{n-1}||} \right) p^{n-1} & \text{if } n > 1 \end{cases} \tag{4.13}$$

where p^n is a scaled vector of our adjoint solution which is written out to *r-files*.

With our scaled solution, the initial condition temperature field can be updated with the field obtained from from our adjoint integration by

$$T_0^{n+1} = T_0^n + \delta^n p^n. \tag{4.14}$$

Here $\delta^n \leq 1$ and is a damping factor which can be determined as a fixed value; by a simple function; or by more sophisticated methods, such as by a gradient function (Ismail-Zadeh et al. 2004).

The difference between T_0^{n+1} and T_0^n is output to *d-files* at this point together with L^2 norms of the whole, upper and lower mantle differences. Additionally if we are running a synthetic test case we output an additional set of *d-files* and norms for the difference between T_0^{n+1} and $T_{t,0}$, the initial condition of our true synthetic model.

Our new temperature field T_0^{n+1} is then written to a new set of *e-files* ready for use in the $n+1$ forward calculation.

4.5 A 10 Myr forward-adjoint test case

To conclude this chapter we will look at a synthetic example of a forward-adjoint calculation in order to validate the robustness of the method. To perform a synthetic test we will make use of a separate mantle circulation model that has been run in the standard MCM method for 200 Myr. We will then take as our true data source T_t the final output temperature field from this model. Since we are using an MCM as our true data source, we also have access to the temperature field for the whole of the MCM model in the past. As a consequence of this, when we run the forward-adjoint model over a given time period, we can compare the forward-adjoints optimal initial condition temperature field T_0^N to that of the MCM model at the same point in time $T_{t,0}$.

For our test case we ran an incompressible with radial viscosity model at a resolution of $mt = 128$. The model parameters used are outlined in table 4.2. The radial viscosity profile for the model is determined as follows:

$$\eta(r) = \begin{cases} 50\eta_0 & r \leq 100\,\text{km} \\ \eta_0 & 100\,\text{km} < r \leq 660\,\text{km} \\ 30\eta_0 & r > 660\,\text{km} \end{cases}$$

For this investigation we will look at setting the length of the forward-adjoint model t_0 to 10 Myr of plate motion histories. Calculations were terminated early if the residual L^2 norm of the calculations at t_1 fell below the value of 30 K. The temperature profile for T_0^1 is taken as a tetrahedral

Parameter		Value	Units
Surface temperature	T_S	300	K
CMB temperature	T_C	3000	K
Internal heating rate	H	4×10^{-12}	$\mathrm{W\,kg^{-1}}$
Reference viscosity	η_0	3×10^{22}	Pa s
Density	ρ	4500	$\mathrm{kg\,m^{-3}}$
Thermal expansivity	α	2.5×10^{-5}	$\mathrm{K^{-1}}$
Thermal conductivity	κ	4	$\mathrm{W\,m^{-1}\,K^{-1}}$
Specific heat capacity	C_V	1000	$\mathrm{J\,kg^{-1}\,K^{-1}}$
Rayleigh number	Ra_H	$\approx 2.5 \times 10^6$	–

Table 4.2 Model parameters

spherical harmonic temperature perturbation on top of a 1D temperature profile.

4.5.1 Results

In fig. 4.3 we plot the temperature residuals norms for both $T_{t,1} - T_1^n$ and $T_{t,0} - T_0^n$ for the 10 Myr calculation. Our test case shows excellent convergence at t_1 as can be seen from fig. 4.3b, where after 5 iterations the residual had already fallen by over 90% of the first iterations value. By the sixth iteration the convergence had reached such a point that the iterations were terminated as we had fallen below our predefined convergence limit. Due to this surprisingly excellent convergence rate, the calculation was then restarted in order to determine what value the residuals might converge to. It can be seen that by the 10th iteration, the temperature residual values had settled with the whole mantle residual remaining around 10 K. However, beyond the fifteenth iteration, there is a suggestion that the solution is beginning to diverge, which we believe to be down to an over correction of features. Despite this we still see our temperature residual remaining below our initial 30 K termination point.

From fig. 4.3 we see that the upper mantle sees less convergence compared to the lower mantle. This can be attributed to the fact that lithospheric features in our model are more difficult to resolve at the models resolution. Also as the thermal boundary layer makes up a larger percentage of the upper mantle volume compared to in the lower mantle, any differences in the residual temperatures due to the boundary layer will be more pronounced

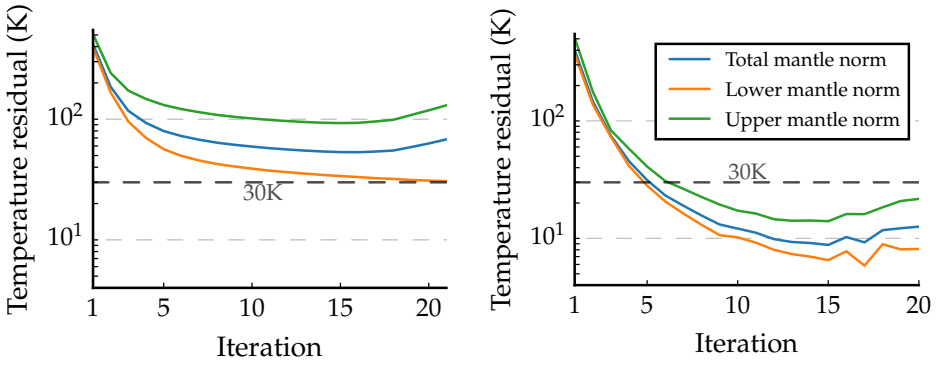

(a) t_0 **(b)** t_1

Fig. 4.3 L^2 norms for the residual temperature at t_1 and t_0 for successive forward-adjoint iterations

here. Subducted material collecting into the lower mantle as driven by the plate motion history could also attribute to this difference, since there will be a greater amount of features that are controlled by our surface boundary condition being driven into the mantle.

Figure 4.3a shows the temperature residual $T_{t,0} - T_0^n$ norms. We see that in comparison to the t_1 residuals the t_0 total mantle norm does not show the same rate of convergence. In the lower mantle we can see that our updated initial conditions continually converge towards the true initial condition state. The limiting factor on the whole mantle convergence is clearly based in the upper mantle reconstruction.

Figure 4.4 present snapshots of the temperature difference between the true and predicted initial state from near both boundary layers together with the mid mantle at t_0. Snapshots are for the differences following; the first iteration, the original termination point - iteration 5, the iteration from where the residuals settle down - iteration 10.

Looking in detail at the 180 km depth of our model we see in fig. 4.4a that following the initial iteration we have matched very little of the upper mantle structure. The differences between the sixth and eleventh iteration reflect the overall reduction in the norms at these iterations, but the regions of greatest mismatch are at the spreading ridges in both instances. We see that the slower spreading ridges such as in the Atlantic show a smaller positive anomaly region. The rest of the upper mantle region shows slight negative deviation from the true model.

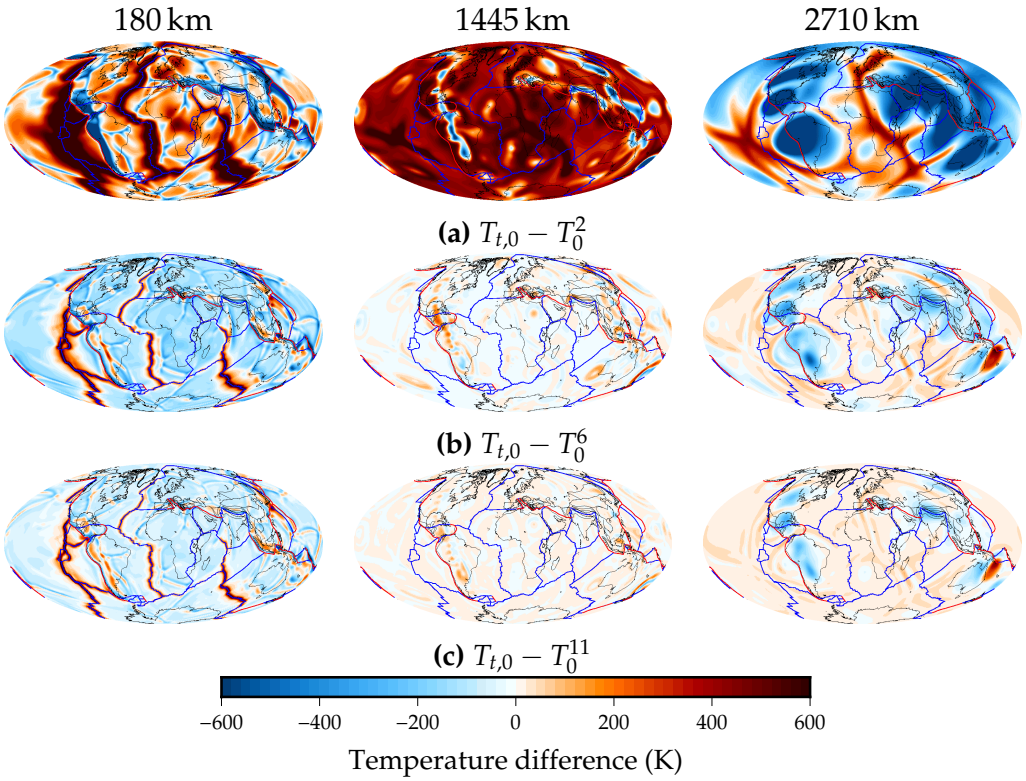

Fig. 4.4 Horizontal maps of the temperature difference $T_\mathrm{t} - T_\mathrm{m}$ from forward-adjoint model at various depths at t_0. Positive differences highlight regions that need to be hotter to match the true state, and negative differences regions that need to be cooler to match. Current coastlines (black) and tectonic boundaries (blue) and subduction zones (red) are included for reference.

We see the best match between the true data source and our model at the mid mantle at 1445 km. This is not unexpected as away from the thermal boundary layers the effects of diffusion, which cause the most issues in the inverse calculations, are much less pronounced. We see again that following our first iteration from the simple spherical harmonic initial temperature condition that the first iterations calculated initial condition contains lots of errors compared to our true data source (fig. 4.4a). By the time of the sixth iteration however, (fig. 4.4b), we can see that the only differences in the initial conditions are below the main subduction regions in Asia, and to a lesser extend the west coast of the Americas. By the completion of the tenth iteration, the temperature differences between T_0^{11} and $T_{t,0}$ are negligible.

In the lowermost mantle boundary, due to our short plate motion histories we fail to generate any meaningful structures by the conclusion of the first forward-adjoint calculation. But similar to the mid mantle, by the sixth

iteration the mismatch, with exceptions of the regions affected by subduction (around western America and central and eastern Asia), we see minimal deviation from zero temperature difference. This shows how the sensitivity of our calculated ideal initial condition to the starting initial condition is quickly resolved after only a few iterations. Again however, the initial conditions contain some significant mismatches even by the end of the tenth iteration, which again must be attributed to the location being located so near to the boundary of our domain.

4.6 Conclusion

Here we have validated the forward-adjoint iteration scheme against a known initial condition, such that we can be confident that the model works as hoped. At these short time scales, the rate of convergence is very pronounced as the initial forward model does not run long enough to generate any features even in the mid mantle; and so even two forward-adjoint iterations appear to yield incredible improvements. Extending the time scale of the model back further in time we would expect this rapid rate of convergence in the first few iterations to be somewhat negated by the model having enough time to generate some mid to deep mantle structures.

Furthermore for this 10 Myr forward-adjoint model, a single iteration ran for approximately 30 min. Each iteration took approximately 110 time steps and required on average 41 GB of storage for the full forward model *a-files*. From this we can determine that each time step requires roughly 370 MB at $mt = 128$; which when looking at longer timescale models of over 1000 time steps would equate to over 400 GB of storage for a single forward-adjoint iteration.

As we look to extend our models further back in time we can expect the trends shown in this synthetic case to be less pronounced and will have to account for the strain placed on storage space. To this end, we will continue the investigation of the outlined method in the following chapter.

Chapter 5

Profiling the robustness, efficiency and limits of the forward-adjoint model

Abstract

Knowledge of Earth's mantle into the past is inherently unknown. This lack of knowledge presents problems in many areas of Earth science, including in mantle circulation modelling (MCM). As a mathematical model of mantle convection, MCMs require boundary and initial conditions. While boundary conditions are readily available from sources such as plate reconstructions for the upper surface, and as free slip at the core-mantle boundary (CMB), the initial condition is not known. MCM have historically 'created' an initial condition using long 'spin up' processes using the oldest available plate reconstruction period available. Whilst these do yield good results when models are run to present day, it is difficult to infer with any confidence results from early in a models history. Techniques to overcome this problem are now being studied in Geodynamics, such as by assimilating the known internal structure of Earth at present day backwards in time. This is done using an iterative process known as the forward-adjoint method, which while an efficient means of solving the inverse problem still strains all but the most cutting edge computational systems. In this chapter we endeavour to profile the effectiveness of this method using synthetic test cases as our known data source. We conclude that savings in terms of computational expense for forward-adjoint models can be achieved by streamlining the time stepping of the calculation, as well as determining the most efficient method of updating initial conditions in the iterative scheme. Finally we

determine that a realistic limit of the time interval the method can be run over lies around 50 Myr.

5.1 Introduction

The adjoint method has been shown to be an excellent method of assimilating information in order to minimise the misfit between observed and predicted fields in a number of numerical modelling disciplines from meteorology (Courtier and Talagrand 1987) to seismology (Tarantola 1984) to oceanography (Menemenlis and Wunsch 1997). It has also been shown that this technique can be extended to address the problem of having an incomplete picture of Earth's mantle structure in the past (Bunge et al. 2003).

The adjoint method for mantle circulation models (MCMs) has previously been utilised using both synthetic (Bunge et al. 2003) and tomography derived (Horbach et al. 2014) true state forward-adjoint mantle models. Further studies using a simplified adjoint calculation have also been conducted (Ismail-Zadeh et al. 2004; Liu et al. 2008; Spasojevic et al. 2009), which use a subset of the full adjoint equations. In all of these studies, the interval over which the forward-adjoint iterations were ran spanned from 40 Ma to 100 Ma until present day. A possible reason for shorter timescale calculations could be due to hardware limits, as a high resolution forward-adjoint calculation requires in excess of 10 TB of hard disk storage for a single iteration running over a 40 Myr time interval, and takes several days to weeks of runtime (Horbach et al. 2014).

For an adjoint system using the full set of adjoint equations very little literature exists defining how reliable results are further back in time. Vynnytska and Bunge (2014) attempt to quantify this question of convergence using a two-dimensional forward adjoint model which did use the full system of adjoint equations. In this study the authors determined that knowledge of the surface boundary condition is crucial in order for the solution to converge to a unique initial condition, a result that they attribute to the uniqueness theorem of Serrin (1959). This states that two incompressible Stokes flows are equivalent given they have the same initial and boundary conditions. Their models investigated adjoint models running up to one-third of the transit time of mantle material, where they observed consistent converge for various time intervals up to this limit. Here we will look to expand on

the method of Vynnytska and Bunge (2014), by running a range of adjoint calculations and comparing them to a synthetic known mantle state.

Equally, the forward-adjoint formulation has a number of parameters that have not been tested for their influence on the convergence of the final solution. One source that has been investigated is the effect that the choice in first guess initial condition has on the solution convergence. Horbach et al. (2014) found that regardless of this first guess, from a one-dimensional temperature profile to unlikely temperature structures derived from tomography, all forward-adjoint models converge to the same global minimum.

Very low resolution investigations have also been made with a compressible forward-adjoint model by Ghelichkhan and Bunge (2016). In their study they compare a compressible and incompressible adjoint model to a compressible 'true' state reference. They found that due to the formulation of the compressible adjoint equations, there are only small differences between the incompressible and compressible adjoint solutions to the reference temperature field.

With the results of Vynnytska and Bunge (2014), Horbach et al. (2014), and Ghelichkhan and Bunge (2016) already found, we look to extend the investigation of the forward-adjoint method to cover more of the parameters that may control the convergence of solutions. In doing so we hope to understand better how the method can be altered to yield more efficient compute times and storage requirements without compromising the convergence.

We organise this chapter as follows: firstly we present the method used to solve the forward-adjoint system, including the equations, solution scheme and model setup. Then by computing synthetic initial and final states from a mantle circulation model to use as a benchmark for our forward-adjoint models, we investigate the effects on convergence of altering components of the forward-adjoint model. We will first investigate the role of the forward time step lengths on convergence; following this we will look at altering δ, the fraction used to update our initial state; finally with the availability of plate reconstructions that extend over 200 Myr we look at varying the time period over which the calculation is run to provide an upper bound on the time interval that can be used with this method.

5.2 Method

5.2.1 Numerical methodology

Mantle circulation models are carried out using an adapted version of the three-dimensional finite element code TERRA (Baumgardner 1985; Bunge et al. 1997), which solves the equations governing conservation of mass, momentum and energy (eq. (5.1)) for an incompressible fluid

$$\nabla \cdot \boldsymbol{u} = 0 \tag{5.1a}$$

$$\nabla \cdot \left\{ \eta (\nabla \boldsymbol{u} + (\nabla \boldsymbol{u})^T) \right\} - \nabla P + \alpha \rho (T_{av} - T) \boldsymbol{g} = 0 \tag{5.1b}$$

$$\frac{\partial T}{\partial t} + \boldsymbol{u} \cdot \nabla T - \kappa \nabla^2 T - H = 0 \tag{5.1c}$$

and the adjoint equations governing conservation of mass, momentum and energy (eq. (5.2)) for an incompressible fluid

$$\nabla \cdot \boldsymbol{\phi} = 0 \tag{5.2a}$$

$$\nabla \cdot \left(\eta \{ \nabla \boldsymbol{\phi} + (\nabla \boldsymbol{\phi})^T \} \right) - \nabla \psi + \tau \nabla T = 0 \tag{5.2b}$$

$$\frac{\partial \tau}{\partial t} + \boldsymbol{u} \cdot \nabla \tau + \kappa \nabla^2 \tau + \alpha \rho \boldsymbol{g} \cdot \boldsymbol{\phi} = \partial_T \chi(T). \tag{5.2c}$$

Here η is the dynamic viscosity, α is the coefficient of thermal expansion, ρ the reference density, T_{av} the radial temperature profile, $\boldsymbol{g}$ gravitational acceleration, κ is the thermal diffusivity and H is radiogenic heat production. $\partial_T \chi(T) = (T_{\mathrm{t}} - T_{\mathrm{m}}) \delta(t - t_1)$ is the gradient of the misfit function χ that relates the observed model temperature T_{m} to the observed true temperature T_{t}. $\boldsymbol{\phi}$, ψ and τ are the adjoint compliments to the forward terms $\boldsymbol{u}$, P and T.

These two sets of equations (eqs. (5.1) and (5.2)) are run together in an iterative loop with the temperature profile at t_0 updated using a conjugate gradient method (Fletcher and Reeves 1964),

$$T_0^{n+1} = T_0^n + \delta^n \tau_0^n. \tag{5.3}$$

Here δ is damping factor which is ≤ 1, the value of which can be varied over the calculation. Figure 5.1 outlines the full iteration loop, and is cycled over until the misfit at t_1 falls below a pre determined level, or the total number of iterations is exceeded.

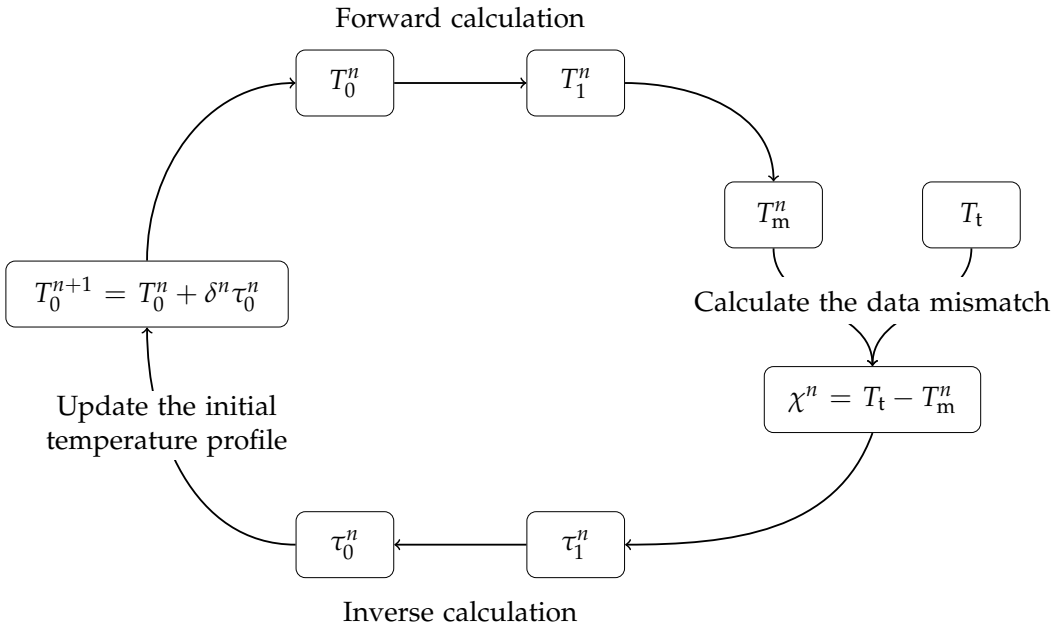

Fig. 5.1 The forward-adjoint workflow

5.2.2 Model configuration

All test cases were modelled as an incompressible fluid on a mesh with 10 million finite elements, which corresponds to an average grid spacing of 50 km. The viscosity profile employed in our models varies as a function of depth (r) only according to the function

$$\eta(r) = \begin{cases} 100\eta_0 & r \leq 100\,\text{km} \\ \eta_0 & 100\,\text{km} < r \leq 660\,\text{km} \\ 30\eta_0 & r > 660\,\text{km}. \end{cases}$$

Other key model parameters are outlined in table 5.1.

A free slip boundary condition is defined at the CMB, whereas surface velocities are prescribed using the plate motion reconstruction of Seton et al. (2012), with the velocities scaled to match the convective vigour of the underlying convection model. The surface velocities are assimilated in 1 Myr intervals over the course of our forward model calculations.

Parameter		Value	Units
Surface temperature	T_S	300	K
CMB temperature	T_C	3000	K
Internal heating rate	H	4×10^{-12}	$\mathrm{W\,kg^{-1}}$
Reference viscosity	η_0	3×10^{22}	Pa s
Density	ρ	4500	$\mathrm{kg\,m^{-3}}$
Thermal expansivity	α	2.5×10^{-5}	$\mathrm{K^{-1}}$
Thermal conductivity	k	4	$\mathrm{W\,m^{-1}\,K^{-1}}$
Thermal diffusivity	κ	1×10^{-6}	$\mathrm{m^2\,s^{-1}}$
Specific heat capacity	C_V	1000	$\mathrm{J\,kg^{-1}\,K^{-1}}$
Basally heated Rayleigh number	Ra_b	$\approx 5 \times 10^6$	–
Internally heated Rayleigh number	Ra_H	$\approx 9 \times 10^7$	–

Table 5.1 Model parameters

The Rayleigh number, the non-dimensional value which quantifies the convective vigour of the system that is basally heated is defined as

$$Ra_b = \frac{\alpha \rho \Delta T D^3 g}{\kappa \eta},$$

where D is the mantle radius and ΔT the total temperature contrast. As our models also contain internal heating we define a second Rayleigh number for an internally heated volume which is defined as

$$Ra_H = \frac{\alpha \rho^2 H D^5 g}{k \kappa \eta}.$$

Using the values used in this study this gives our models a Rayleigh numbers $Ra_b \approx 5 \times 10^6$ and $Ra_H \approx 9 \times 10^7$, meaning we expect the vigour of convection in our models to be slightly below what is expected for Earth. Because of this we scale the timescales of our models to allow a similar amount of convection to occur in the models presented here. All times used are after accounting for this scaling.

For our study into the limits, robustness and efficiencies of the forward-adjoint method we use a synthetically generated temperature field for our true data source, similar to the method used in Bunge et al. (2003). To generate this synthetic data source we begin with a mantle convection calculation (free-slip as the surface boundary condition) and run this until it has reached

a quasi-steady thermal state, such that the surface heat flux is fairly constant. Once this state has been reached the convecting mantle volume is conditioned with the oldest available plate motion stage to introduce the tectonic features of the stage. This is achieved by continuing the calculation for $\approx$ 50 Myr with the oldest plate stage, introducing the temperature and density anomalies in the upper to mid mantle from the plate stage. Following this setup we then run our reference model through to present day, recording the mantle structure at 10 Myr intervals. This is done so that as well as having a present day mantle structure to use directly in our adjoint calculation, we can compare the calculated initial stage mantle structure from our adjoint calculation to the synthetic case.

The main metric we use to compare different cases is the L^2 norm of the mismatch at t_0 and t_1. This gives us a measure of the distance between the modelled T_m, and true T_t, temperature fields, with lower values reflecting a smaller distance between the two fields.

For the different parameters we investigate in this study unless otherwise stated we use as default; a time stepping mechanism that is allowed to evolve freely, and a delta value of $\delta = 0.8$ in eq. (5.3).

We conclude by outlining the motivation and setup for each each of the different cases we considered in this work.

5.2.3 Altering the forward time step mechanism

Our first investigation concerns the time stepping mechanism of the forward calculation. We see from eq. (5.2) that the adjoint equations require knowledge of the forward iterations temperature and velocity values. This coupling of the two equations results in the adjoint calculation having to take the exact same time steps back in time as the freely evolving forward calculations time steps. The storage of the $\boldsymbol{u}$ and T arrays at each time step requires, depending on resolution, 0.4 GB to 3 GB of temporary storage for each time step. As calculations grow into the thousands of time steps, this can begin to push practical limits of storage available.

To this end, we hope that by constraining the forward time steps evolution we can achieve practical gains in terms of storage space and runtime without compromising the convergence of our solutions.

In its current implementation in TERRA, time stepping is performed using a second order Runge-Kutta scheme. The length of each time step

is adjusted as the calculation evolves, such that only one iteration of the code's multigrid algorithm is required to maintain the residual error in the solving of the momentum equation below a specified level. Furthermore, the length of each time step is bounded from above in order to ensure the Courant-Friedrichs-Lewy (CFL) condition is not violated. The time step is also controlled by the presence of any unstable temperature values for nodes located at the boundaries. The net result is a time step which will increase $\times 1.1$ if all tolerances are reached or $\times 0.8$ if one or more tolerances are not met. This method of time step evolution is the same as the one used in previous chapters as well as in our test case in section 4.5.

In order to investigate the effect that changing the time step evolution has on the convergence of the forward-adjoint we shall conduct two synthetic tests which cover 10 Myr and 40 Myr of Earth history respectively. We consider three methods of time step evolution:

- **Free** - This is the classic time step as found in TERRA and described above.
- **Upwards** - This limits the time step by taking the maximum value out of the previous and current time step values; this has the net effect of allowing the time step to increase when the tolerances are met but never decrease in value.
- **Forced** - In this implementation the time step is hard coded to the CFL limit apart from the first ten time steps of each 1 myr plate stage in order to allow the code to handle the change of plate boundaries.

5.2.4 Varying the choice of δ for the T_0^{n+1} update

At the end of a forward-adjoint iteration we update the initial condition guess by

$$T_0^{n+1} = T_0^n + \delta^n \tau^n \tag{5.4}$$

where δ is the damping factor that controls the influence of the adjoint temperature in the update process. A well chosen function for determining δ could have a significant effect on the rate of convergence of our solutions, resulting in fewer forward-adjoint iterations required to reach satisfactory results. This of course would have the additional benefit of less total storage

required, as well as shorter run times; both valuable when considering calculations run on large HPC systems.

In order to understand how the choice of δ affects the convergence of our forward-adjoint solution, we will conduct a series of synthetic forward-adjoint models running over a time period of both 10 Myr and 40 Myr. By running our tests using synthetic data we are able to directly compare the accuracy of our predicted initial condition for the different cases. For both of these time spans we consider the following for our choices for δ:

- $\delta = 1$ - A value where we apply the whole minimised adjoint field.
- $\delta = 0.8$ - A second fixed value addition of the adjoint field.
- $\delta = 1 - 0.02n$ - A simple decreasing function that ranges from 1 to 0.8 over the 20 iterations. Here n corresponds to the iteration number.
- $\delta = \dfrac{1}{n + n_0}$ - A decreasing function for δ as used in Liu and Gurnis (2008), where we choose $n_0 = 0$. Again n corresponds to the iteration number.
- $\delta = \min\left\{\dfrac{1}{1+n}, \dfrac{||\chi^n||}{||\tau_0^n||}\right\}$ - Here δ is determined based on the gradient method as in Ismail-Zadeh et al. (2004). n once more corresponds to the iteration number, χ^n the misfit between the true and model temperatures for the current iteration, and τ_0^n the adjoint temperature at t_0.

5.2.5 Varying the time interval of the forward-adjoint calculation

For our final investigation we shall look at how the time interval we run our forward-adjoint model over affects the residuals between the modelled and true temperature fields. As previously discussed, previous studies that looked at 3D forward-adjoint simulations ran over a time interval of 40 Myr to 100 Myr. Both Liu et al. (2008) and Bunge et al. (2003) ran adjoint models that extended back to 100 Myr, with the latter running a global model using the full adjoint system of equations. Bunge et al. (2003) ran their calculation for 100 forward-adjoint iterations and saw a reduction of 90% at t_1 and 50% at t_0. For our study we do not attempt to run for as many iterations due to the limits of the computational resource available for this work.

With the availability of plate reconstructions that extend back to the early Jurassic (Seton et al. 2012), we can therefore conduct forward-adjoint calculations over a time period of twice that of other studies. In doing so we hope to determine at what point, if any, information is not significantly propagated back in time using an adjoint calculation. We will run several cases covering a range of intervals; 10 Myr, 20 Myr, 40 Myr, 80 Myr, 120 Myr, 160 Myr and 200 Myr. As in our other test cases we will start all our models from the same 1D temperature structure.

5.3 Results

5.3.1 Altering the forward time step mechanism for the forward adjoint calculation

Figures 5.2 and 5.3 show the results for the different methods of controlling the forward time step for both the 10 Myr and 40 Myr calculations. For the 10 Myr (figs. 5.2a and 5.2b) calculation the t_0 profiles all display the same convergence to a minimum around 55 K globally before a small uplift in the norms is observed. At t_1 the choice of time step method does have some influence on the convergence, however these differences are $\mathcal{O}\sim 1$ K.

For the 40 Myr calculation we again see that the convergence of the different solutions very closely match each other both at t_0 and at t_1, as can be seen in figs. 5.3a and 5.3b. Similar to the 10 Myr calculation we see in fig. 5.3b that in the later iterations there is some variation in the L^2 norms $\mathcal{O}\sim 10$ K, although there is no noticeable favoured implementation. We also note that the minimum norm values at both end points are higher than those observed in the 10 Myr calculation. Finally we do not observe the small divergence of the L^2 norms in the later iterations at t_0.

As the aim of our testing of different time step controls is to maximise savings in storage and runtime without compromising our solutions we also present figures for both storage and runtime for each iteration. At 0.36 GB per time step at this resolution we see in figs. 5.2c and 5.3c that over the 10 Myr and 40 Myr calculations we require a fairly uniform amount of storage for each iteration of roughly 40 GB and 160 GB respectively. In both length calculations we see that the initial iteration shows a much higher storage requirement for the first iteration for the free and upwards methods. We

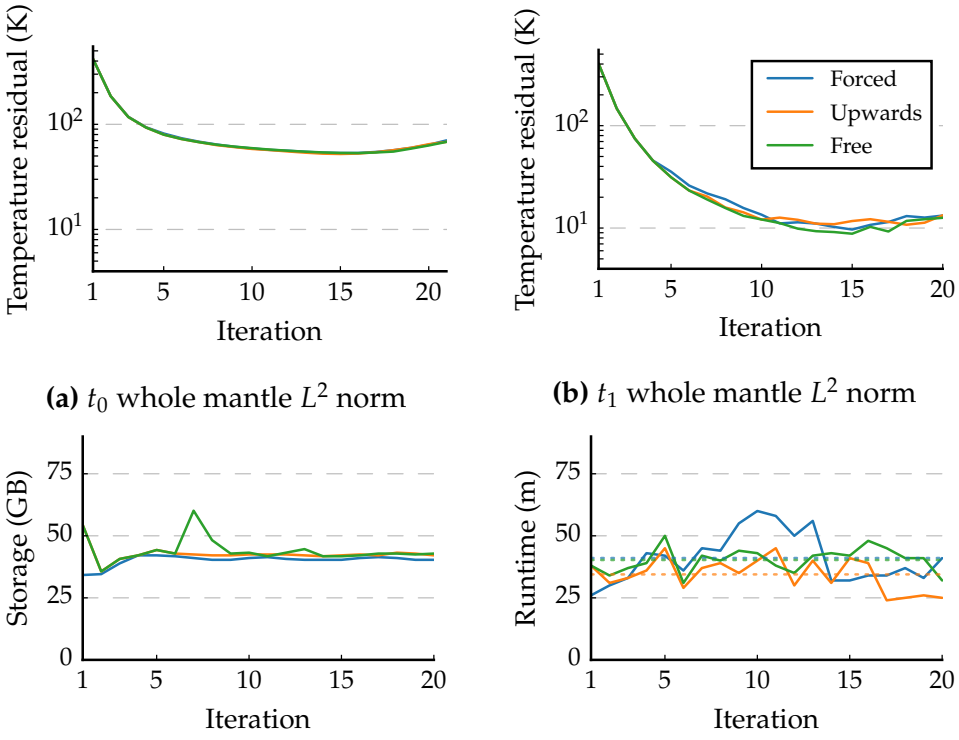

(a) t_0 whole mantle L^2 norm

(b) t_1 whole mantle L^2 norm

(c) Storage requirement per iteration

(d) Runtime per iteration

Fig. 5.2 Various line graphs for a 10 Myr synthetic forward-adjoint calculation with varying methods of time step evolution. (a) and (b) show the L^2 norms at both end members plotted on semi log axis. (c) displays the total hard disk storage required for information for each iteration. (d) is the total computation time required for each iteration with the average denoted by the dotted lines.

can interpret this as an effect of our choice of initial condition being a 1D temperature profile. As there is no information of the internal structure a freely evolving model will progress slowly as thermal structures are introduced into the model, which will limit the time step growth as the model copes with these structures. The forced time step method on the other hand ignores this and progresses at full pace, hence the smaller storage requirement in the first iteration. By the start of the second iteration some thermal structures have been introduced into all the test cases and so we see the similar storage requirement across all cases.

Turning to the runtime for our cases figs. 5.2d and 5.3d we see that the upwards time step performs best on average over both time intervals. Perhaps surprisingly, the forced time step does not outperform the others, and in the 10 Myr case we also see it perform noticeable worse for a period.

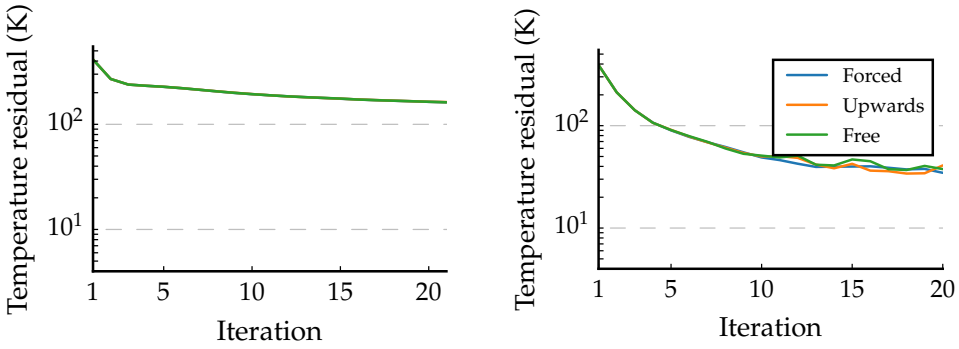

(a) t_0 whole mantle L^2 norm

(b) t_1 whole mantle L^2 norm

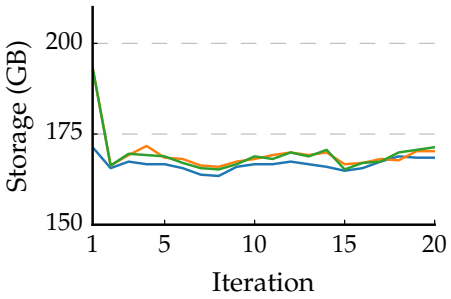

(c) Storage requirement per iteration

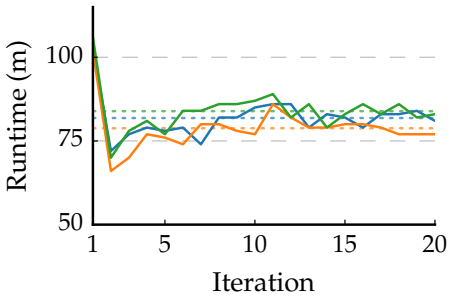

(d) Runtime (average in dotted lines) per iteration

Fig. 5.3 As fig. 5.2 but for the 40 Myr synthetic forward-adjoint calculations.

We attribute this to the case ignoring any difficult to solve regions in the volume, therefore requiring extra multigrid cycles in order to satisfy the convergence tolerances of the code.

5.3.2 Varying the choice of δ for the T_0^{n+1} update

The temperature residuals for all cases for various choices in δ are presented in fig. 5.4 and fig. 5.5. Regardless of calculation time period we see that the choices in δ can be split into two separate groups based on their convergence.

The first group contains the linear choices of δ. Focusing on the 10 Myr results first we see that the three cases can be characterised by a very similar convergence rate at t_1, fig. 5.4b, with each reaching a minimum norm value $\sim$10 K to 20 K for the misfit between the modelled and observed temperature field. While at t_1 we see some differences between these three choices of δ even early on, with $\delta = 0.8$ showing the best convergence, at t_0 all three cases show very similar convergence until iteration 10. Beyond this point $\delta = 1$ begins to quickly diverge, and our linear function show similar, but less

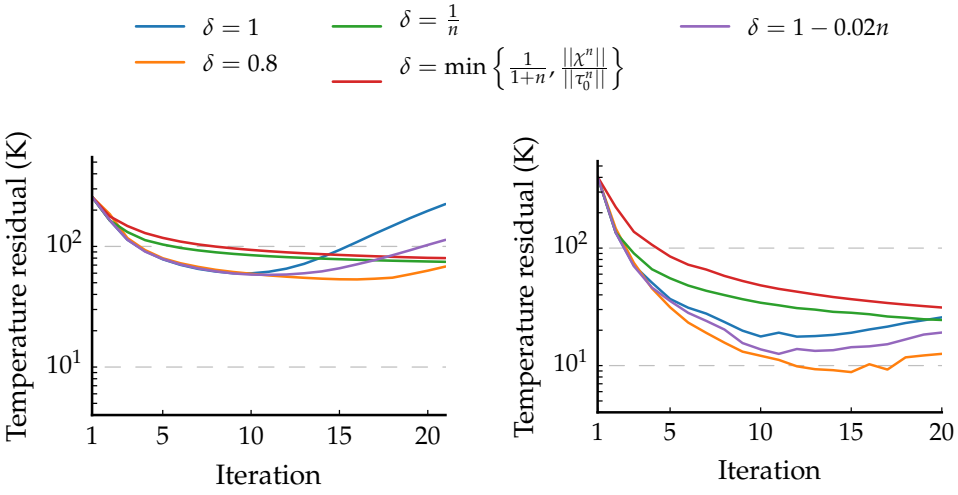

(a) t_0 whole mantle norm

(b) t_1 whole mantle norm

(c) t_0 upper mantle norm

(d) t_1 upper mantle norm

(e) t_0 lower mantle norm

(f) t_1 lower mantle norm

Fig. 5.4 Logarithmic plot of L^2 norms for the residual temperature at t_0 and t_1 for different δ implementations in a 10 Myr synthetic forward-adjoint.

pronounced behaviour. All three cases obtain a minimum of ∼50 K to 60 K. We can see from figs. 5.4c and 5.4e that this divergence of our misfit at t_0 is only observed in the upper mantle, with $\delta = 0.8$ actually being marginally worse that the other two choices in the lower mantle up until iteration 17. This is an unexpected result, which we attribute to the build up of an over correction of features located at the near surface, introduced by these choices of δ. The difference between the upper and lower mantle is not observed at t_1 however, as over the 10 Myr of forward model there is time to remove some of this over correction.

The second group contains the non-linear choices for δ. Both of these choices show a monotonically decreasing norm residual across both end points, a feature not shared by the first group. Whilst this may suggest a more stable convergence rate, we do see however that it is taking 20+ iterations for this group to begin falling below the minimum levels obtained by the first group. Across both the upper and lower mantle at t_1 they only just start to outperform the three choices from the linear group, namely $\delta = 1$. At t_0 we do not see the same divergence in the upper mantle due to over correction, but the minimum values after 20 iterations still fail to match the early norm levels of the linear δ group. We also see that $\delta = 1/n$ is consistently below the more complex non-linear function. From further investigation of this we found that the gradient determined by $||\chi^n||/||\tau_0^n||$ was larger than $1/1+n$ at all but the last two iterations. Because of this, the choice in δ was taken as the fraction $\frac{1}{1+n} < \frac{1}{n}$ and so explains the poorer convergence rate compared to the other non-linear choice.

For the 40 Myr calculations (fig. 5.5) the differences are less pronounced, but results still fall into the same two groups. We observe that at t_1 for four out of the five choices of δ, the temperature residuals continue to decrease across the 20 iterations obtaining a minimum value ranging from 30 K to 70 K at the twentieth iteration. The exception is $\delta = 1$ which begins to show a diverging final stage misfit from the twelfth iteration onwards. The minimum value obtained by this choice is worse than the other linear functions at this point, showing no advantage to this choice in δ. In contrast to the 10 Myr calculations, the best observed choice at t_1 is $\delta = 1 - 0.02n$, which shows a much more stable convergence compared to the next nearest which shows an oscillating norm value. From fig. 5.5f we see that this oscillation for the 0.8 choice is actually from contributions in the lower mantle.

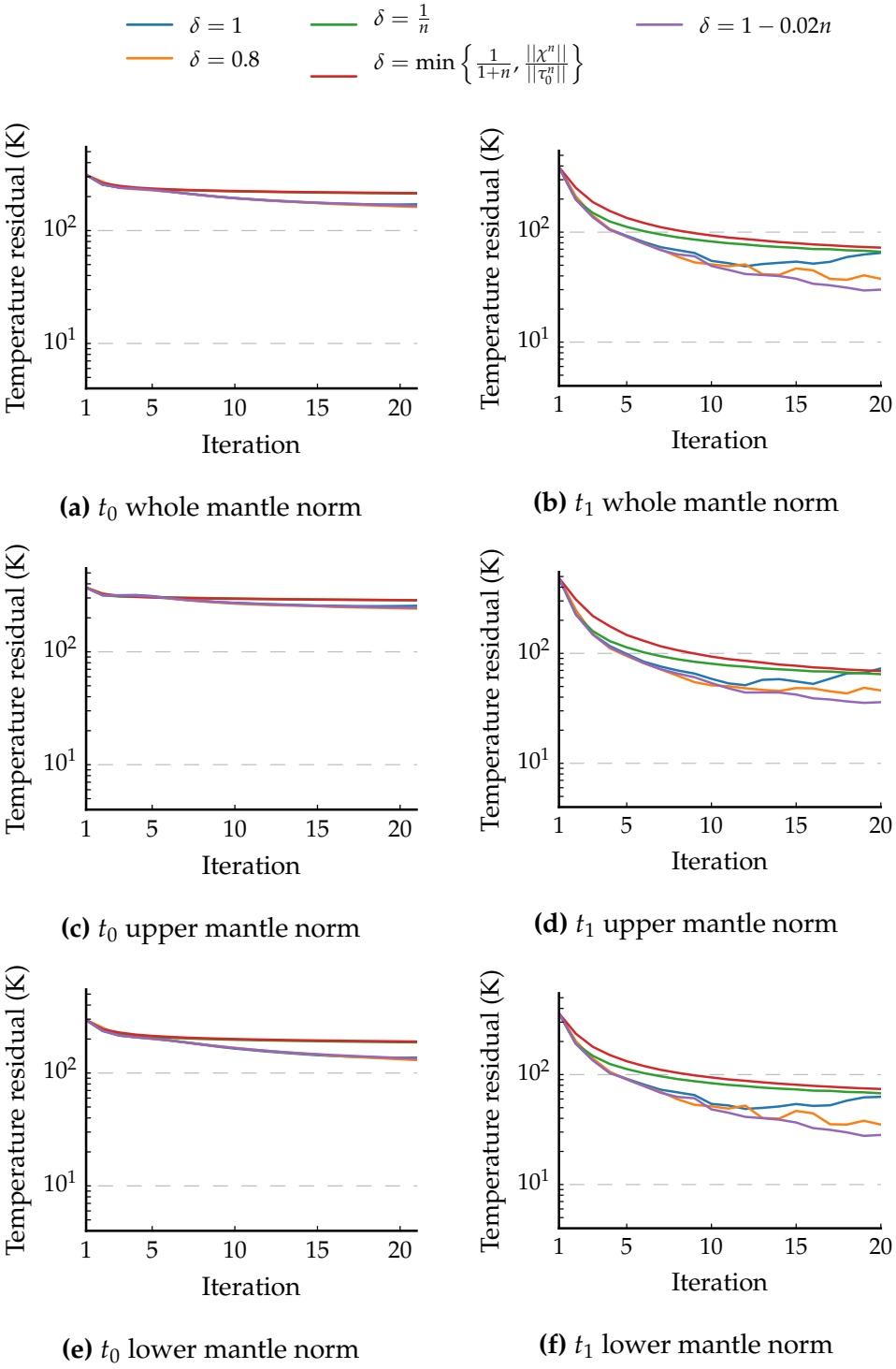

(a) t_0 whole mantle norm

(b) t_1 whole mantle norm

(c) t_0 upper mantle norm

(d) t_1 upper mantle norm

(e) t_0 lower mantle norm

(f) t_1 lower mantle norm

Fig. 5.5 Logarithmic plot of L^2 norms for the residual temperature at t_0 and t_1 for different δ implementations in a 40 Myr synthetic forward-adjoint.

The picture at t_0 is much less diverse, with the values at each iteration for the differing choices of δ falling into the two previously mentioned groups of linear and non-linear (fig. 5.5a). All the values show a monotonically decreasing residual, though the non-linear choices are decreasing by only a few K over the last ten iterations. The minimum values obtained range over a region of 160 K to 220 K. As expected the upper mantle norms are worse than the lower mantle (figs. 5.5c and 5.5e); however, we do not see the same behaviour as we did for the 10 Myr runs where some of the choices for δ would begin to diverge as the iterations continued. This is attributed to the t_0 predicted field not being over corrected as less information is available to update the initial condition as the length of the calculation time span is extended.

5.3.3 Varying the time interval of the forward-adjoint calculation

The temperature residuals at both t_0 and t_1 for these models are presented in fig. 5.6. The first feature we notice from the t_1 residual norms is that following the first forward calculation we see a range of values for the different length calculations. This is unsurprisingly arranged in order with the shortest test case showing the greatest difference from the reference state, to the full 200 Myr model which has a residual norm nearly half of the worst. We attribute this difference to the vastly different length assimilation times of our models, as having a long period of surface boundary conditions has previously been shown to provide a good match to present day observations (Bunge et al. 2002). Looking beyond the first iteration we see that by the end of the second forward iteration that the shorter length models are already displaying the best match to the observed mantle field, and by the fifth iteration the models have reordered completely in terms of best match. Over the course of the twenty iterations we see very small reductions in the residuals of the longest length calculations whereas the short time scale models show an excellent match. We also observe that all the models $\leq$80 Myr show continuing convergence while those $\geq$120 Myr appear to reach their minimums and oscillating about a final value.

Looking at the temperature residuals observed at t_0 between the predicted initial condition and the reference we see a vastly contrasting picture. Figure 5.6a shows that all models >40 Myr achieve their minimum misfit

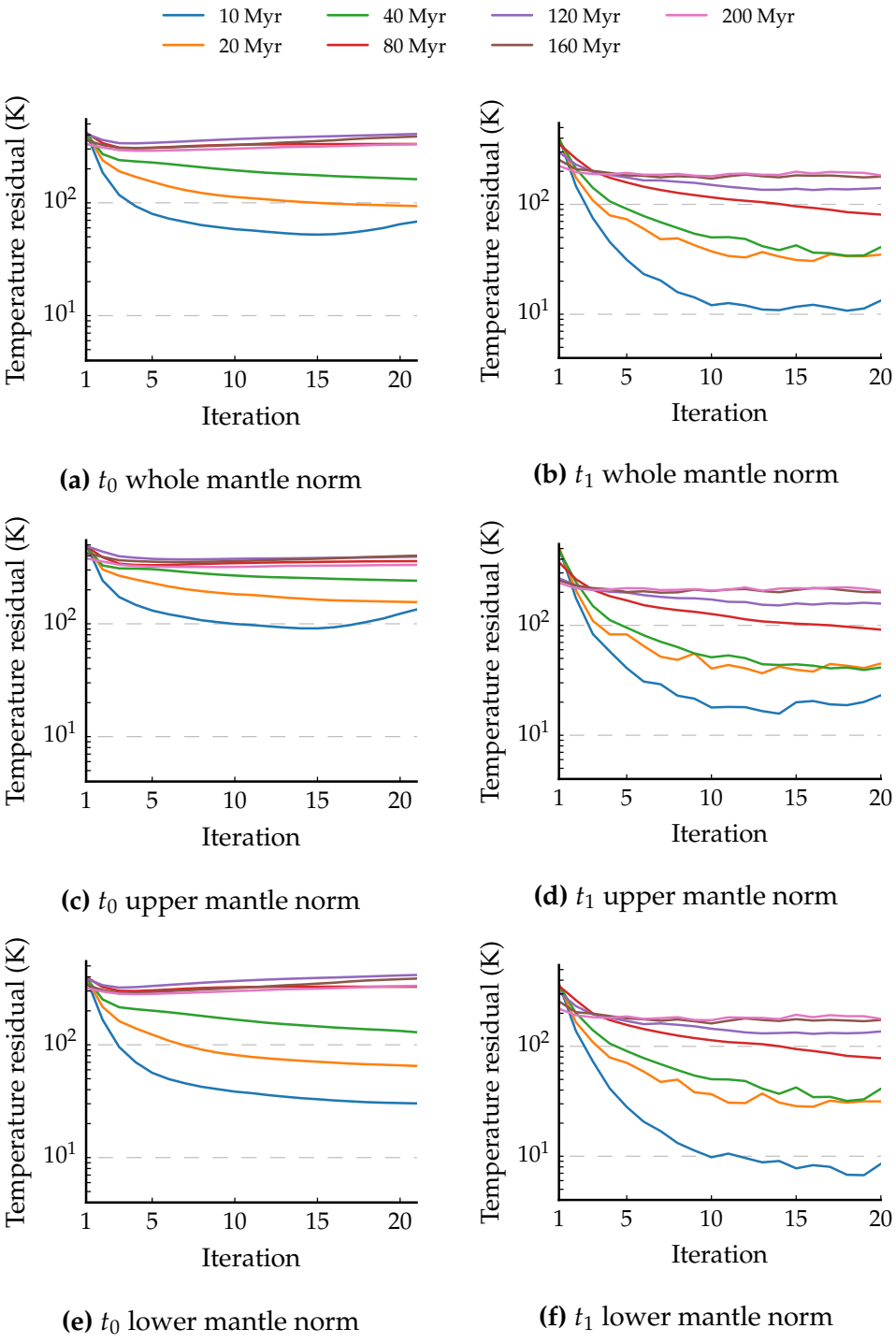

(a) t_0 whole mantle norm

(b) t_1 whole mantle norm

(c) t_0 upper mantle norm

(d) t_1 upper mantle norm

(e) t_0 lower mantle norm

(f) t_1 lower mantle norm

Fig. 5.6 Logarithmic plot of various L^2 norms for the residual temperatures of forward-adjoint models run over differing time intervals as a function of forward-adjoint iterations.

following three forward-adjoint iterations before seeing their norms steadily climb. For iteration 1 with our 1D radial temperature field, we see that the longest calculations, 200 Myr and 160 Myr, have a smaller misfit compared to the other cases. This could stem from the total length of the plate reconstruction model available to us together with how the reference model was calculated. We recall that the reference model is created by conditioning a plain mantle volume with the oldest plate stage for up to 50 Myr before the sequential assimilation of the full plate reconstruction. The reduced misfit values for the 200 Myr and 160 Myr for T_0^1 suggests that the standard method of setup for a forward model, as used for the reference state, provides a mantle volume that is still fairly heterogenous.

Unlike the t_1 residuals, we see that the t_0 residuals are not arranged from shortest to longest assimilation periods. While 10 Myr, 20 Myr and 40 Myr are arranged in order, the next best fitting model is the 200 Myr and 80 Myr respectively with the 120 Myr calculation showing the worst misfit values across the whole calculation. As expected we see better convergence in the lower mantle (figs. 5.6e and 5.6f) compared to the upper mantle (figs. 5.6c and 5.6d), although both regions do show the same overall convergence behaviour.

To further aid our understanding of our results, in fig. 5.7 we present snapshots of some of the adjoint derived initial conditions for a number of total forward-adjoint iterations together with the reference model which we hope to match with. The excellent convergence of the misfit observed previously for the 10 Myr calculation is apparent here with minimal visual difference by the fifth iteration. The reconstructed initial condition displays the same subducting features together with similar lithospheric thickening. Further iterations show very little change in the features despite further decrease in the residuals.

The selected snapshots at 40 Myr show a good match from the fifth iteration with an improving picture in the subsequent images. The region located at 90° east shows a less accurate match though we conclude that the broad structure is correct. At 80 Myr we see similarly that the eastern side of our cross sections again appear to be less accurate to our observed state.

As we look towards our longer time spanning cases we see the power of features introduced in the first few iterations are very low and broad in comparison to the shorter cases. This is particularly pronounced between 120 Myr and 160 Myr where the former shows more defined features com-

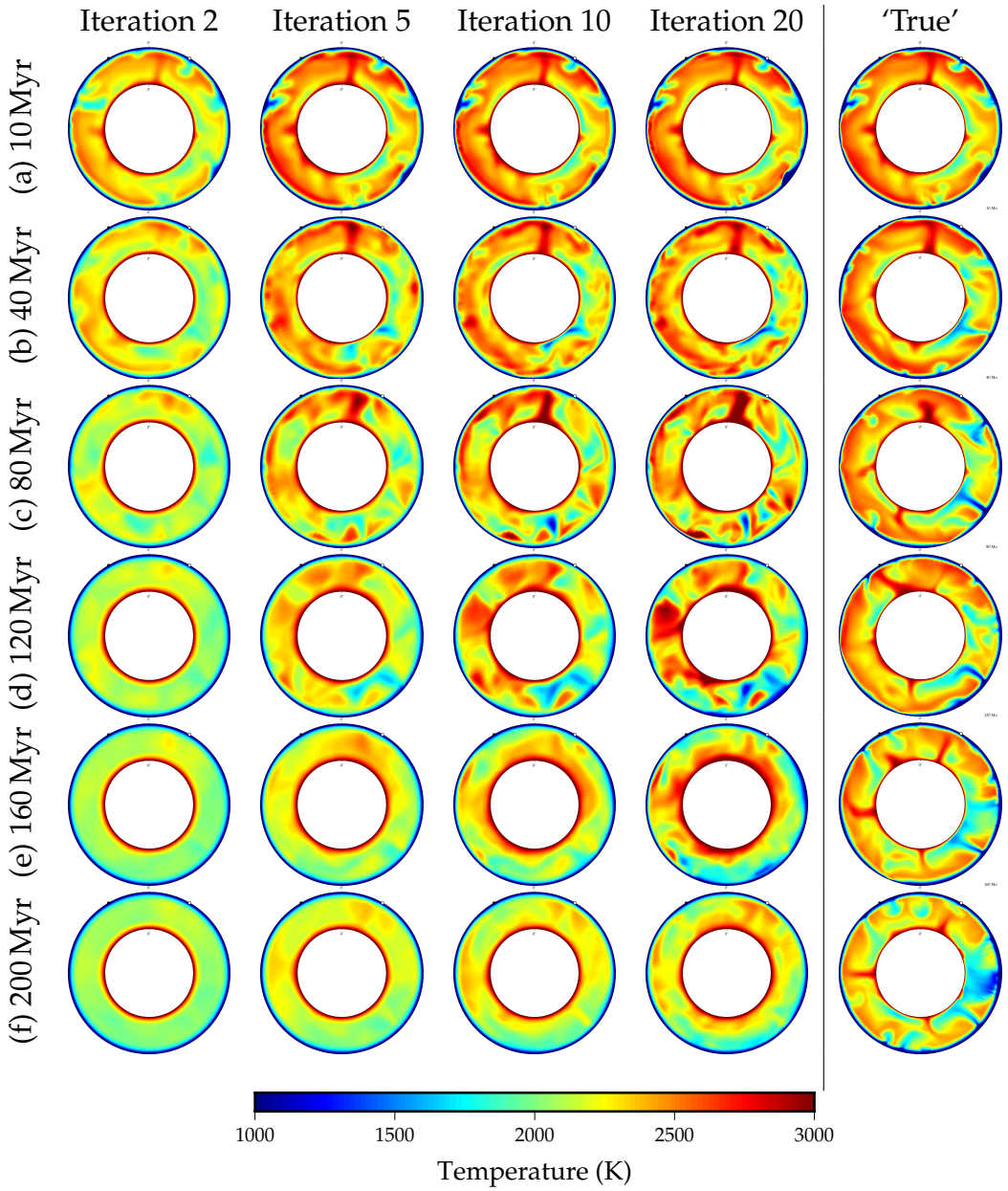

Fig. 5.7 Cross section plots through the equator at t_0 for various time intervals forward-adjoint calculations. A range of iterations are shown together with the expected 'true' mantle structure taken from a separate MCM calculation.

pared to the latter. Considering this together with the knowledge that the 120 Myr case showed the worst match to the reference state, we conclude that by having less pronounced features in the longer cases results in less dramatic shifts from the observed state and hence the observed anomalous ordering in the t_0 residuals.

5.4 Discussion

By conducting synthetic tests of the forward-adjoint method we have been able to constrain a number of parameters that can help improve the efficiency of models.

While considering how best to conserve storage and runtime we have seen that all our choices for time step method had no noticeable effect on the converge rate. This allows us to view the three choices in mechanism equally without fear of compromising our solution.

There is no noticeable best choice for storage savings, as all mechanisms require the same storage requirements outside of the first iteration where forcing the time step works best. While at higher resolution calculations this difference would grow, considering this trade off with the potential caveats of this mechanisms runtime, it is not obvious that the forced time step is superior.

We also note that there is an anomalous value from the free time step calculation at iteration seven in the 10 Myr. This corresponds to when the calculation was terminated prematurely, and so had to be restarted, which caused a duplication of some output files. This value is therefore not indicative of any greater issue with the free time step.

For the runtime required for each of our six test cases we see the only real difference between the three types of time step control; the upwards method shows to be on average quicker than both forced and free methods for both calculation lengths. As previously mentioned, the region where the runtimes of the forced calculation are noticeably longer due to the nature of forcing the time step, helps us to discredit this as a possible choice. Given that over a short time interval, low resolution calculation this resulted in nearly a $\times 2$ slow down of calculation, the magnified affect of this in more complex calculations would be very disadvantageous.

Therefore from our three options conclude that the upwards time step is the best of the mechanisms tested. We can see that choosing the freely evolving time step as in a standard TERRA calculation has no noticeably benefits over the upwards mechanism in terms of storage, runtime or convergence of our forward-adjoint. While before hand one might have made an argument that due to the iterative nature of the forward-adjoint method we can force the time step to save time and space, we see that in actuality only small gains are made in terms of storage ($\mathcal{O}$ $\sim$25 GB); although at the next increment of resolution we would extrapolate this to correspond to a 250 GB saving at the first iteration. The upwards time step meanwhile does not compromise on convergences, is no worse or better than the other methods in terms of storage, and consistently shows the best runtimes of the methods tested.

For our choice in δ we have observed that the more sophisticated choices used in some studies that looked at forward-adjoint models (Liu et al. 2008; Ismail-Zadeh et al. 2004), while achieving a monotonically decreasing residual, do not achieve the best convergence of residuals in our tests. The simple fixed value < 1 as used in Bunge et al. (2003) shows excellent convergence at both t_0 and t_1 for both length calculations. We do however note that there is some oscillation for these fixed values which does not occur when using the simple function $1 - 0.02n$. The strictly monotonically decreasing nature of the non-linear functions is an undoubtably attractive feature in a numerical model, and as computational power increases these methods would be preferential. Due to the computational limits imposed at present, we believe a choice of $\delta = 0.8$ or $\delta = 1 - 0.02n$ can be considered the preferred factor to use for updating our initial condition temperature field.

The varying length time interval forward-adjoint models provide excellent insight into the limits of the method. We conclude that for models extending up to at least 40 Myr we can expect excellent convergence at t_1 and the features present at t_0 can be taken as accurate. For models between 80 Myr and 120 Myr while we would expect to see a converging present day residual we do not observe a similar convergence at t_0 and in fact observe some defined features which are not present in our reference model. Models longer that 120 Myr require many more forward-adjoint iterations to introduce meaningful mantle structures, with our snapshots showing minimal downwelling features compared to upwellings, with predominantly broad scale deep mantle features being the main reconstructed features.

However, the difference between converging residuals at t_1 compared to at t_0 leads us to conclude that results from longer spanning models must be taken with caution as even here in our relatively simple synthetic tests discrepancies exist across the whole volume. We again recall that in Bunge et al. (2003), their 100 Myr forward-adjoint models presented showed an excellent match to the true state after running for 100 iterations. While we cannot discount that a factor of five increase in iterations here could yield similar results, the practicality of solving this many iterations makes solving 100 iterations unrealistic. Furthermore, there is of course less certainty in the 'true' state we are comparing to at 200 Ma to 120 Ma and so this raises the question of how bad a match these models are.

In spite of this, even if we can only reliably use deep mantle features generated from the adjoint method, this is not without its uses in Earth sciences. Deep Earth mantle structure have been shown to have a large influence on surface dynamics (Lithgow-Bertelloni and Silver 1998) and the long term nature of deep Earth features such as the Large Low Shear Velocity Provinces (LLSVP) has been the focus of recent studies (Zhang et al. 2010; Bower et al. 2013).

We note that a simpler model utilising a 'backwards in time' calculation that only reverses the time dependent terms of the governing equations (eq. (5.1)) and ignores the diffusive term performed calculations back from 75 Ma to 126 Ma before drawing conclusions (Conrad and Gurnis 2003). In their study however, the authors observe that instabilities in the thermal boundary layers make it difficult for this method to accurately reconstruct the present day structures the model began with. Due to this, we conclude that the method used in our study is superior to these methods even if run over shorter time frames due to the lack of instabilities in the boundary layers.

This investigation into adjoints run over different time intervals is more intriguing when considering previous work that looks at error growth in mantle models, which look to determine a 'limit of predictability' (Chapter 3 as well as Bello et al. (2014) and Colli et al. (2015)). Results from these studies suggest at their most conservative estimates, a limit of predictability of 95 Myr (Bello et al. 2014) without an assimilated surface boundary condition. With an assimilated surface it is suggested that solutions will evolve towards a single solution, which corroborates the theorem of Serrin (1959) which states that two incompressible viscous bodies are equivalent given their

boundary conditions are the same. Ismail-Zadeh et al. (2007) meanwhile determine that the adjoint solution is limited by the characteristic thermal diffusion time, which for large features (>100 km) suggests a limit over 300 Myr, and less than 5 Myr for fine features (<10 km). This falls in line with what we have seen here, with the large scale features being predicted for all time scales (given sufficient iterations) and finer features not captured (such as in the upper mantle).

We therefore conclude that despite being within the limit of predictability for this class of models, it is the thermal diffusion time which is limiting our adjoint predictions.

5.5 Conclusion

We have investigated a number of parameters that can be varied in the full forward-adjoint system for mantle convection. A minimum number of modelling assumptions have been made in our investigation here and so our results are relatively straightforward to interpret. In order to optimise the runtime and storage requirements of the forward-adjoint calculation one should consider using a gentle forcing of the time step mechanism, as doing so sees moderate improvements in terms of calculation speed whilst not compromising on the misfit convergences. Furthermore whilst complex non-linear choices can be made for the choice of δ, the factor that controls the amplitude of the adjoint solution used to update the initial condition, simple linear functions can achieve a minimum residual value in far fewer iterations. Despite this effect diminishing over longer timescales, the linear functions still perform best and so we consider these the optimum choice for our forward-adjoint models moving forward. In this work we shall remain with the choice of $\delta = 0.8$.

Results from investigating varying the time interval that the forward-adjoint calculations are run over suggest that drawing conclusions of fine features should be done with caution for longer calculations, though initial conditions derived in this manner still may present a better educated guess than currently employed in the geodynamics community. The effect using these adjoint derived initial conditions have on the final output compared to current methods when conducting whole Earth investigations using mantle models is an open question that could readily be investigated further. As an

example, the effects on dynamic topography over recent Earth history is one avenue of investigation that could benefit from these adjoint derived initial conditions.

With these results, together with those of Horbach et al. (2014), Vynnytska and Bunge (2014), and Ghelichkhan and Bunge (2016) which also investigate some of the parameters involved in running adjoint models, future adjoint model based investigations can be focused on applying the method to real world scenarios using the wealth of present day information available. With this in mind, we turn our attention to using the forward-adjoint method together with a true data source based on Earth observations. In the next chapter we shall attempt to better understand how the introduction of a more complex data source may affect solutions.

CHAPTER 6

INVESTIGATING THE EFFECTS OF TOMOGRAPHIC FILTERING IN ADJOINT MANTLE MODELS

Abstract

Due to the time dependent nature of mantle flow, together with the non-linear equations that govern mantle convection, reconstruction of past mantle flow is non-trivial. The adjoint method has been shown to be a powerful inverse method of determining past mantle flow on Earth. Through running the adjoint together with forward models in an iterative process, information from present day observations can be incorporated into the inverse model to give a more comprehensive understanding of past mantle structure. In this study we build on previous work that looks at the viability and constraints of running adjoint models and attempt to better understand how best to incorporate data from seismic tomography. As seismic tomography is spatially less well resolved compared to even very low resolution mantle circulation models, previous forward modelling studies have made use of the resolution filters for tomographic models. These account for the spatial resolution of the tomography models and allow more like for like comparisons to be made. By applying these filters to the forward model as part of our iterative scheme before comparing to the corresponding tomography model, we find that this does not result in a converging solution. Instead we find that no extra steps need to be applied to the forward model before comparing to tomographic sources. This allows the forward-adjoint method to be used with any tomography model, not just those with available filters.

6.1 Introduction

The adjoint method has been shown to be an excellent process to help address the time dependent nature of mantle dynamics (Chapter 5, Bunge et al. (2003), Horbach et al. (2014), and Vynnytska and Bunge (2014)). Forward-adjoint models work by comparing a mantle circulation model (MCM) end member temperature field to a known true data source, and using any differences between these to improve the initial condition in an iterative process.

So far in this work we have only considered synthetic tests of the method that use plate reconstructions to create the 'true' data source. While these are useful to investigate the accuracy of the method, their larger applications to Earth problems is limited. Considering this we therefore look to employ present day observations of mantle structure as the true data source.

Seismic imaging of Earth's interior reveals a wealth of information on structures in the mantle including two distinct types of seismic features. The first are a series of positive seismic anomalies, which correspond to structures that are colder than average (Grand et al. 1997; van der Hilst et al. 1997), which have been shown to be relics from previously subducted slabs (Bunge et al. 1998; Bunge and Davies 2001).

The second obvious feature in shear wave tomographic models is the presence of two, distinct negative seismic anomalies present in the deep mantle (Garnero and McNamara 2008). These two Large Low Shear Velocity Provinces (LLSVPs) occupy separate hemispheres (Becker and Boschi 2002; Simmons et al. 2010; Ritsema et al. 2011; Koelemeijer et al. 2016) beneath Africa and the Pacific respectively (an example is shown of the -0.6% dV_s velocity perturbation in fig. 6.1a), covering approximately 30% of the core-mantle boundary, with their structure being imaged rising over 1000 km above the core-mantle boundary (Tanaka et al. 2009; French and Romanowicz 2015) (as shown in figs. 6.1b and 6.1c).

However, despite these many studies and more providing detailed analysis of features seen in tomographic models, and how these relate to thermal or chemical features within the mantle, this information is of limited use when trying to construct a picture of the mantle in Earth's history. Due to the non-linear, time dependent nature of the equations that govern mantle convection (Mckenzie et al. 1974; Jarvis and Mckenzie 1980), it is non-trivial to project present day information back in time. Conrad and Gurnis (2003)

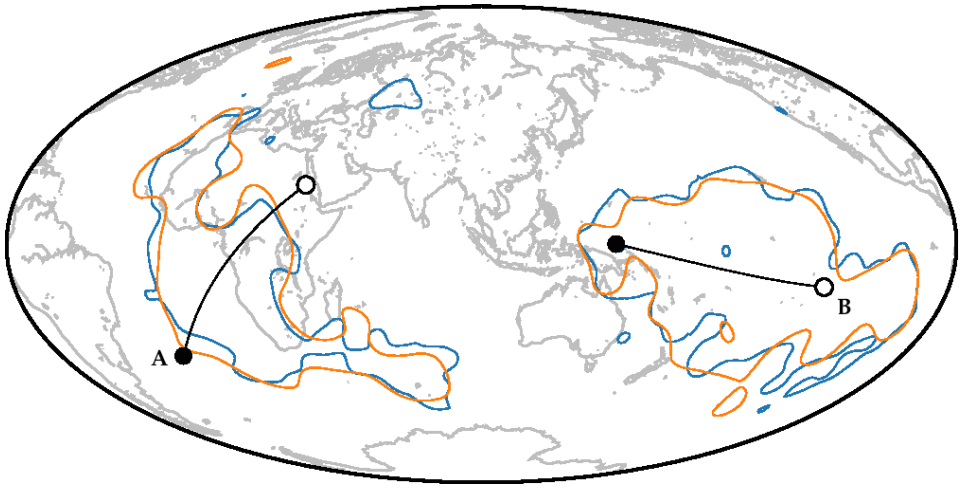

(a) Contours at 2800 km

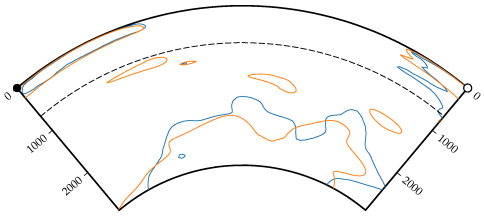

(b) Cross section (A) through African LLSVP

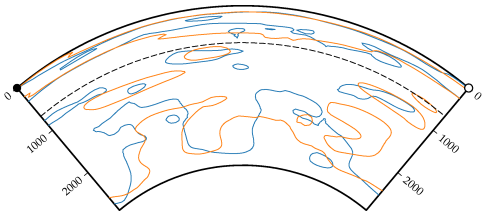

(c) Cross section (B) through the Pacific LLSVP

Fig. 6.1 Seismic tomography data for the LLSVPs. The -0.6% dV_s contours are shown for the S40RTS (blue), S20RTS (orange) tomography models. Coastlines (grey) are included for reference, the dashed black line denotes the 660 km depth boundary.

attempted such a feat by reversing the time dependency of their mantle convection model, and removing the term that governs thermal diffusion, as the diffusive term is unstable when run backwards. While the authors managed to draw some conclusions of dynamic topography in the Cenozoic, their models were also plagued by thermal instabilities from the models boundary layers.

The adjoint method in comparison is a more systematic method of assimilating present day information to reconstruct the unknown past mantle (Bunge et al. 2003; Ismail-Zadeh et al. 2004; Liu and Gurnis 2008). These class of models assimilate present day information by calculating the mismatch between a modelled mantle and an observed mantle before solving a new set of equations that can be thought of as a complimentary, inverse set to the standard forward equations. Some studies have attempted to use present day knowledge to build a picture of the past mantle on a specific region using

adjoint 'lite' models (Spasojevic et al. 2009; Liu et al. 2008; Shephard et al. 2010). These models only consider an adjoint energy in their formulation, as opposed to the full set that include adjoint mass, momentum and energy equations such as in Horbach et al. (2014).

The final class of models that attempt the problem of predicting past mantle information from present day knowledge utilise what is known as a quasi-reversibility method (QRV) (Ismail-Zadeh et al. 2007; Glišović and Forte 2014).

Each of these studies incorporates their chosen tomographic model as their present day mantle structures without accounting for the spatial resolution of the models (Ritsema et al. 2007). As tomographic models are dependent on the data from which they are derived they contain bias to their spatial resolution due to the location of receiver stations (Bunge and Davies 2001); the parameterisation for the tomography model; and the damping and smoothing effects of the tomographic inversion (Ritsema et al. 2007).

Ritsema et al. (2007) and Schuberth et al. (2009a) applied the resolution filter to a variety of end member mantles derived from forward mantle models and note that in doing so creates a change in the geographical pattern of features in the modelled velocity fields, as well as a reduction in the power of the features. These studies along with others (Mégnin et al. 1997; Bull et al. 2009) show how a straight comparison of geodynamic models of Earth to observations can yield unclear, and misleading results. Figure 6.2 shows an example of an end member from a MCM temperature field, together with its shear wave velocity structure both before and after applying a resolution filter. The change in shape and power of features is apparent comparing the two MCM velocity fields to the tomographic model. We see for instance that while the velocity field derived from our temperature field contains a number of positive seismic anomalies not present in the tomographic model, the filtered velocity field contains a number of these features more in line with the tomography.

With the knowledge that comparisons between modelled temperature fields and tomographically derived fields can lead to misleading conclusions we pose the question; should the mismatch calculation of the forward-adjoint method include the resolution matrix of tomography models before calculating said mismatch? In this study we aim to answer this question by applying the forward-adjoint method to a shear wave velocity tomography model that has an associated resolution matrix available. We will do this by investigat-

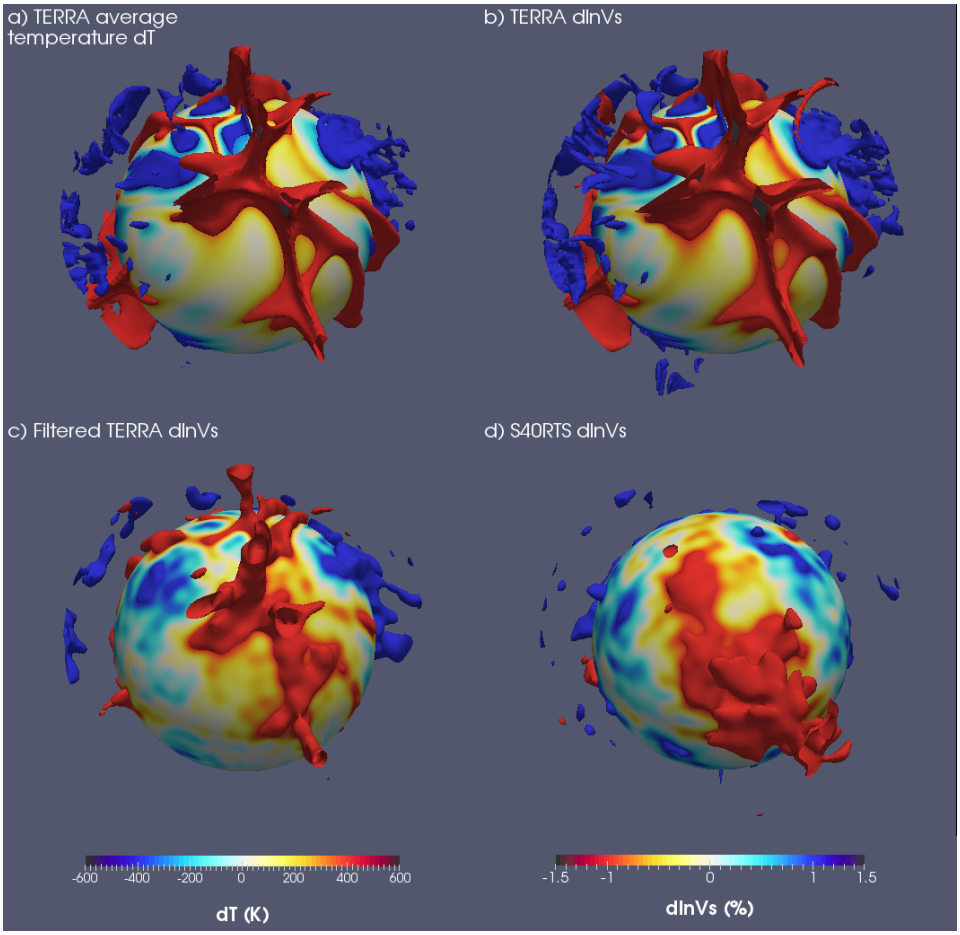

Fig. 6.2 View of (a) TERRA average temperatures, (b) converted shear wave velocity perturbations, (c) converted shear wave velocity perturbations after applying the corresponding resolution filter, (d) S40RTS velocity perturbations focused on the Atlantic seismic anomaly. Images include a radial surface located at 2800 km with $\pm$400 K isosurface for temperature and $\pm$1 % isosurface for seismic velocities. The differences between before (b) and after (c) applying the resolution filter for S40RTS are clear, with (c) showing features more reflective of S40RTS (d).

ing a variety of different methods of comparing the MCM derived fields to the observed tomographic fields.

6.2 Method

6.2.1 Numerical methodology

Forward-adjoint mantle circulation models are carried out using the three-dimensional finite element code TERRA (Baumgardner 1985; Bunge et al. 1997), which has been adapted to perform the forward-adjoint calculation. TERRA solves the following equations, which govern conservation of mass, momentum and energy (Mckenzie et al. 1974) (eq. (6.1)) for an incompressible fluid

$$\nabla \cdot \boldsymbol{u} = 0 \tag{6.1a}$$

$$\nabla \cdot \left\{ \eta (\nabla \boldsymbol{u} + (\nabla \boldsymbol{u})^T) \right\} - \nabla P + \alpha \rho (T_{av} - T) \boldsymbol{g} = 0 \tag{6.1b}$$

$$\frac{\partial T}{\partial t} + \boldsymbol{u} \cdot \nabla T - \kappa \nabla^2 T - H = 0 \tag{6.1c}$$

together with the analogous adjoint equations for mass, momentum and energy (Bunge et al. 2003) (eq. (6.2)) for an incompressible fluid

$$\nabla \cdot \boldsymbol{\phi} = 0 \tag{6.2a}$$

$$\nabla \cdot \left(\eta \{ \nabla \boldsymbol{\phi} + (\nabla \boldsymbol{\phi})^T \} \right) - \nabla \psi + \tau \nabla T = 0 \tag{6.2b}$$

$$\frac{\partial \tau}{\partial t} + \boldsymbol{u} \cdot \nabla \tau + \kappa \nabla^2 \tau + \alpha \rho \boldsymbol{g} \cdot \boldsymbol{\phi} = \partial_T \chi(T). \tag{6.2c}$$

For these equations η is the dynamic viscosity, α is the coefficient of thermal expansion, ρ the reference density, T_{av} the radial temperature profile, $\boldsymbol{g}$ gravitational acceleration, κ is the thermal diffusivity and H is radiogenic heat production. $\partial_T \chi(T) = (T_{\mathrm{t}} - T_{\mathrm{m}}) \delta(t - t_1)$ is the gradient of the misfit function χ that relates the model temperature T_{m} to the observed true temperature T_{t}. $\boldsymbol{\phi}$, ψ and τ can be viewed as the adjoint compliments to the forward $\boldsymbol{u}$, P and T.

These two sets of equations (eqs. (6.1) and (6.2)) are run together in an iterative loop until the misfit at t_1 (present day) falls below a pre determined level, or the total number of iterations is exceeded.

When discussing temperature and velocity variables in the forward-adjoint calculation we utilise the following notation. For a variable, $\cdot_m^n$, superscripts denote the iteration number of the forward-adjoint calculation with $n \in \mathbb{N}_1$; subscripts meanwhile denote the initial $m = 0$ or final $m = 1$ point in time of the model relative to the forward calculation. That is to say $m = 0$ refers to some point in the past from present day, regardless of whether discussing forward or adjoint variables.

For our investigation we use the shear wave seismic tomography models S20RTS (Ritsema et al. 2004) and S40RTS (Ritsema et al. 2011) as our true data source T_t. We have chosen these models as the resolution matrix $\mathcal{R}$ that accounts for the regional variation in coverage of the seismic observations present in the tomography models, are readily available for these models (Ritsema et al. 2007). With $\mathcal{R}$, we can apply a filter to our forward model observations to provide a better comparison to the corresponding tomography model (Schuberth et al. 2009a). A caveat of this is that the two tomography models we are using only display features up to a spherical harmonic degree of 20 and 40 which corresponds to a lateral resolution $\geq$1000 km or $\geq$500 km respectively. This differs greatly from the average lateral resolution of 50 km for the mantle circulation models used here. Because of this resolution difference, we shall investigate the effect comparing two data sources of different resolution has on the efficiency of the adjoint method by adjusting how the present day mismatch is calculated.

In order to convolve our modelled mantle structures with the resolution matrix $\mathcal{R}$ we must convert the temperature field at the end of the forward calculation T_1^n to shear wave seismic velocities. The conversion from $T \mapsto V_s$ can be performed using using lookup tables derived from mineral physics, as such conversions have been shown to allow a more direct comparison to tomographic models (Schuberth et al. 2009b). Using the (T, P) fields from t_1 of the forward model we can therefore calculate seismic velocities V_s, using the lookup tables of Stixrude and Lithgow-Bertelloni (2011). As these models are isochemical we assume a pyrolitic composition for this conversion. This velocity field can then be convolved with $\mathcal{R}$ to achieve a velocity profile that has amplitudes comparable to that of the tomographic data source.

With V_s data for both the model and true source we also need to consider how to convert the seismic velocities to the temperature fields, T_m and T_t, as this is what is used in the adjoint calculation. To obtain a temperature field from the velocity field is non trivial as the mapping $T \mapsto V_s$ is non-unique,

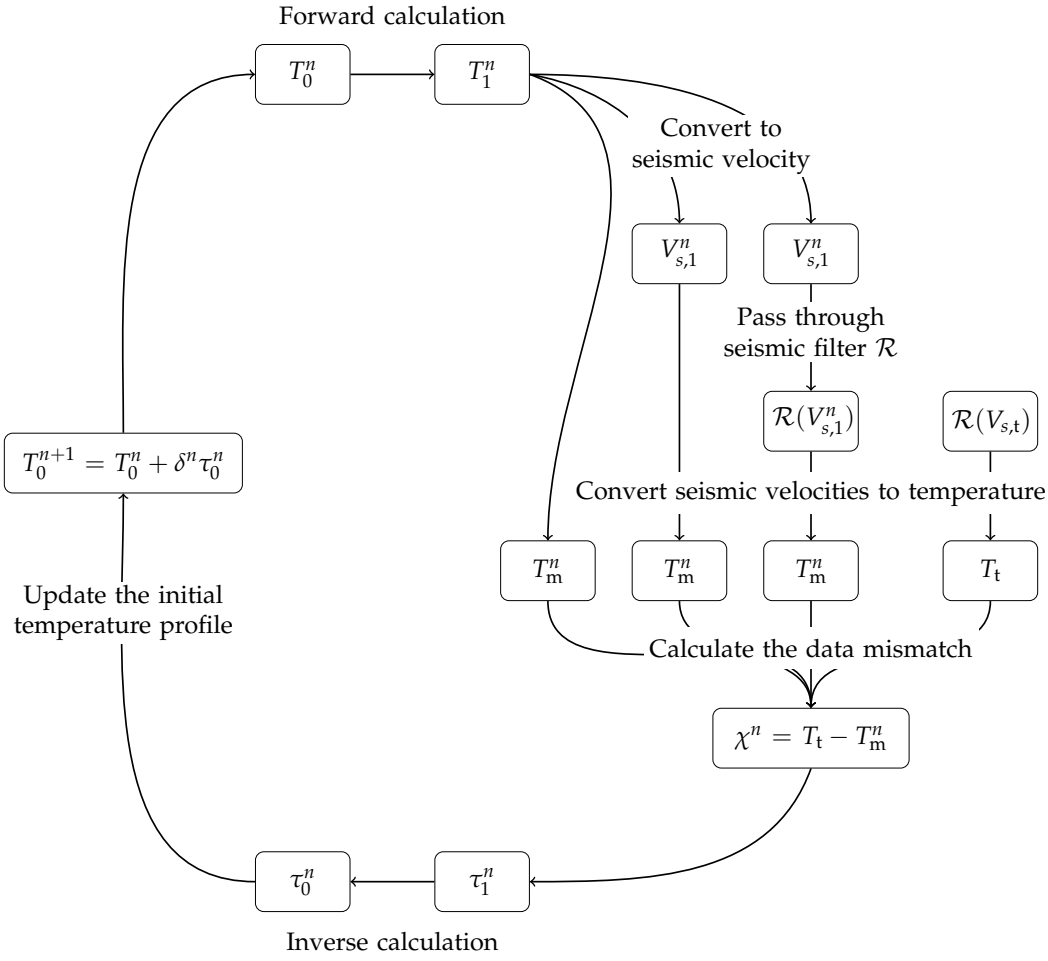

Fig. 6.3 The forward-adjoint workflow, with the different paths to determining T_m used in this study denoted.

so there is no unique inverse mapping. Therefore, for the reverse conversion we simplify the problem and utilise a radial conversion using the equation

$$T = T_{ref} - \frac{1}{\alpha} R \left(\frac{\delta V_s}{V_s} \right), \tag{6.3}$$

where T_{ref} is the average temperature for a given layer from the forward model, α is the coefficient of thermal expansion, R can vary with depth (as has been done in other studies (Bull et al. 2010)) though we take this as a fixed value of 0.5 based on previous results (see section 2.5.1), and $\delta V_s / V_s$ is the horizontal shear velocity perturbation at each point.

As previously discussed the tomographic models differ in resolution to the convection model, and so as well as using the resolution matrix as part of the workflow to determine T_m, we will also conduct calculations that do

not utilise this. Finally as the conversion $V_s \mapsto T$ is an imperfect mapping, we consider a third case that does not perform the mapping to V_s on the way to determining T_m.

We therefore shall conduct three calculations that consider paths for determining the model data source T_m^n used in the mismatch, with the different paths outlined in fig. 6.3. For the first we use the T_1^n temperature profile such that $T_1^n \mapsto T_\mathrm{m}^n$, hereafter referred as TT. The second path we use involves converting the final temperature to shear wave velocities and then using the conversion of eq. (6.3) back to a temperature field, $T_1^n \mapsto V_{s,1}^n \mapsto T_\mathrm{m}^n$, TVT. The final path we consider also takes account of the resolution filtering of $\mathcal{R}$ such that $T_1^n \mapsto V_{s,1}^n \mapsto \mathcal{R}(V_{s,1}^n) \mapsto T_\mathrm{m}^n$, which we abbreviate as TVRT. For all these paths, to determine the true data source T_t we take the shear wave velocities from the tomographic model, which in essence have the resolution filter applied as they are direct observations, and convert these to a temperature field such that $\mathcal{R}(V_{s,\mathrm{t}}) \mapsto T_\mathrm{t}$.

Figures showing the temperature derived structure for S40RTS are shown in fig. 6.4. The upper mantle is characterised by strong colder than average temperature broadly beneath the continents. Just above the core-mantle boundary we see the two large thermal anomalies that are associated with LLSVP structures identified in various tomography studies (Lekic et al. 2012). It is an open question as to whether these are purely thermal or thermochemical in nature (Tackley 1998; Karato and Karki 2001; Davies et al. 2012; Tackley 2012), though as previously stated, for this study we assume an isochemical mantle.

We shall utilise both the S20RTS and S40RTS models for our true data source together with their corresponding resolution matrix for all these given scenarios to give a total of six different cases.

In order to monitor the difference between our modelled and true data sources we calculate the L^2 norm of the mismatch. This gives us a measure of the distance between the modelled T_m, and true T_t, temperature fields, with lower values reflecting a smaller distance between the two fields.

6.2.2 Model setup

All cases are modelled as an incompressible fluid on a mesh with 10 million finite elements; this corresponds to an average grid spacing of 50 km. The viscosity employed in our models varies as a function of depth (r) only

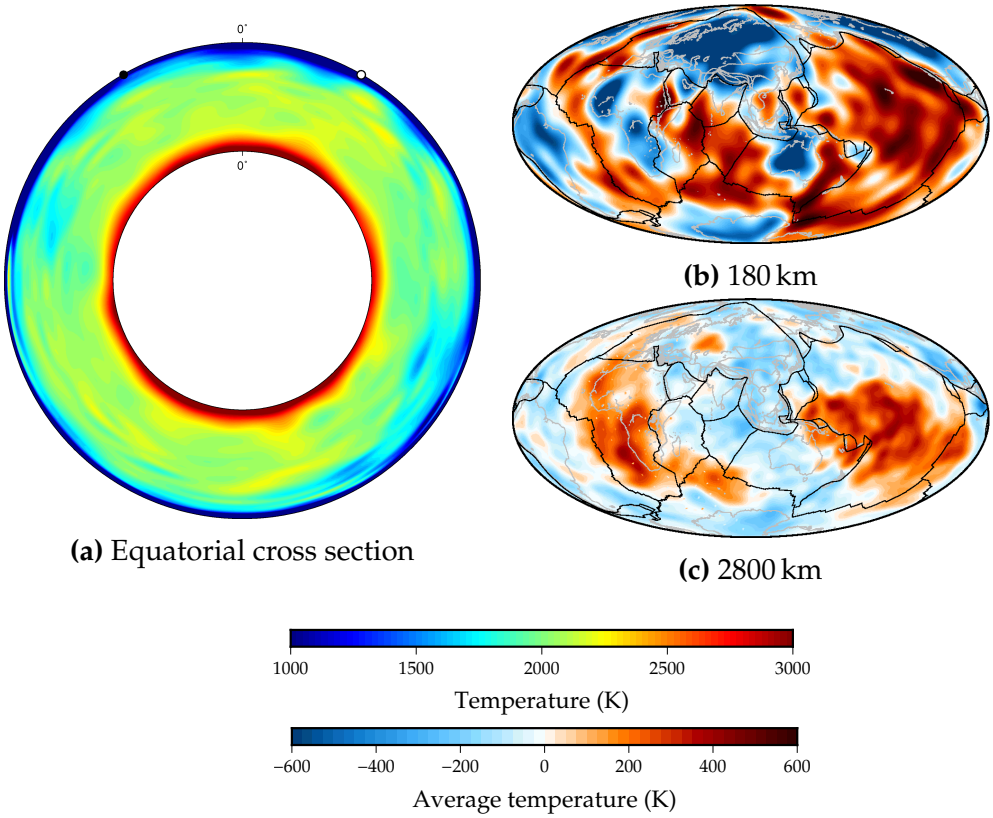

(a) Equatorial cross section

(b) 180 km

(c) 2800 km

Fig. 6.4 Absolute temperature equatorial cross section through the mantle, and the average temperature layers at 180 km and 2800 km for the thermal structure derived from S40RTS. Present day plate boundaries (black) and coastlines (grey).

according to the function

$$\eta(r) = \begin{cases} 100\eta_0 & r \leq 100\,\text{km} \\ \eta_0 & 100\,\text{km} < r \leq 660\,\text{km} \\ 30\eta_0 & r > 660\,\text{km}. \end{cases}$$

The other other key model parameters are detailed in table 6.1.

For the boundary conditions for the forward models we apply a free slip boundary condition at the CMB, while surface velocities are prescribed for the forward calculation using the plate motion reconstruction of Seton et al. (2012), with velocities scaled to match the convective vigour of the underlying convection model. Models are run over a time interval of 10 Myr. This choice is based on previous results (Chapter 5), which have shown that

Parameter		Value	Units
Surface temperature	T_S	300	K
CMB temperature	T_C	3000	K
Internal heating rate	H	4×10^{-12}	$\mathrm{W\,kg^{-1}}$
Reference viscosity	η_0	3×10^{22}	Pa s
Density	ρ	4500	$\mathrm{kg\,m^{-3}}$
Thermal expansivity	α	2.5×10^{-5}	$\mathrm{K^{-1}}$
Thermal conductivity	k	4	$\mathrm{W\,m^{-1}\,K^{-1}}$
Thermal diffusivity	κ	1×10^{-6}	$\mathrm{m^2\,s^{-1}}$
Specific heat capacity	C_V	1000	$\mathrm{J\,kg^{-1}\,K^{-1}}$
Basally heated Rayleigh number	Ra_b	$\approx 5 \times 10^6$	–
Internally heated Rayleigh number	Ra_H	$\approx 9 \times 10^7$	–

Table 6.1 Model parameters

the adjoint method converges quickly yielding excellent results over this timeframe.

The Rayleigh number, the non-dimensional value which quantifies the convective vigour of the system that is basally heated is defined as

$$Ra_b = \frac{\alpha \rho \Delta T D^3 g}{\kappa \eta},$$

where D is the mantle radius and ΔT the total temperature contrast. As our models also contain internal heating we define a second Rayleigh number for an internally heated volume which is defined as

$$Ra_H = \frac{\alpha \rho^2 H D^5 g}{k \kappa \eta}.$$

Using the values used in this study this gives our models Rayleigh numbers $Ra_b \approx 5 \times 10^6$ and $Ra_H \approx 9 \times 10^7$, meaning we expect the vigour of convection in our models to be slightly below what is expected for Earth. Because of this we scale the timescales of our models to allow a similar amount of convection to occur in the models presented here. All times used are after accounting for this scaling.

As the choice of starting initial condition for forward-adjoint calculations have been shown to not affect the convergence of the solution scheme (Horbach et al. 2014), for T_0^1 we prescribe a 1D radial temperature profile.

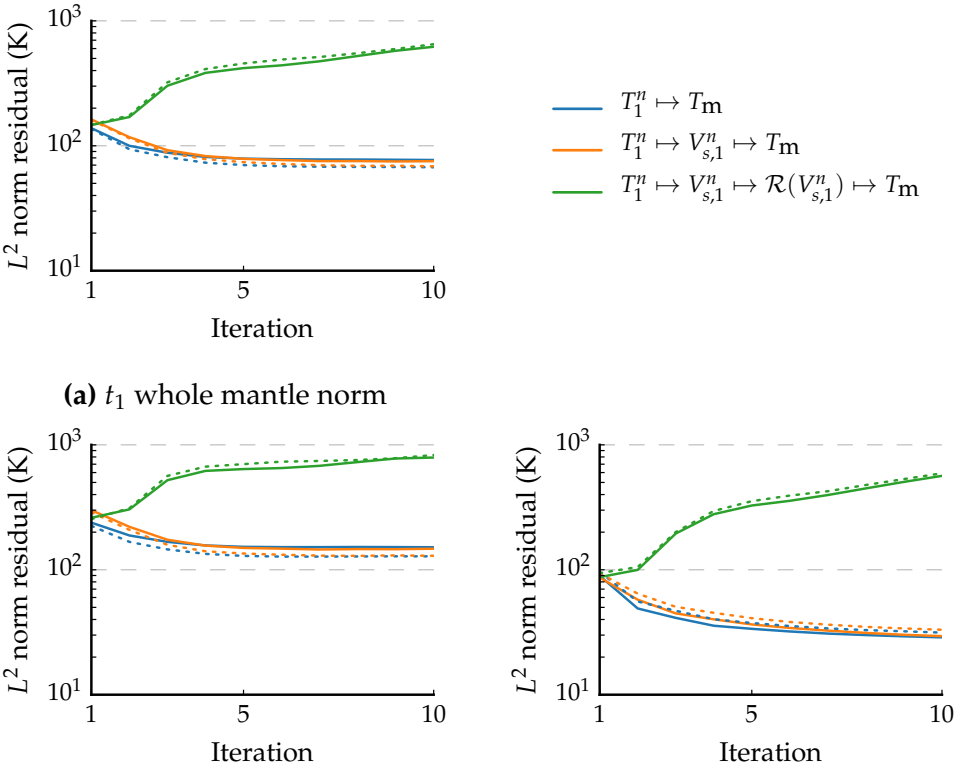

(a) t_1 whole mantle norm

(b) t_1 upper mantle norm

(c) t_1 lower mantle norm

Fig. 6.5 L^2 norms for the residual temperature at t_1 between T_m and T_t for the whole mantle, and broken down into the contributions above (upper mantle) and below (lower mantle) 660 km. Dashed lines denote models using the S40RTS model for T_t, solid lines the S20RTS model. Here it can be seen that cases that do not utilise the resolution matrix show convergence, while also observing that the model mismatch is much lower in the lower mantle compared to the upper mantle.

6.3 Results

The measure of the mismatch between the modelled and true data source is shown for our test cases in fig. 6.5. We see that using either S20RTS or S40RTS has no bearing on the temperature residuals despite the improvements in data coverage of S40RTS. In fact at each iteration, the different T_t sources follow identical courses of convergence, or for TVRT, divergence.

The TT and TVT cases follow a similar rate of convergence however TVRT displays a strictly diverging residual. Looking in more detail between the upper (fig. 6.5b) and the lower (fig. 6.5b) mismatch, the lower mantle residuals are a factor of two smaller than the upper mantle norms. This

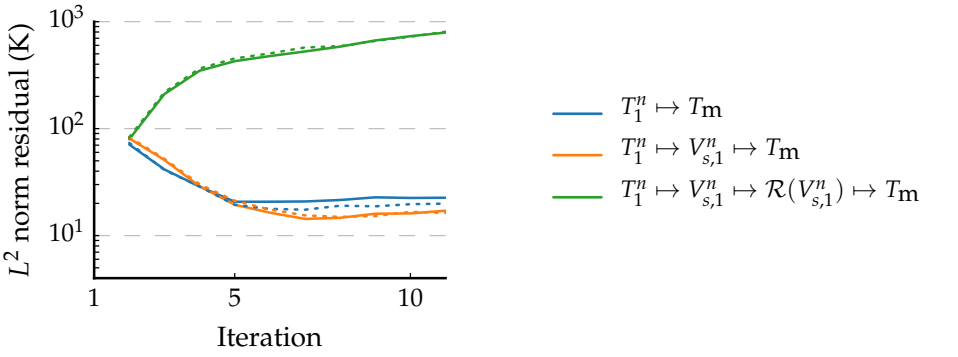

(a) t_0 whole mantle norm

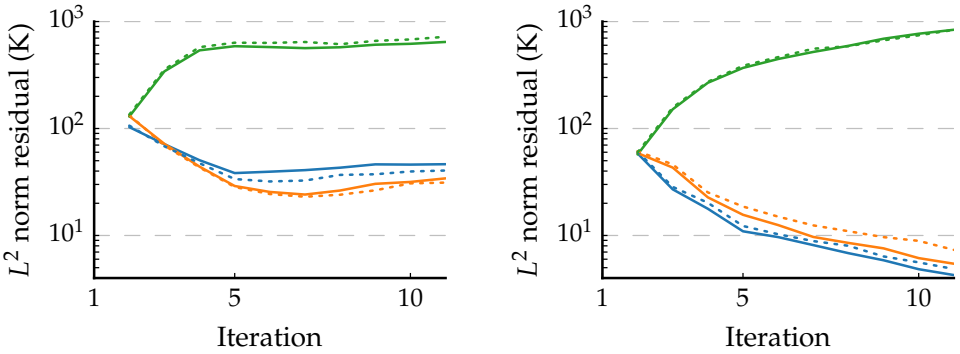

(b) t_0 upper mantle norm

(c) t_0 lower mantle norm

Fig. 6.6 L^2 norms for the residual temperature at t_0 between the current T_0^n, and previous T_0^{n-1} iterations temperature field for the whole, upper and lower mantle. Dashed lines denote models using the S40RTS model for T_t, solid lines the S20RTS model. Beyond the fifth iteration the difference between successive updated initial conditions is ≈ 20 K for cases that show convergence suggesting some small scale oscillations between iterations.

is not unexpected as it is questionable whether high velocity anomalies in the uppermost mantle are purely thermal in nature or compositionally influenced (Forte et al. 1995). It has also been observed in other adjoint studies (Chapter 5 and Horbach et al. (2014)) that the mismatch in the upper mantle is less well constrained by this method, again due to crustal features. In the lower mantle, the lowest mismatch values are within 30 K by the end of the calculation, showing a three fold reduction from the first iteration. We also note that following only one iteration, the mismatch falls by almost half for the converging cases.

Plotted in fig. 6.6 is the difference between the previous and current iterations' initial condition temperature field. The same trends between S20RTS and S40RTS are observed, with the TT and TVT cases showing more

incremental adjustments to the temperature field over successive iterations, whereas TVRT applies greater adjustments at each iteration. These results reflect the t_1 norms, with the lower mantle adjustments for the converging cases reaching values <10 K by the calculations end. In the upper mantle we see adjustments of very similar sizes being applied for all cases beyond the fifth iteration. The slightly smaller adjustment in the upper mantle for the T_0^2 field of the TT case can be explained by the lack of extra complexity of the V_s conversion where the indeterminate influence of crustal features come into effect.

The continually diverging updates in initial condition, together with the diverging present day temperature profiles for the TVRT case suggest that the process of applying the resolution filter is dramatically changing the temperature structure of the system. This is then having a feedback effect due to the iterative process and compounding errors, as we further alter the forward temperature field by applying the resolution filter on each successive iteration.

As minimising the temperature misfit is made more difficult in the upper mantle due to crustal features we shall focus on the lower mantle reconstructions. In figs. 6.7 to 6.9 we present the layer averaged temperature field for the three cases using S40RTS at t_0, t_1, and also the t_1 temperature field prior to any conversion, for successive iterations. Overlaying the -0.6% dV_s contour shows how successive forward-adjoint iterations can quickly match to the true data source.

We see in the first iteration of TT that at a depth of 2800 km, over the 10 Myr assimilation period no real features are introduced with the initial temperature profile still being the dominant feature. By the beginning of the second iteration we see that structures that resemble the contour from the tomographic model at both t_0 and t_1. Successive iterations further reinforce these two structures with the t_0 positive temperature features being rotated slightly eastward from the present day temperature field.

The TVT case presented in fig. 6.8 shows similar behaviour in the early iterations with the effect of converting to V_s and back only serving to reduce anomalous temperature amplitudes that otherwise line up with the contours. At the fifth iteration we see that the process of converting to and from seismic velocities now has quite a pronounced effect, reducing and sharpening the colder than average regions at this depth. While the -0.6% contour still encircles the hottest regions at this depth, a much larger area is

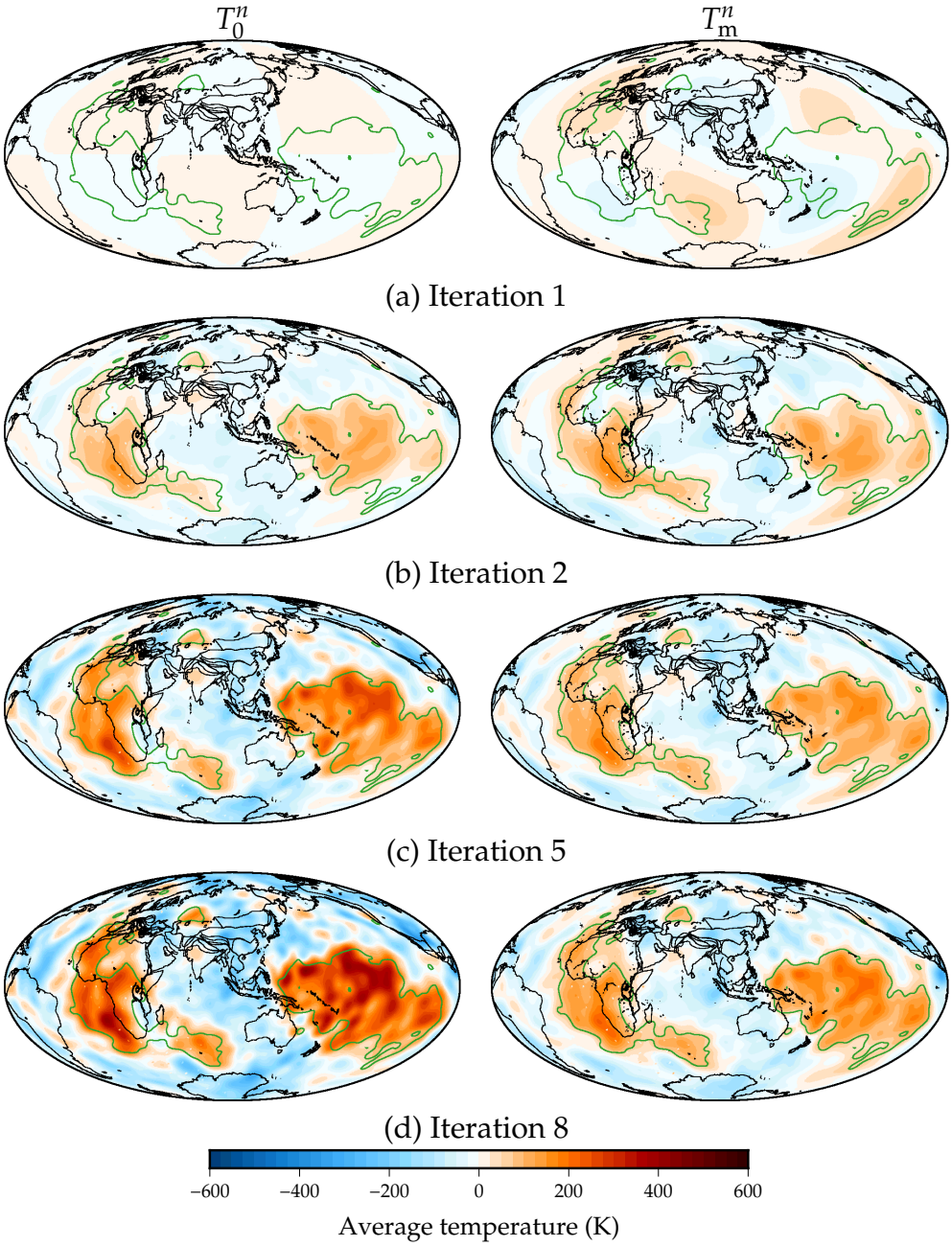

Fig. 6.7 Horizontal average temperature maps at 2800 km of the initial T_0^n, and the final T_m^n, temperatures from the $T_1^n \mapsto T_m^n$ forward-adjoint model using S40RTS for iterations one, two, five and eight. Relevant time period coastlines (black) and the -0.6% dV_s contours are shown for S40RTS (green) are included. Hotter than average regions, which are seen to correspond with the positive V_s anomalies, overlap at both t_0 and match at t_1 reflecting the low misfit norms.

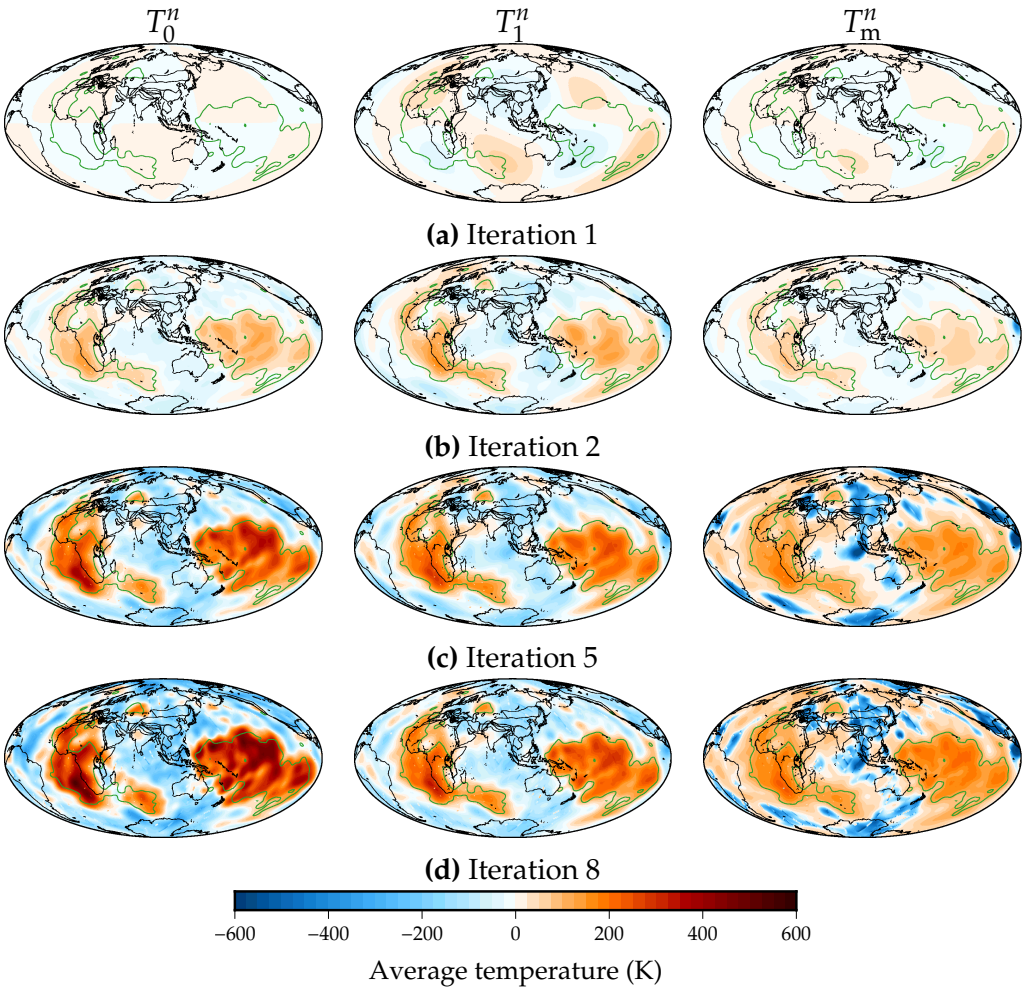

Fig. 6.8 Horizontal average temperature maps at 2800 km of the initial T_0^n, final T_1^n, and model, T_m^n; temperatures from the $T_1^n \mapsto V_{s,1}^n \mapsto T_m^n$ forward-adjoint model using S40RTS for iterations one, two, five and eight. Relevant time period coastlines (black) and the -0.6% dV_s contours are shown for S40RTS (green) are included. The T_1^n temperature field shows excellent match to the -0.6% dV_s contour, however in the process of determining T_m we see that in later iterations the negative temperature anomalies are sharpened and increased in power while hotter regions are expanded.

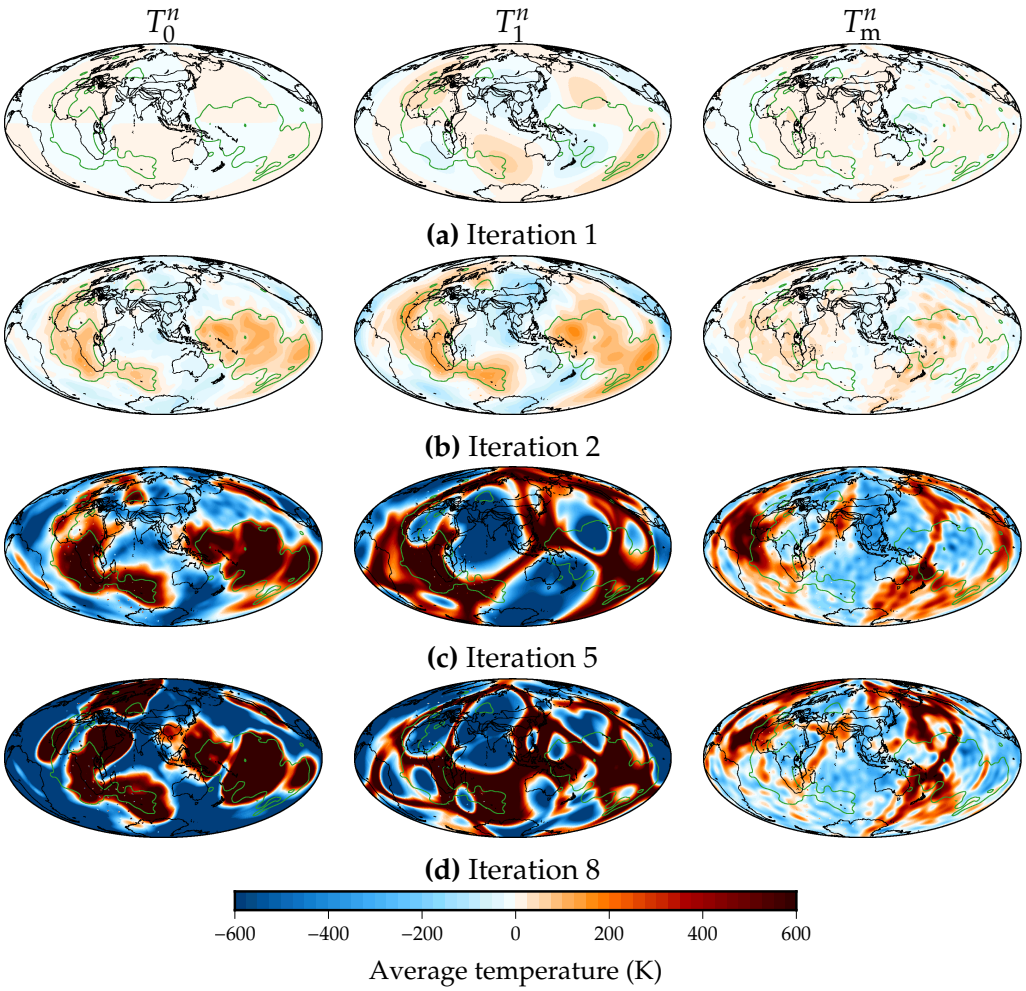

Fig. 6.9 Horizontal average temperature maps at 2800 km of the initial T_0^n, final T_1^n, and model, T_m^n; temperatures from the $T_1^n \mapsto V_{s,1}^n \mapsto \mathcal{R}(V_{s,1}^n) \mapsto T_m^n$ forward-adjoint model using S40RTS for iterations one, two, five and eight. Relevant time period coastlines (black) and the -0.6% dV_s contours are shown for S40RTS (green) are included. By the fifth iteration it can be seen that the effects of the resolution matrix have dramatically altered the temperature field of the model such that there is no overlap of positive temperature anomalies and the -0.6% dV_s contour.

hotter than average when compared to the respective T_1^n prior to the conversions. Despite this quite dramatic shift in T_m we see however the power of the adjoint method, with the predicted t_0 structures consistently returning back to two distinct positive thermal anomalies reaffirming the proposed idea that solutions converge to a single initial condition (Horbach et al. 2014).

Finally looking at the slices from the TVRT case (fig. 6.9), we can see the diverging temperature mismatch field observed in fig. 6.5. We see following the first forward iteration that as expected the resolution filter alters the modelled temperature structure which when combined with our true data source as in the other examples goes on to create an initial temperature field that follows the -0.6% contour. The effect of the resolution filter on the second iteration shifts the structures away from the contour of the true data source, more prominently in the Pacific, whilst also reducing the amplitude of features. By iteration 5 we see the predicted temperature field, whilst a similar shape to the other cases, has strong temperature gradients with temperatures exceeding ± 600 K. Due to these substantial temperature gradients, 10 Myr of assimilating the plate reconstructions in the forward model is an insufficient length of time to overcome this very different temperature field, with the T_1^n field now not resembling the true field as in the other instances. The application of the resolution filter at this point does little to improve the forward model temperature field. The effects of this feedback loop of more extreme present day mismatch values further compounds the issue over successive iterations, as shown by figures from the eighth iteration.

6.4 Discussion

In this study we have built on the previous work testing the forward-adjoint method from Chapter 5, by using a data source derived from Earth studies and investigated different methods of performing the mismatch calculation. Many studies have shown that applying the appropriate resolution filter aids comparisons between geodynamic models and tomography (Ritsema et al. 2007; Bull et al. 2009; Schuberth et al. 2009a; Davies et al. 2012). However, we see in the results presented here that accounting for the filtering as part of the iterative process of calculating the initial condition, distorts and prevents converging solution.

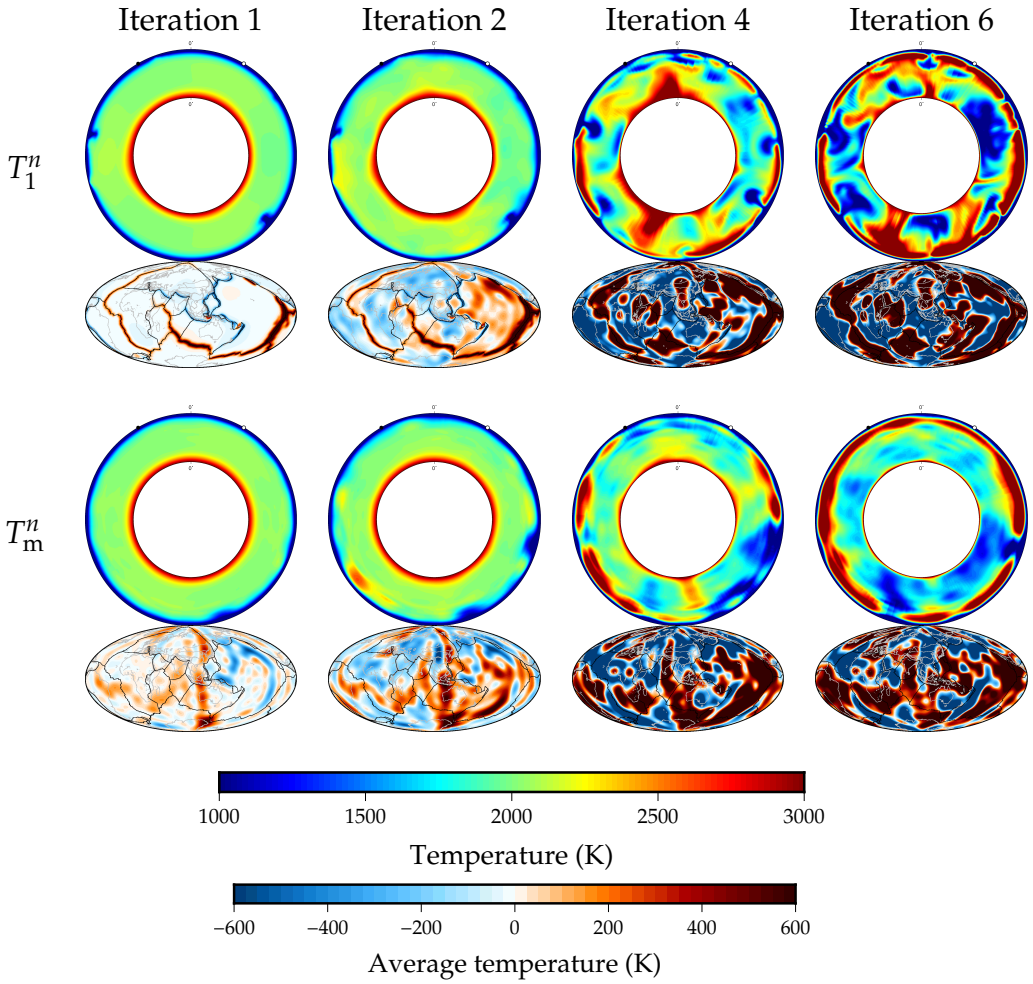

Fig. 6.10 Absolute temperature equatorial cross sections through the mantle, and the average temperature layers at 180 km at t_1 for the TVRT case using S40RTS, showing the temperature structures before and after applying $T_1^n \mapsto V_{s,1}^n \mapsto \mathcal{R}(V_{s,1}^n) \mapsto T_m^n$ in order to determine T_m. Here we see the effect of the resolution filter on the upper mantle over successive forward-adjoint iterations.

Figure 6.10 presents equatorial cross sections, together with the average temperature profile for 180 km depth from the TVRT model using S40RTS resolution filter. We see that in applying the resolution filter the spreading and converging plate margins of the forward model at iteration one are completely removed, with features in the cross section not present prior to the conversion. This introduction of different features is more pronounced in the second iteration with a significant positive thermal anomaly present after filtering. The introduction of such significant thermal anomalies is clearly the reason for the observed diverging solution with this being the only difference from the other cases that were ran. Inspecting the images from the 180 km horizontal plots, we see the effect this has as significant thermal anomalies are present in the later iterations. Here thermal anomalies are seen to line up with the plate margins as should be expected in the early iterations, but in later iterations they have very sharp boundaries with significant temperature gradients beyond what are observed. Looking at the cross sections of the later iterations, unsurprisingly no real match to the expected structures are present.

These models were reran where, for the uppermost 200 km, when performing the conversion to V_s using eq. (6.3) we set $R = 0$ as in other studies to account for the indeterminate nature of velocity perturbations at shallow depth (Bull et al. 2010). This however, yielded no improvements over the results presented here, leading us to conclude that a region at least as deep as the upper mantle would need to be removed in the conversion in order to maintain some convergence in the lower mantle. While this is one potential way of removing the feedback loop we are observing by applying the resolution filter, we do not believe a compromise should be used.

We therefore are left with the TT and TVT cases for using in calculating the mismatch. Owing to the uncertainties in converting to V_s and back again, which involves a crude radial conversion back to temperatures, the preferred method is the TT method.

Having determined that using tomography models that have an associated resolution filter yields no advantages due to erroneous effects of using $\mathcal{R}$, this opens up forward-adjoint methods to use any of wealth of available global seismic tomography models. One such candidate for further studies to utilise would be the SMEAN, PMEAN, and the newer SMEAN2, tomographic models of Becker and Boschi (2002) which each aggregate several

tomography models to average the models and emphasise the common structures of the separate models.

6.5 Conclusion

In this work we have investigated three different ways of manipulating the temperature structure from the forward model to compare to a shear wave seismic tomography model. We have shown that over the short timescale used in this study, using the resolution matrix that corresponds to the tomography model used for the true data source does not provide any advantages of matching spatial resolutions. We conclude that using the forward predicted temperature field as the temperature field used in the mismatch calculation yields a solution with no disadvantages. In future work looking to extend the forward-adjoint method further back in Earth history we would suggest it unnecessary to account for poorer resolutions in the true data source, as the adjoint calculation accurately assimilates the true present day mantle structures.

Following this conclusion we have now determined; a preferred time interval to run our forward-adjoint model over, as well as the ideal method of comparing modelled structures to the seismic data. With this knowledge we will, in the final chapter of this work, turn our attention to applying the forward-adjoint method to high resolution models that closer mimic Earth features to investigate deep mantle structures.

CHAPTER 7

INVESTIGATING THE DIFFERENCES IN 40 Myr MANTLE FLOW FOR DIFFERING VISCOSITY PROFILES USING STANDARD AND INVERSE METHODS

Abstract

Mantle circulation models (MCMs) are started from an unknown initial condition. This lack of knowledge for a starting point introduces uncertainties to the early part of models when looking at mantle flow patterns. Inverse methods have been shown to overcome the uncertainty of the initial condition by assimilating present day observations. We compare the classic method for generating an initial condition for MCMs to using one such inverse method, the adjoint. The classic method uses prior plate reconstructions stages available to precondition the starting point at 40 Ma, whereas the adjoint method uses tomographic data from present day together with the last 40 Myr of plate reconstructions. We observe that irrespective of viscosity structure, adjoint derived initial conditions create markedly different flow patterns over the 40 Myr assimilation period. Comparisons of the modelled present day mantle to tomography yields a varying distribution of velocity perturbations for the different initial conditions.

7.1 Introduction

Observations of the lower mantle from seismic tomography reveals two extremely large anomalous regions at the core-mantle boundary (CMB), which significantly increase the travel times of seismic waves that travel

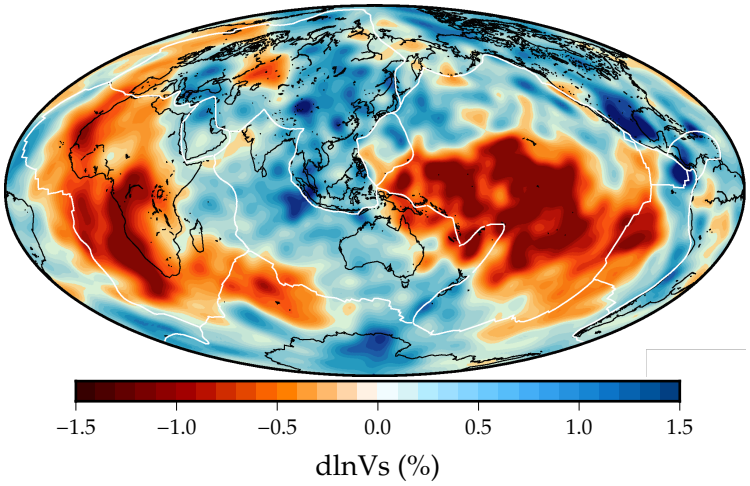

Fig. 7.1 Shear wave velocity perturbations for the S40RTS model at 2800 km depth highlighting the LLSVP anomalies near the CMB. Present day coastlines are highlighted by black lines, present day tectonic boundaries by white lines.

through them (Garnero and McNamara 2008). These two anomalous regions, located beneath the Pacific and Africa respectively (as seen in fig. 7.1), have been observed in S wave tomographies, and to a lesser extent in P wave velocity models (Garnero et al. 2016). Due to their observed existence in S wave tomographic models, these two regions are referred to as the Large Low Shear Velocity Provinces (LLSVPs).

The nature, composition and stability of these LLSVPs has been an ongoing research question that has generated lively debate (Dziewonski et al. 1977; Ritsema 1999; McNamara and Zhong 2005; Zhang et al. 2010; Davies et al. 2012; Bower et al. 2013; Bull et al. 2014). Numerous studies have attempted to reconcile these LLSVPs with our understanding of mantle dynamics through the use of mantle circulation models. Mantle circulation models (MCMs) are a class of mantle convection model that assimilate known plate reconstructions as the surface boundary condition, recreating mantle flow patterns similar to those observed at present day (Bunge et al. 2002).

The stability of these structures as two near antipodal features in the lower mantle is a particularly interesting question, with studies showing that the remnants of subduction, colder higher than average wave speed material, surrounds the LLSVPs (Grand et al. 1997; Bunge et al. 1998; Zhang et al. 2010; Shephard et al. 2012a). Through the use of MCMs and long plate assimilation periods ($>$ 250 Myr) studies have investigated the possibility of the LLSVPs existing more or less as they are prior to the breakup of Pangea

(Zhang et al. 2010; Bower et al. 2013; Bull et al. 2014). Further interest has been in whether the LLSVPs are caused by thermal or thermo-chemical structures (Davies et al. 2015a; Deschamps et al. 2015). A purely thermal explanation for the LLSVPs would be that they are comprised of a collection of fine plumes, which due to resolution limitations in the tomography are imaged as single large features (Schuberth et al. 2009a; Bull et al. 2009) Thermo-chemical explanations meanwhile hypothesise that the LLSVPs are comprised of reservoirs of chemically distinct material that has a density higher than the surrounding mantle (McNamara and Zhong 2005; Bull et al. 2014).

A limitation in these MCM studies however, is the lack of initial condition for past mantle flow. This is an inherent unknown, and inferences from mantle circulation models for the time evolution of mantle flow are intrinsically linked to their starting condition. While studies have shown that differences in initial condition can be overcome through assimilation of known surface boundary velocities (Colli et al. 2015), these differences are reduced over the course of the calculation meaning early calculation mantle flow will still not be well constrained.

Attempts to overcome this lack of initial condition have been made with use of knowledge of the present day mantle flow from sources such as tomography. Through simple inversions, a density structure for tomographic models can be generated and related to a temperature field, which can then be used as an initial condition for a backwards calculation (Conrad and Gurnis 2003). Such backwards in time methods however are not well suited to the problem of mantle convection as they ignore the effects of thermal diffusion in order to maintain some stability. More sophisticated methods that do not ignore diffusion are available such as the adjoint (Bunge et al. 2003; Ismail-Zadeh et al. 2004) and quasi-reversibility (Ismail-Zadeh et al. 2007). The adjoint method is an iterative process of forward and reverse calculations which has been shown to be well suited to mantle models, converging to a global minimum for the unknown initial condition determined by the method (Horbach et al. 2014). However, as each initial condition is unique to its physical parameterisation (e.g. heating mode, rheology, compressibility), this adds further complexity to attempts to constrain past mantle flow due to these additional unknowns.

The few previous studies looking to constrain past mantle flow using adjoint methods have employed a single parameterisation for their inves-

tigations, with each study choosing a different parameterisation. One of the main differences between these models is the choice of viscosity profile. Many radial viscosity profiles have been put forward for the mantle, with a remarkable amount of variation as to where high and low viscosity regions may exist (Hager 1984; Hager and Richards 1989; Mitrovica and Forte 2004; Rudolph et al. 2015; Liu and Zhong 2016). With the mantle also expected to feature lateral variations in viscosity it is not untypical for models to feature viscosity variations over 3 orders of magnitude. Such contrasts in viscosity has a major influence on flow speeds and the convective planform of the mantle (Bunge et al. 1996; Bunge et al. 1997).

As viscosity changes have been shown to have a significant effect on the convective patterns of the mantle, we shall focus our investigation to look at applying the adjoint method to different radial viscosity profiles. Since the adjoint method by design generates a unique initial condition for its given model parameters we can also see how these initial conditions compare to the classic MCM models. By comparing adjoint and classic MCMs we hope to better understand how flow patterns differ between the two methods over the assimilation period while using different viscosity profiles.

7.2 Method

We derive the first initial condition for our forward models using the adjoint equations for incompressible mantle convection (Bunge et al. 2003). These equations are combined with the standard forward equations for incompressible mantle convection (Mckenzie et al. 1974), and are solved in an iterative process as shown in fig. 7.2.

This method assimilates plate reconstructions in the forward model as in typical mantle circulation models (Bunge et al. 2002) which results in a temperature field which shows agreement with observed present day mantle features (Schuberth et al. 2009b). Following the conclusion of the forward model present day observations of the mantle (from sources such as seismic tomography), are assimilated by computing the difference between the final modelled temperature field and the observed temperature field to form an adjoint temperature field. This adjoint temperature field is then used as an initial condition for the adjoint equations, which run from present day to the start of the forward model, at which point we can update our initial

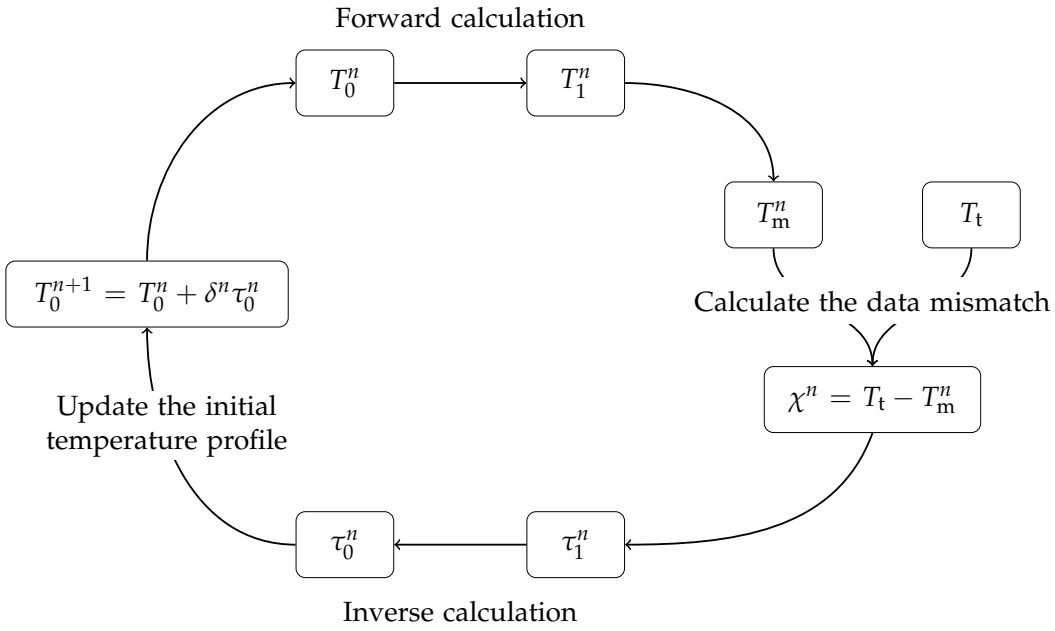

Fig. 7.2 The iterative solution scheme of the forward-adjoint workflow.

condition for the temperature field in Earth's past. Successive iterations allow the initial condition to converge towards a fixed solution for a given physical parameterisation as shown by Horbach et al. (2014). Previous results (see Chapter 5) suggest that the adjoint method performs best for models running over 40 Myr. We will therefore investigate models starting at 40 Ma.

The second initial conditions we use are determined using a classic mantle circulation model that uses 200 Myr of plate reconstructions. These models are initiated from a 1D temperature profile and conditioned with the oldest available stage of plate reconstruction for 50 Myr before being progressed from 200 Ma to 40 Ma. Setup for calculations such as this is typical for mantle circulation studies. By taking the last 40 Myr of mantle structure from this calculation to compare to the adjoint derived models allows observations between the different temperature structures generated during each calculation.

We perform all calculations using an adapted version of the spherical finite element code, TERRA (Baumgardner 1985; Bunge et al. 1997). Calculations are carried out on a computational mesh of 80 million nodal points, which corresponds to an average grid spacing of 22 km. Performing calculations at this resolution allow us to investigate models that have a convective vigour comparable to that of Earth, with an internally heated Rayleigh num-

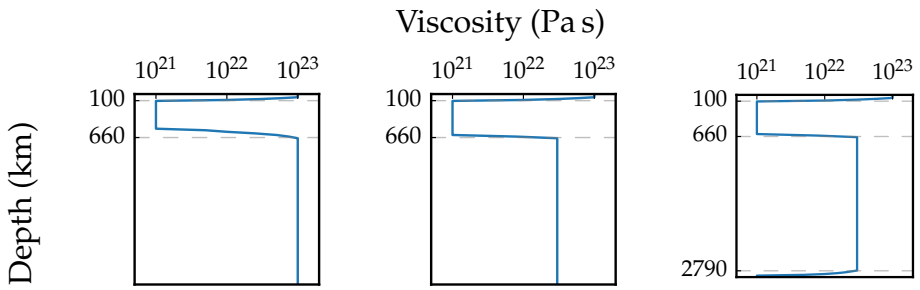

(a) Case 1 **(b)** Case 2 **(c)** Case 3

Fig. 7.3 The three depth dependent viscosities profiles used in this study.

Parameter		Value	Units
Surface temperature	T_S	300	K
CMB temperature	T_C	3000	K
Internal heating rate	H	4×10^{-12}	$\mathrm{W\,kg^{-1}}$
Density	ρ	4500	$\mathrm{kg\,m^{-3}}$
Thermal expansivity	α	2.5×10^{-5}	$\mathrm{K^{-1}}$
Thermal conductivity	k	4	$\mathrm{W\,m^{-1}\,K^{-1}}$
Thermal diffusivity	κ	1×10^{-6}	$\mathrm{m^2\,s^{-1}}$
Specific heat capacity	C_V	1000	$\mathrm{J\,kg^{-1}\,K^{-1}}$

Table 7.1 Model parameters

ber value $Ra_H \approx 4 \times 10^8$. This value of Ra_H is in line with Rayleigh number estimates for Earth's mantle (Davies 1999).

The viscosity profiles employed in our study are shown in fig. 7.3. All models have a high viscosity uppermost mantle (10^{23} Pa s) to replicate the effects of the lithosphere, with an upper mantle viscosity of 10^{21} Pa s. Below 660 km depth we then use three differing viscosity structures with case 1 featuring a factor of 100 viscosity increase into the lower mantle. For case 2 we have a more moderate factor of 30 increase in the lower mantle to a value of 3×10^{22} Pa s. In case 3 we have this same factor increase into the lower mantle, but also include a much less viscous layer from 2790 km to the CMB. Other key physical parameters used in this study are stated in table 7.1.

At the surface we assimilate plate velocities according to the plate reconstruction model of Seton et al. (2012) by setting these as the boundary condition for the velocity field. The core-mantle boundary is prescribed as a free slip boundary condition due to the low viscosity of the adjacent core material.

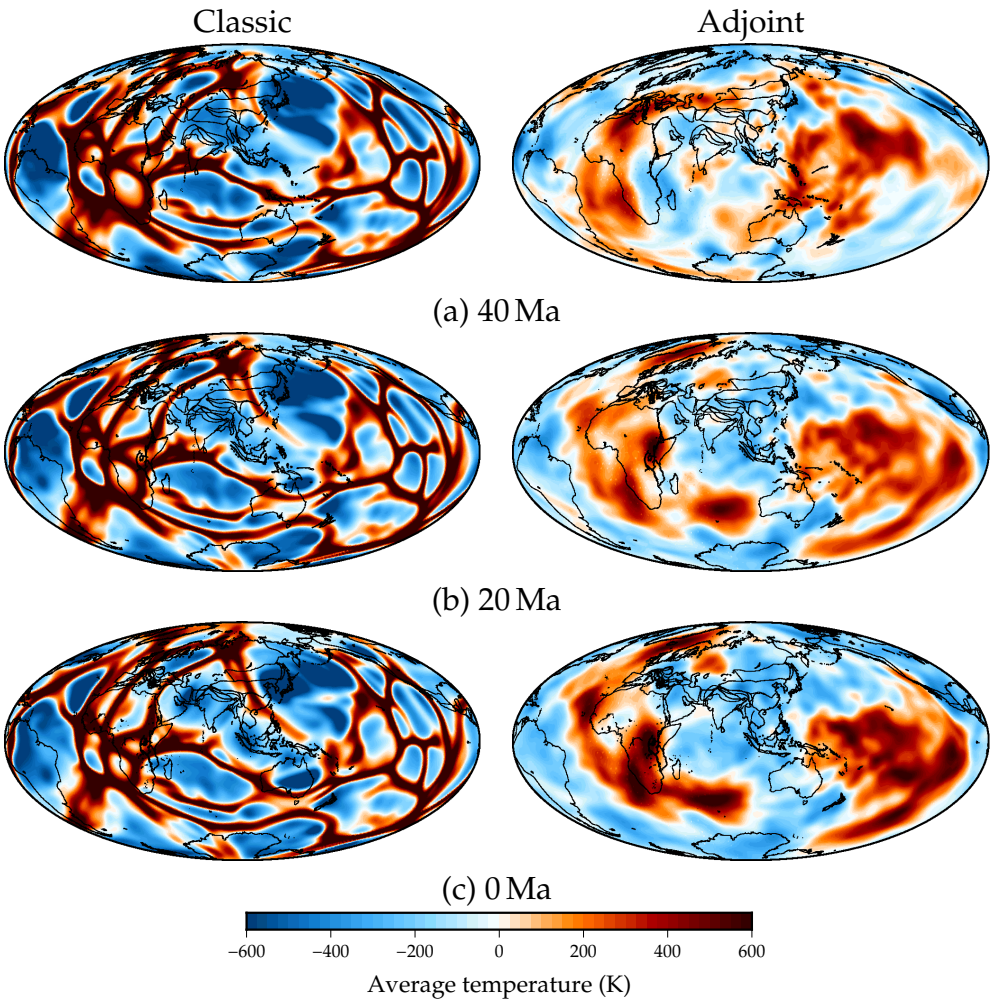

Fig. 7.4 Average temperature plots at 2800 km for different stages for the case 1 viscosity profile for the classic (left), and adjoint derived initial condition (right) mantle circulation models. Black lines denote current age coastlines.

7.3 Results

7.3.1 Time evolution of classic and adjoint based mantle circulation models

In figs. 7.4 to 7.6 we present the average temperature profile at 2800 km depth for the last 40 myr for both the classic MCMs and MCMs started at 40 Ma with the adjoint derived initial condition.

For our most viscous mantle, case 1, we observe that both the classic and adjoint models show hot regions in the Pacific and Africa across all ages, separated by colder than average material. Due to the stiffness of the lower

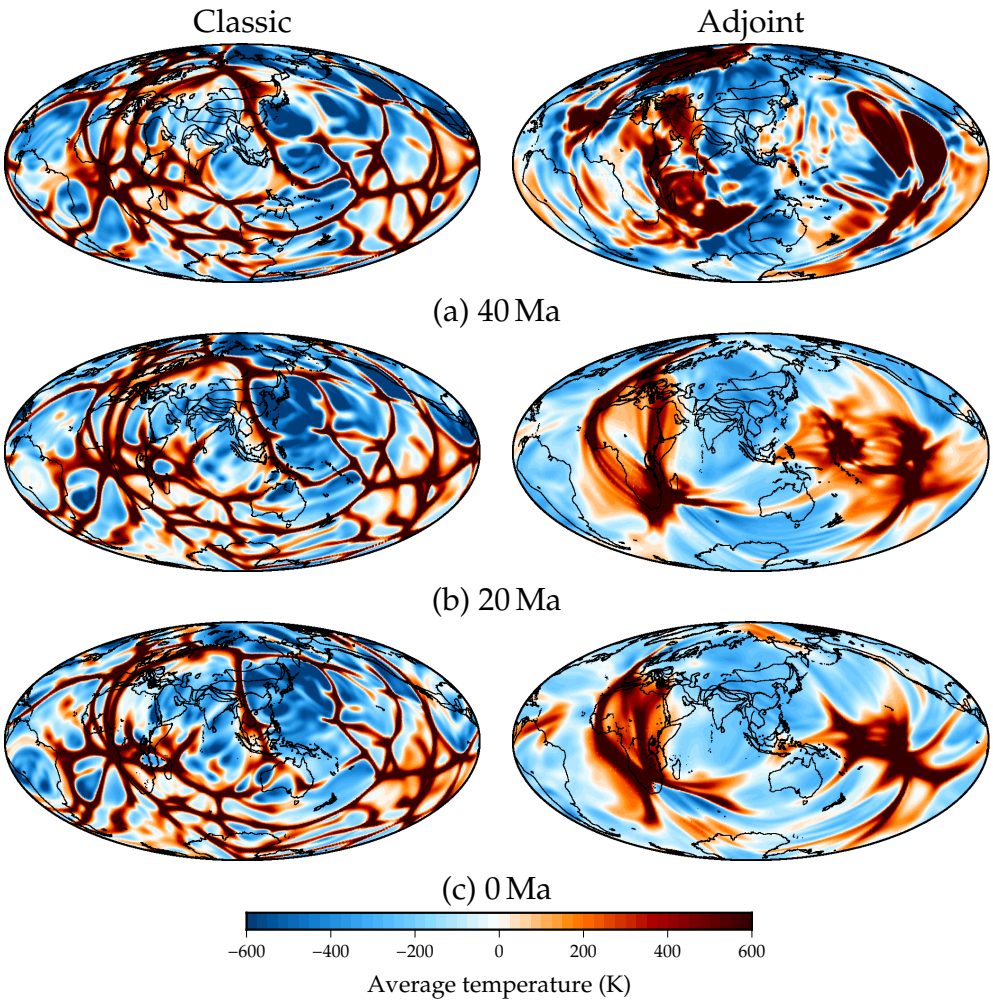

Fig. 7.5 Average temperature plots at 2800 km for different stages for the case 2 viscosity profile for the classic (left), and adjoint derived initial condition (right) mantle circulation models. Black lines denote current age coastlines.

mantle, the hotter than average features do not show much movement over the 40 Myr of circulation calculation. The form that the hotter than average features take varies quite dramatically however. In the classic model we see a fine 'spiderweb' of hot features, typically observed in high Rayleigh number, purely thermal mantle circulation models (Schuberth et al. 2009b). These fine features are the base of fine upwellings plumes that extend up from the CMB. In comparison, the adjoint model shows very broad features that closely resemble the S40RTS tomographic model used in the assimilation process of the adjoint calculation.

Case 2 (fig. 7.5), which features a $\times 30$ increase into the lower mantle displays much more mobile features over the 40 Myr. We again note that the

classic model consists of the fine web of hotter than average features that are still centred around the Pacific and Africa. Over the 40 Myr circulation calculation these two regions grow more distinct with cold material being placed between them.

The adjoint based calculation again begins as two distinct regions. We note that at 40 Ma around the main hot features there is some local banding of hot and cold features, which may suggest some numerical instabilities. By 20 Ma these features have been removed leaving the two very distinct regions, with the African feature displaying the typical south-east to north planform as observed in the tomography, but constructed of much finer features. Similarly the Pacific features planform lies in a similar region to the observed LLSVP region while displaying the more typical fine upwellings. By present day these two regions have evolved to be more focused about their centres whilst still displaying planforms that follow the directions expected by tomographic studies.

Our final viscosity structure featured a much less viscous layer above the CMB (shown in fig. 7.6). As in our other models the differences between the classic and adjoint models is the focus of the fine upwelling features, with classic models having upwellings spread over a larger area. Over the 40 Myr assimilation period the classic model does not show the same level of lateral change as case 2, with the perceived boundary between the two hot regions following the figures central longitude not becoming more distinct.

In contrast the adjoint model again displays very distinct upwelling regions over the course of the circulation calculation. The initial condition at 40 Ma, similar to case 2, shows two separate hotter than average regions which contain some hot/cold banding hinting at some numerical instability in calculating this starting point. As before though, following 20 Myr of convection we have two hot anomaly regions that have planforms similar to the LLSVPs observed in tomographic models. The final present day structure is very similar to the Pacific anomaly present in case 2, with more focused upwelling features within the areas imaged in the tomography. The African anomaly in contrast appears somewhere between cases 1 and 2, with a longer north to south east shape as in case 1, but with more focused features as in case 2.

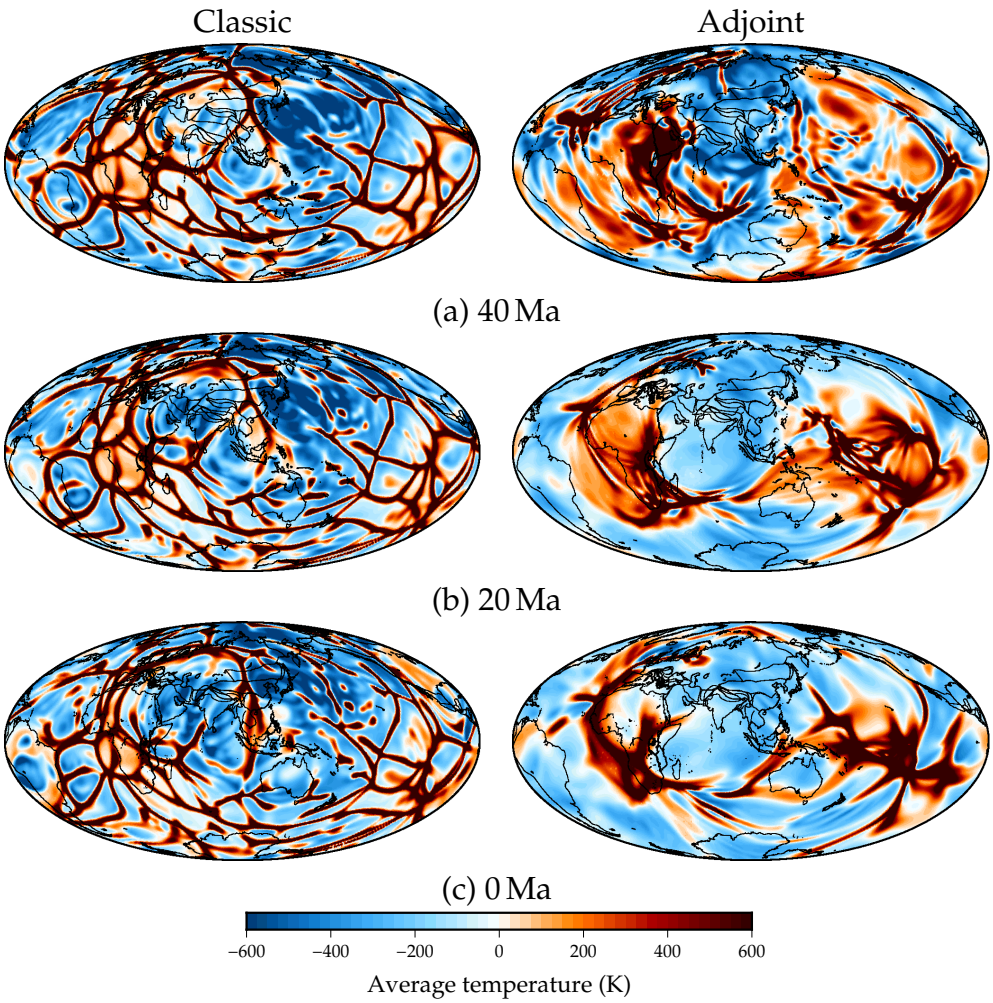

Fig. 7.6 Average temperature plots at 2800 km for different stages for the case 3 viscosity profile for the classic (left), and adjoint derived initial condition (right) mantle circulation models. Black lines denote current age coastlines.

7.3.2 Comparison between modelled final velocity structures to the S40RTS tomography model

As a final step, we convert the present day temperature structures to shear wave velocities using the mineral based lookup tables of Stixrude and Lithgow-Bertelloni (2011), assuming a pyrolitic mantle composition. We also apply a resolution filter to our derived seismic structure which accounts for the regional bias of the tomographic model we compare to, the S40RTS shear wave tomography model (Ritsema et al. 2007; Ritsema et al. 2011). Such a conversion method has been shown to provide a clearer picture for comparing circulation model outputs to tomographic models due to the reduction in amplitude of perturbations (Schuberth et al. 2009a; Bull et al.

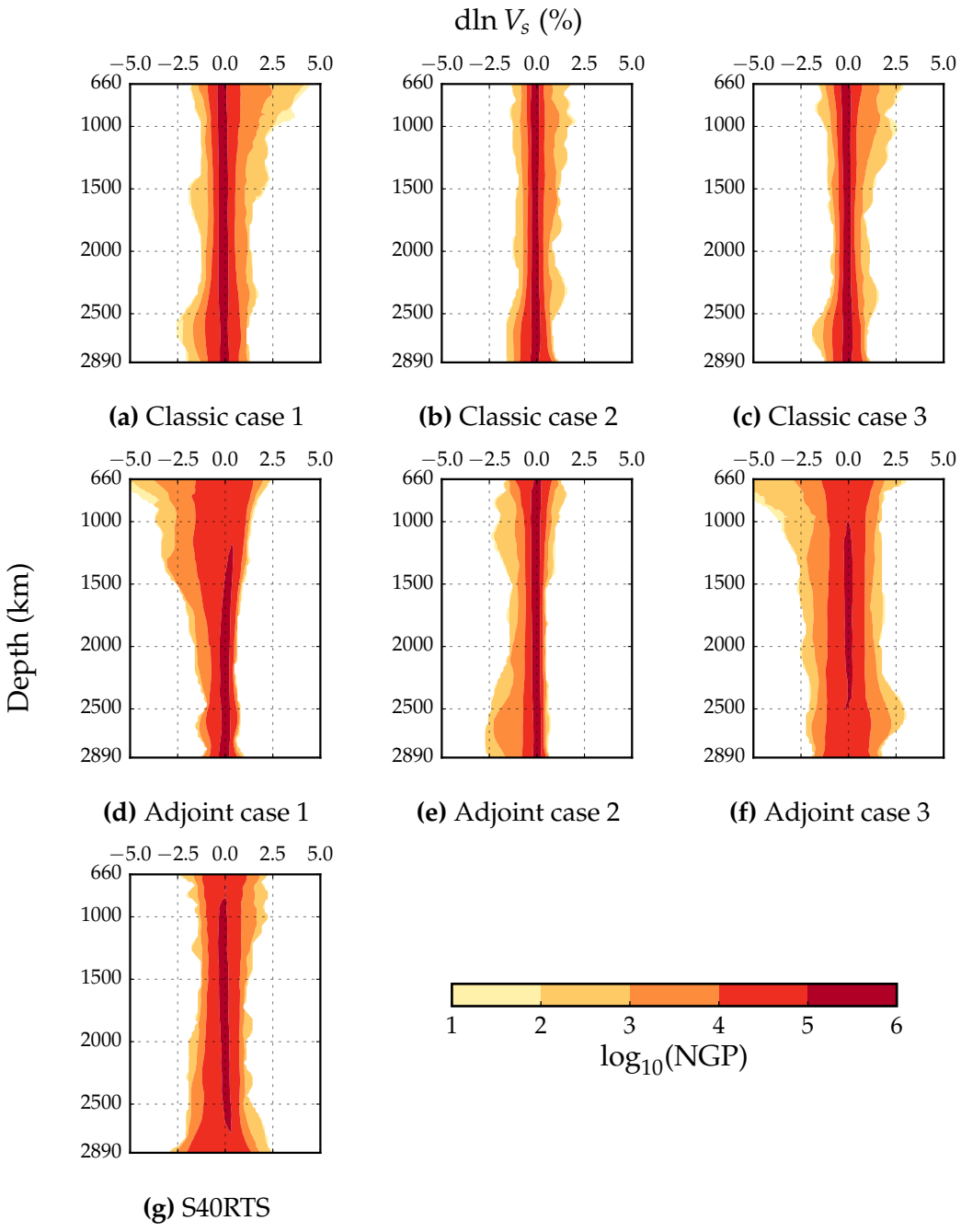

(a) Classic case 1 **(b)** Classic case 2 **(c)** Classic case 3

(d) Adjoint case 1 **(e)** Adjoint case 2 **(f)** Adjoint case 3

(g) S40RTS

Fig. 7.7 Histograms of perturbations in V_s for the various classic and adjoint viscosity cases, together with those of S40RTS. Logarithmic colour scale and contours indicates the number of grid point (NGP) for a given depth.

2009). In fig. 7.7 we display histograms of the V_s perturbations for the lower mantle as a function of depth for the six cases as well as for the S40RTS model for reference.

Looking at case 1 (figs. 7.7a and 7.7d) we see that there is noticeable difference between the distribution of velocities. For both we see the largest amplitudes are present in the uppermost parts of the lower mantle, however the overall skew in the classic case is positive whilst negative in the adjoint model. This skew is less significant below 2000 km depth for both cases, with both models displaying an overall skew to negative values as observed in S40RTS. This skew to negative perturbations has also been noted from other tomographic models (Hernlund and Houser 2008).

For case 2 (figs. 7.7b and 7.7e) there is less difference between the two models with the majority of the perturbations located within $\pm 1\%$ at all depths. While the classic case has no marked skew, the adjoint case shows a much narrower spread of points with an overall negative skew across the lower mantle.

For the final viscosity profile looked at in this study ((figs. 7.7c and 7.7f), we see that using the adjoint initial condition again has a significant difference on the V_s perturbations. The classic case has a very narrow spread of values (typically $\pm 1\%$) whereas the adjoint case has values spread over twice the range. The $\log_{10}(\mathrm{NGP}) = 4$ and greater contours for the adjoint show the closest match to the S40RTS model, although the tomography model has a much tighter overall spread.

Overall we see that adjoint cases 1 and 3 produce the most substantial deviation from the classic approach, with a larger spread for the majority of points. The classic cases and adjoint case 2 meanwhile all display a much narrower distribution across the entire lower mantle.

7.4 Discussion

We have compared the results of 40 Myr MCMs that use initial conditions derived from either assimilating the 200 Ma to 40 Ma plate histories, or by performing forward-adjoint calculations over 40 Myr that assimilate the S40RTS tomography model. We have also varied the viscosity profile for these models and observed the effects this has on the mantle flow over the 40 Myr assimilation period. Finally by utilising the mineral based lookup

tables of Stixrude and Lithgow-Bertelloni (2011) we convert the present day temperature field to seismic velocities and account for the limited resolution of tomographic models (Ritsema et al. 2007).

The most remarkable difference is between the very stiff lower mantle used in case 1 compared to the other cases. We see that the high viscosity of case 1 has limited the movement of the lower mantle features for the adjoint constructed initial condition. This high viscosity lower mantle is the same as is used in Horbach et al. (2014), where there was also very limited deviation of lower mantle structures. In comparison, cases 2 and 3 both see much more dynamic movement of the hotter than average features, being more easily influenced by the continuing convective processes over the 40 Myr period. Cases 2 and 3 also show structures more similar to their classic counterparts with features concentrated into the finger like upwelling bands seen in the classic case.

When considering the information from the histograms of the velocity perturbations we note that each layer in our models contain over six hundred thousand grid points; therefore the contours below $\log_{10}(\mathrm{NGP}) = 4$ represent only 1% of the total number of points in the layer. Taking this into consideration we see that despite the spread of perturbations in the adjoint cases being wider than seen in the tomography and classic cases, the main distribution of values ($\geq \log_{10}(\mathrm{NGP}) = 4$) in adjoint case 3 best line up with S40RTS distribution.

The difference in the deep mantle flow patterns between the initial conditions is of interest, as it has the potential to alter current ideas of the dynamic topography in the past. Estimates of topography have been known to differ over regional areas by an order of magnitude (Muller et al. 2008). Such differences would imply that a region is or is not above sea level which has great economic interest, as knowledge of past sea levels is of great importance in resource exploration. Studies by Spasojevic et al. (2009), Shephard et al. (2010), and Shephard et al. (2012b) employ a simplified adjoint model to perform such observations by deriving an initial condition for the Americas at 50 Ma.

MCM studies regularly employ compressibility, phase transitions and lateral viscosity variations, whereas these are still in their infancy for adjoint models. These studies can also see good matches to present day heterogeneity for higher lower mantle viscosities (Schuberth et al. 2009a). Because of this we must take caution when drawing conclusions for a preferred viscos-

ity structure as the models presented in this study, whilst having a number of characteristics of Earth do not cover the full range of Earth dynamics. We acknowledge that it has recently been shown that compressibility can be incorporated into adjoint models by using compressible equations for convection in the forward model and incompressible equations for the adjoint calculation without affecting the convergence of the forward-adjoint (Ghelichkhan and Bunge 2016).

Alternative methods for constraining the viscosity profile are currently being undertaken such as in the work of Atkins et al. (2016). In this study, the authors use pattern recognition techniques to make inferences on model parameters, such as the viscosity profile for 2D mantle models. While their study serves as a proof of concept currently (without the added complexities of moving to an extra dimension with 3D models), such techniques show promise as an additional pathway to helping improve estimates of mantle parameters.

This result paves the way for more Earth like investigations to be undertaken using the adjoint method. Thanks to the work of Ghelichkhan and Bunge (2016) it is possible incorporate complex dynamics into forward-adjoint models using the a compressible forward. Including the additional dynamics of compressibility will help clarify the potential for adjoint models to be a useful tool towards understanding mantle dynamics.

7.5 Conclusion

We have presented models that investigate the longevity of thermal structures that can be inferred as the source of LLSVPs from shear wave tomographic models for the last 40 Ma. Using a range of viscosity profiles we have constructed a temperature profile for the mantle flow using both a classic mantle circulation model, as well as assimilating present day information using adjoint methods.

The planforms of the African and Pacific structures show great variability in their evolution depending on both the initial condition and viscosity profile. Their positions at present day also vary significantly between classic and adjoint derived initial condition models, with adjoint models generating V_s perturbations that show a better match to the tomography at depth. These results suggest that viscosity profiles that feature a low viscous base and a

moderate $\times 30\eta$ lower mantle best matches tomography models. However, other studies that incorporate a greater set of the physics describing the mantle find matches for higher viscosity values for the deep mantle. To this end, introducing more complex rheologies and the effects of compressibility would better position adjoint derived initial conditions in addressing the question of the ideal viscosity structure for the mantle.

CHAPTER 8

CONCLUSIONS

In this thesis we have been motivated by the simple question surrounding the choice of the initial condition in MCMs. As computational power increases and with advancements in the numerical model allowing more sophisticated descriptions of the physical processes, the choice of initial condition is one of greater importance. While various studies have looked at smaller sections of this problem, we aimed here to investigate the entire issue of initial conditions, from the effects of its choice to how to better determine one.

8.1 Summary of research

At the start of this thesis we posed three questions that we aimed to address over the course of the undertaken research. The questions we presented were:

1. How accurate are our current methods of calculating mantle flow?
2. In what ways can we better constrain our understanding of past mantle flow?
3. Are these methods an improvement over current techniques in helping understand current questions in geodynamics?

By addressing these questions we hoped to provide a clear picture of the initial condition for MCMs, from how it affects current models, to how we can improve it, and finally to how an improved initial condition may change results. To conclude we now revisit these questions and summarise our findings.

How accurate are our current methods of calculating mantle flow?

The beginning of our investigations into the initial conditions for MCMs was based around the idea of chaotic growth and the results of Bello et al. (2014), which stated that there is a limit of predictability to our models. In Chapter 3 we readdressed the methods of Bello et al. (2014), which exclusively looked at models which did not prescribe a surface boundary condition as would be the case in circulation models.

In our work we took the surface velocity field from the reference twin and assimilated this as the surface boundary condition for the perturbed twin, alongside a free slip perturbed twin. By prescribing a surface boundary condition we found that the notion of limits of predictability are redundant in these cases, with values far exceeding the length of plate reconstructions, corroborating the results found in Colli et al. (2015). Furthermore, by varying the heating mode for models we found that the Lyapunov times for models heated internally are the shortest. The implication of this being that internal heating has a greater effect on any growth of errors as models progress.

Overall in answering this question we find that mantle models that prescribe a surface boundary, such as in MCM studies, and which are investigating questions based on the final output, will not be influenced by the choice in initial condition since errors are reduced over the assimilation period. This does not however, vindicate studies that look at the long term past mantle, as the errors are reduced over the assimilation period, and not instantaneously. While this can be avoided by refocusing studies to, investigate potential start states for imaged deep mantle structures for example, these only slightly constrain our understanding of past mantle flow. It does not provide us with a unique picture for the past mantle flow based on all available observations, something that we addressed in the rest of this research.

In what ways can we better constrain our understanding of past mantle flow?

Beginning in Chapter 4 we presented the main numerical methods that attempt to answer this question. After choosing the method of variation assimilation (the adjoint) we presented the adjoint equations for mantle convection (with a derivation in Appendix B) and in detail for the first time, the steps required to implement a successful forward-adjoint iteration model into a mantle convection code. Following this, through the use of a twin

experiment that utilised a synthetic true reference state, we showed that our implementation of the method worked well.

Through the presentation of the adjoint method, it was clear that while an excellent method, the adjoint method is very computationally intensive. High resolution models need to run on large HPC systems that typically restrict a users CPU time and disk space, both of which are intensively used with this method. Clearly any potential savings in either runtime or disk space would be advantageous, and we showed in Chapter 5 that savings in term of runtime and disk space could be achieved by altering the time stepping mechanism of the model. Such tweaks also had no bearing on the overall accuracy of predicted results making this a useful addition to the forward-adjoint model. We also went on to investigate the method of updating the initial condition, finding that while complex gradient methods yielded a more consistent level of convergence in synthetic tests, simple linear update methods converged much faster before displaying divergence. When considering this in terms of HPC system usage, we once again conclude that the apparent compromise to cruder methods is beneficial, with the calculations requiring less CPU time to reach satisfactory convergence levels.

The final conclusion from our synthetic testing was that high accuracy reconstruction of mantle structures was only reliably achieved for calculations extending back between 80 Ma to 40 Ma. Forward-adjoint calculations that ran over longer time intervals displayed a poorer convergence rate, and less detailed reconstruction of features over their twenty iterations. Of course extra iterations could change this, such as in Bunge et al. (2003) where they ran models for 100 iterations. This is however, impractical for the same reasons given previously for adjoint calculations, and represents a major limitation for the method.

Whilst we acknowledge this limitation, it does not deter us from further investigations as the method had been shown to have excellent convergence over shorter time frames. Chapter 6 continued our investigations into the overall method of the forward-adjoint by looking at the mismatch calculation at present day. Previous studies that utilise Earth observations from seismic tomography did not investigate the effects of the difference in resolution between the tomography and modelled fields. This, of course, left room for an investigation into how the differing resolutions impacted convergence.

To this end we utilised the resolution filter of the S20RTS and S40RTS models (Ritsema et al. 2004; Ritsema et al. 2011) to account for this drop

in resolution in our modelled data before computing any mismatches. Of course, further uncertainties in the mismatch calculation are created when using data sources that are not already a temperature field, with a conversion to a temperature field required for such data. We analysed this by converting our modelled temperature field to a velocity field and then back to temperature and found no difference to the case where no conversions of the modelled data were used. In our findings, we then found that methods of computing the mismatch performed equally well as long as the respective resolution filters were not applied to the model data. This result was somewhat surprising, however it does reduce the complexity in calculations as not requiring any conversion of the model data before computing the mismatch has significant savings in terms of CPU time.

We do acknowledge however, that the true data will always have a lower resolution and require converting to temperatures and so there will always be some base level of uncertainty in these adjoint models. This does not overly impact the adjoint methods effectiveness compared to other forward model techniques, as this method is still assimilating more information than those studies.

Overall, in these three chapters we have unequivocally shown that methods exist that can better constrain estimates of past mantle flow. We acknowledge that we have only shown one such method, albeit with a rigorous testing of its implementation. Testing of other methods such as the QRV method (Ismail-Zadeh et al. 2007; Glišović and Forte 2014), which has been shown to perform equally well as the adjoint, lies beyond the scope of this thesis where we ultimately chose to fully understand the adjoint method. This decision was based on the lack of available information on implementations and robustness of the adjoint method in the geodynamics literature.

Are these methods an improvement over current techniques in helping understand current questions in geodynamics?

With the final question that we posed, we aimed to introduce a method that can constrain past mantle flow to a real Earth situation in earnest. To this end, in Chapter 7, we investigated high resolution models that use the forward-adjoint method.

In this chapter we have seen that over a 40 Myr calculation, classic forward models and adjoint based models generate remarkably different flow

patterns. The planform of present day thermal structures was seen to vary greatly, with the adjoint based models having two focused positive thermal anomalies in the locations of observed LLSVPs. The classic models on the other hand had positive thermal anomalies spread over a much larger area. We have also seen that the choice in viscosity structure also has an influence on the adjoint based models. Having a high viscosity produced a mantle characterised by two features very reminiscent of the tomography model used, while lower viscosities showed more variation during their evolution.

These results suggest that adjoint models can indeed be used to improve our understanding of current questions. The markedly different flow patterns that appear from incorporating present day observations provide an alternative perspective on the mantle evolution from current methods.

8.2 The place of adjoint models and future work

The adjoint for mantle models sits in a unique position that allows investigations into areas with which current forward techniques will always struggle without a constrained initial condition. We have shown that the method works best when being ran over intervals between 40 Myr to 80 Myr, which while not as wide an interval as hoped, still places this method as an excellent tool for mantle studies. While forward models still undeniably have great use, the ability to construct a picture of mantle flow over this period has clear benefits in studies that would look to investigate phenomena such as true polar wander, dynamic topography changes, and the touched upon placement of the large scale deep mantle structures. These areas would benefit greatly from these inverse techniques.

Of course, the method is still greatly untapped despite the work presented in this thesis. One potential method that we have not investigated in this thesis is the option of 'chaining' time intervals together using the adjoint. As we have seen it is difficult to project information back in time beyond a certain age. We pose the question, would an adjoint model running 0 Ma to 40 Ma followed by a second adjoint that runs 40 Ma to 80 Ma carry information back better than the attempted 0 Ma to 80 Ma presented in this thesis? This idea is not dissimilar from the iteration steps employed in Ismail-Zadeh et al. (2004), although their implementation was not for the full adjoint.

A second question is whether the adjoint method could be extended to compositional mantle flow? The potential applications of such a method are clear with the current debate over potential dense piles on the CMB. The equations for mantle convection contain a fourth equation for composition which is also time-dependent (see Section B.8). Having a second time-dependent equation, together with a fourth term C, requires additional initial and boundary conditions for C, as well as requiring a true compositional field, C_t at present day to compare a modelled composition C_m to. Implementing such a set of equations would require additional assumptions that are not immediately clear.

It is clear from the growing body of literature regarding inverse and assimilation techniques that the geodynamics research community is embracing techniques that utilise the wealth of present day observations to improve estimates of the mantle's history. From the adjoint methods covered here and by others such as Bunge et al. (2003), Horbach et al. (2014), and Ghelichkhan and Bunge (2016); to the QRV methods of Ismail-Zadeh et al. (2007) and Glišović and Forte (2014); or to innovative methods that zero in on constraints of mantle parameters using pattern recognition and statistics as in Atkins et al. (2016); we see that these methods are becoming a valuable tool in any modellers toolbox thanks to their additional insights.

References

Alfè, D., Gillan, M., and Price, G. (2002). Composition and temperature of the Earth's core constrained by combining ab initio calculations and seismic data. *Earth and Planetary Science Letters* **195**, 91–98.

Atkins, S., Valentine, A. P., Tackley, P. J., and Trampert, J. (2016). Using pattern recognition to infer parameters governing mantle convection. *Physics of the Earth and Planetary Interiors* **257**, 171–186.

Austermann, J., Kaye, B. T., Mitrovica, J. X., and Huybers, P. (2014). A statistical analysis of the correlation between large igneous provinces and lower mantle seismic structure. *Geophysical Journal International* **197**, 1–9.

Baumgardner, J. R. (1985). Three-dimensional treatment of convective flow in the Earth's mantle. *Journal of Statistical Physics* **39**, 501–511.

Baumgardner, J. R. and Frederickson, P. O. (1985). Icosahedral discretization of the two-sphere. *SIAM Journal on Numerical Analysis* **22**, 1107–1115.

Baumgardner, J. R. (1983). A three-dimensional finite element model for mantle convection. University of California, Los Angeles.

Becker, T. W. and Boschi, L. (2002). A comparison of tomographic and geodynamic mantle models. *Geochemistry, Geophysics, Geosystems* **3**, 1003.

Bello, L., Coltice, N., Rolf, T., and Tackley, P. J. (2014). On the predictability limit of convection models of the Earth's mantle. *Geochemistry, Geophysics, Geosystems* **15**, 2319–2328.

Benettin, G., Galgani, L., Giorgilli, A., and Strelcyn, J.-M. (1980). Lyapunov characteristic exponents for smooth dynamical systems and for hamiltonian systems: A method for computing all of them. Part 1: Theory. *Meccanica* **15**, 9–20.

Boffetta, G., Giuliani, P., Paladin, G., and Vulpiani, A. (1998). An extension of the lyapunov analysis for the predictability problem. *Journal of the Atmospheric Sciences* **55**, 3409–3416.

Bower, D. J., Gurnis, M., and Seton, M. (2013). Lower mantle structure from paleogeographically constrained dynamic Earth models. *Geochemistry, Geophysics, Geosystems* **14**, 44–63.

Boyden, J. A., Müller, R. D., Gurnis, M., Torsvik, T. H., Clark, J. A., Turner, M., Ivey-Law, H., Watson, R. J., and Cannon, J. S. (2011). Next-generation

plate-tectonic reconstructions using GPlates. In: *Geoinformatics*. Ed. by G. R. Keller and C. Baru. Cambridge University Press, 95–114.

Brandenburg, J. P. and van Keken, P. E. (2007). Deep storage of oceanic crust in a vigorously convecting mantle. *Journal of Geophysical Research: Solid Earth* **112**, B06403.

Bull, A. L., Domeier, M., and Torsvik, T. H. (2014). The effect of plate motion history on the longevity of deep mantle heterogeneities. *Earth and Planetary Science Letters* **401**, 172–182.

Bull, A., McNamara, A., Becker, T., and Ritsema, J. (2010). Global scale models of the mantle flow field predicted by synthetic tomography models. *Physics of the Earth and Planetary Interiors* **182**, 129–138.

Bull, A., McNamara, A., and Ritsema, J. (2009). Synthetic tomography of plume clusters and thermochemical piles. *Earth and Planetary Science Letters* **278**, 152–162.

Bunge, H. and Baumgardner, J. R. (1995). Mantle convection modeling on parallel virtual machines. *Computers in Physics* **9**, 207–215.

Bunge, H.-P. and Davies, J. H. (2001). Tomographic images of a mantle circulation model. *Geophysical Research Letters* **28**, 77–80.

Bunge, H.-P., Hagelberg, C. R., and Travis, B. J. (2003). Mantle circulation models with variational data assimilation: Inferring past mantle flow and structure from plate motion histories and seismic tomography. *Geophysical Journal International* **152**, 280–301.

Bunge, H.-P., Richards, M. A., and Baumgardner, J. R. (1996). Effect of depth-dependent viscosity on the planform of mantle convection. *Nature* **379**, 436–438.

Bunge, H.-P., Richards, M. A., and Baumgardner, J. R. (1997). A sensitivity study of three-dimensional spherical mantle convection at 10^8 Rayleigh number: Effects of depth-dependent viscosity, heating mode, and an endothermic phase change. *Journal of Geophysical Research: Solid Earth* **102**, 11991–12007.

Bunge, H.-P., Richards, M. A., Lithgow-Bertelloni, C., Baumgardner, J. R., Grand, S. P., and Romanowicz, B. A. (1998). Time scales and heterogeneous structure in geodynamic Earth models. *Science* **280**, 91–95.

Bunge, H.-P., Richards, M. A., and Baumgardner, J. R. (2002). Mantle circulation models with sequential data assimilation: Inferring present-day mantle structure from plate-motion histories. *Philosophical Transactions of the Royal Society A: Mathematical, Physical and Engineering Sciences* **360**, 2545–2567.

Cannon, J., Lau, E., and Müller, R. D. (2014). Plate tectonic raster reconstruction in GPlates. *Solid Earth* **5**, 741–755.

Colli, L., Bunge, H.-P., and Schuberth, B. S. A. (2015). On retrodictions of global mantle flow with assimilated surface velocities. *Geophysical Research Letters* **42**, 8341–8348.

Conrad, C. P. and Gurnis, M. (2003). Seismic tomography, surface uplift, and the breakup of Gondwanaland: Integrating mantle convection backwards in time. *Geochemistry, Geophysics, Geosystems* **4**, 1031.

Conrad, C. P., Lithgow-Bertelloni, C., and Louden, K. E. (2004). Iceland, the Farallon slab, and dynamic topography of the North Atlantic. *Geology* **32**, 177–180.

Courtier, P. and Talagrand, O. (1987). Variational assimilation of meteorological observations with the adjoint vorticity equation. II: Numerical results. *Quarterly Journal of the Royal Meteorological Society* **113**, 1329–1347.

Davies, D. R., Davies, J. H., Bollada, P. C., Hassan, O., Morgan, K., and Nithiarasu, P. (2013). A hierarchical mesh refinement technique for global 3-D spherical mantle convection modelling. *Geoscientific Model Development* **6**, 1095–1107.

Davies, D. R., Goes, S., and Lau, H. C. P. (2015a). Thermally dominated deep mantle LLSVPs: A Review. In: *The Earth's Heterogeneous Mantle: A Geophysical, Geodynamical, and Geochemical Perspective*. Ed. by A. Khan and F. Deschamps. Springer International Publishing, 441–477.

Davies, D. R., Goes, S., Davies, J., Schuberth, B., Bunge, H.-P., and Ritsema, J. (2012). Reconciling dynamic and seismic models of Earth's lower mantle: The dominant role of thermal heterogeneity. *Earth and Planetary Science Letters* **353-354**, 253–269.

Davies, D. R. (2008). Applying multi-resolution numerical methods to geodynamics. Cardiff University.

Davies, D., Goes, S., and Sambridge, M. (2015b). On the relationship between volcanic hotspot locations, the reconstructed eruption sites of large igneous provinces and deep mantle seismic structure. *Earth and Planetary Science Letters* **411**, 121–130.

Davies, G. F. (1999). Dynamic Earth: Plates, plumes and mantle convection. Cambridge University Press.

Davies, J. H. (2005). Steady plumes produced by downwellings in Earth-like vigor spherical whole mantle convection models. *Geochemistry, Geophysics, Geosystems* **6**, Q12001.

Deschamps, F., Li, Y., and Tackley, P. J. (2015). Large-scale thermo-chemical structure of the deep mantle: Observations and models. In: *The Earth's Heterogeneous Mantle: A Geophysical, Geodynamical, and Geochemical Perspective*. Ed. by A. Khan and F. Deschamps. Springer International Publishing, 479–515.

Deschamps, F., Tackley, P. J., and Nakagawa, T. (2010). Temperature and heat flux scalings for isoviscous thermal convection in spherical geometry. *Geophysical Journal International* **182**, 137–154.

Dziewonski, A. M., Hager, B. H., and O'Connell, R. J. (1977). Large-scale heterogeneities in the lower mantle. *Journal of Geophysical Research* **82**, 239–255.

Fletcher, R. and Reeves, C. M. (1964). Function minimization by conjugate gradients. *The Computer Journal* **7**, 149–154.

Forte, A. M., Dziewonski, A. M., and O'Connell, R. J. (1995). Continent-ocean chemical heterogeneity in the mantle based on seismic tomography. *Science* **268**, 386–388.

Forte, A. M. and Mitrovica, J. X. (2001). Deep-mantle high-viscosity flow and thermochemical structure inferred from seismic and geodynamic data. *Nature* **410**, 1049–1056.

Forte, A. M. and Peltier, R. (1991). Viscous flow models of global geophysical observables: 1. Forward problems. *Journal of Geophysical Research: Solid Earth* **96**, 20131–20159.

French, S. W. and Romanowicz, B. (2015). Broad plumes rooted at the base of the Earth's mantle beneath major hotspots. *Nature* **525**, 95–99.

Fukao, Y., Obayashi, M., Nakakuki, T., and the Deep Slab Project Group (2009). Stagnant slab: A review. *Annual Review of Earth and Planetary Sciences* **37**, 19–46.

Garel, F., Goes, S., Davies, D. R., Davies, J. H., Kramer, S. C., and Wilson, C. R. (2014). Interaction of subducted slabs with the mantle transition-zone: A regime diagram from 2-D thermo-mechanical models with a mobile trench and an overriding plate. *Geochemistry, Geophysics, Geosystems* **15**, 1739–1765.

Garnero, E. J. and McNamara, A. K. (2008). Structure and dynamics of Earth's lower mantle. *Science* **320**, 626–628.

Garnero, E. J., McNamara, A. K., and Shim, S.-H. (2016). Continent-sized anomalous zones with low seismic velocity at the base of Earth's mantle. *Nature Geoscience* **9**, 481–489.

Ghelichkhan, S. and Bunge, H.-P. (2016). The compressible adjoint equations in geodynamics: Derivation and numerical assessment. *GEM - International Journal on Geomathematics* **7**, 1–30.

Glišović, P. and Forte, A. M. (2014). Reconstructing the Cenozoic evolution of the mantle: Implications for mantle plume dynamics under the Pacific and Indian plates. *Earth and Planetary Science Letters* **390**, 146–156.

Glišović, P. and Forte, A. M. (2015). Importance of initial buoyancy field on evolution of mantle thermal structure: Implications of surface boundary conditions. *Geoscience Frontiers* **6**, 3–22.

Grand, S. P., van der Hilst, R. D., and Widiyantoro, S. (1997). Global seismic tomography: A snapshot of convection in the Earth. *Geological Society of America Today* **7**, 1–7.

Gurnis, M., Mitrovica, J. X., Ritsema, J., and van Heijst, H.-J. (2000). Constraining mantle density structure using geological evidence of surface uplift rates: The case of the African Superplume. *Geochemistry, Geophysics, Geosystems* **1**, 1020.

Gurnis, M., Turner, M., Zahirovic, S., DiCaprio, L., Spasojevic, S., Müller, R., Boyden, J., Seton, M., Manea, V. C., and Bower, D. J. (2012). Plate tectonic reconstructions with continuously closing plates. *Computers & Geosciences* **38**, 35–42.

Hager, B. H. and Richards, M. A. (1989). Long-wavelength variations in Earth's geoid: Physical models and dynamical implications. *Philosophical Transactions of the Royal Society A: Mathematical, Physical and Engineering Sciences* **328**, 309–327.

Hager, B. H. (1984). Subducted slabs and the geoid: Constraints on mantle rheology and flow. *Journal of Geophysical Research: Solid Earth* **89**, 6003–6015.

Hager, B. H., Clayton, R. W., Richards, M. A., Comer, R. P., and Dziewonski, A. M. (1985). Lower mantle heterogeneity, dynamic topography and the geoid. *Nature* **313**, 541–545.

Haskell, N. A. (1937). The viscosity of the asthenosphere. *American Journal of Science* **s5-33**, 22–28.

Hernlund, J. W. and Houser, C. (2008). On the statistical distribution of seismic velocities in Earth's deep mantle. *Earth and Planetary Science Letters* **265**, 423–437.

van der Hilst, R. D., Widiyantoro, S., and Engdahl, E. R. (1997). Evidence for deep mantle circulation from global tomography. *Nature* **386**, 578–584.

Hirose, K., Fei, Y., Ma, Y., and Mao, H.-K. (1999). The fate of subducted basaltic crust in the Earth's lower mantle. *Nature* **397**, 53–56.

Horbach, A., Bunge, H.-P., and Oeser, J. (2014). The adjoint method in geodynamics: Derivation from a general operator formulation and application to the initial condition problem in a high resolution mantle circulation model. *GEM - International Journal on Geomathematics* **5**, 163–194.

Hüttig, C. and Breuer, D. (2011). Regime classification and planform scaling for internally heated mantle convection. *Physics of the Earth and Planetary Interiors* **186**, 111–124.

Ismail-Zadeh, A., Korotkii, A., Schubert, G., and Tsepelev, I. (2007). Quasi-reversibility method for data assimilation in models of mantle dynamics. *Geophysical Journal International* **170**, 1381–1398.

Ismail-Zadeh, A., Korotkii, A., Schubert, G., and Tsepelev, I. (2009). Numerical techniques for solving the inverse retrospective problem of thermal evolution of the Earth interior. *Computers & Structures* **87**, 802–811.

Ismail-Zadeh, A., Schubert, G., Tsepelev, I., and Korotkii, A. (2004). Inverse problem of thermal convection: numerical approach and application to mantle plume restoration. *Physics of the Earth and Planetary Interiors* **145**, 99–114.

Jarvis, G. T. and Mckenzie, D. P. (1980). Convection in a compressible fluid with infinite Prandtl number. *Journal of Fluid Mechanics* **96**, 515–583.

Johannessen, J. A., Balmino, G., Provost, C. L., Rummel, R., Sabadini, R., Sünkel, H., Tscherning, C., Visser, P., Woodworth, P., Hughes, C., Legrand, P., Sneeuw, N., Perosanz, F., Aguirre-Martinez, M., Rebhan, H., and Drinkwater, M. (2003). The European gravity field and steady-state ocean circulation explorer satellite mission: Its impact on geophysics. *Surveys in Geophysics* **24**, 339–386.

Jordan, T. H. (1978). Composition and development of the continental tectosphere. *Nature* **274**, 544–548.

Karato, S.-i. (2008). Deformation of Earth materials: An introduction to the rheology of solid Earth. Cambridge University Press.

Karato, S.-i. and Karki, B. B. (2001). Origin of lateral variation of seismic wave velocities and density in the deep mantle. *Journal of Geophysical Research: Solid Earth* **106**, 21771–21783.

Kennett, B. L. N. and Bunge, H.-P. (2008). Geophysical continua. Cambridge University Press.

King, S. D. (2016). Reconciling laboratory and observational models of mantle rheology in geodynamic modelling. *Journal of Geodynamics* **100**, 33–50.

Koelemeijer, P., Ritsema, J., Deuss, A., and van Heijst, H.-J. (2016). SP12RTS: a degree-12 model of shear- and compressional-wave velocity for Earth's mantle. *Geophysical Journal International* **204**, 1024–1039.

Kronbichler, M., Heister, T., and Bangerth, W. (2012). High accuracy mantle convection simulation through modern numerical methods. *Geophysical Journal International* **191**, 12–29.

Labrosse, S., Hernlund, J. W., and Coltice, N. (2007). A crystallizing dense magma ocean at the base of the Earth's mantle. *Nature* **450**, 866–869.

Lattès, R. and Lions, J. (1969). The method of quasi-reversibility: Applications to partial differential equations. Elsevier.

Lekic, V., Cottaar, S., Dziewonski, A., and Romanowicz, B. (2012). Cluster analysis of global lower mantle tomography: A new class of structure and implications for chemical heterogeneity. *Earth and Planetary Science Letters* **357-358**, 68–77.

Li, C., van der Hilst, R. D., Engdahl, E. R., and Burdick, S. (2008). A new global model for P wave speed variations in Earth's mantle. *Geochemistry, Geophysics, Geosystems* **9**, Q05018.

Lithgow-Bertelloni, C. and Richards, M. A. (1998). The dynamics of Cenozoic and Mesozoic plate motions. *Reviews of Geophysics* **36**, 27–78.

Lithgow-Bertelloni, C. and Silver, P. G. (1998). Dynamic topography, plate driving forces and the African superswell. *Nature* **395**, 269–272.

Liu, L., Spasojevic, S., and Gurnis, M. (2008). Reconstructing Farallon plate subduction beneath North America back to the Late Cretaceous. *Science* **322**, 934–938.

Liu, L. and Gurnis, M. (2008). Simultaneous inversion of mantle properties and initial conditions using an adjoint of mantle convection. *Journal of Geophysical Research: Solid Earth* **113**, B08405.

Liu, Q. and Gu, Y. (2012). Seismic imaging: From classical to adjoint tomography. *Tectonophysics* **566-567**, 31–66.

Liu, X. and Zhong, S. (2016). Constraining mantle viscosity structure for a thermochemical mantle using the geoid observation. *Geochemistry, Geophysics, Geosystems* **17**, 895–913.

Lorenz, E. N. (1965). A study of the predictability of a 28-variable atmospheric model. *Tellus* **17**, 321–333.

Mckenzie, D. P., Roberts, J. M., and Weiss, N. O. (1974). Convection in the Earth's mantle: Towards a numerical simulation. *Journal of Fluid Mechanics* **62**, 465–538.

McNamara, A. K. and Zhong, S. (2005). Thermochemical structures beneath Africa and the Pacific Ocean. *Nature* **437**, 1136–1139.

Mégnin, C., Bunge, H.-P., Romanowicz, B., and Richards, M. A. (1997). Imaging 3-D spherical convection models: What can seismic tomography tell us about mantle dynamics? *Geophysical Research Letters* **24**, 1299–1302.

Menemenlis, D. and Wunsch, C. (1997). Linearization of an oceanic general circulation model for data assimilation and climate studies. *Journal of Atmospheric and Oceanic Technology* **14**, 1420–1443.

Mitrovica, J. and Forte, A. (2004). A new inference of mantle viscosity based upon joint inversion of convection and glacial isostatic adjustment data. *Earth and Planetary Science Letters* **225**, 177–189.

Moucha, R., Forte, A. M., Mitrovica, J. X., and Daradich, A. (2007). Lateral variations in mantle rheology: Implications for convection related surface

observables and inferred viscosity models. *Geophysical Journal International* **169**, 113–135.

Muller, R. D., Sdrolias, M., Gaina, C., Steinberger, B., and Heine, C. (2008). Long-term sea-Level fluctuations driven by ocean basin dynamics. *Science* **319**, 1357–1362.

Müller, R. D., Seton, M., Zahirovic, S., Williams, S. E., Matthews, K. J., Wright, N. M., Shephard, G. E., Maloney, K. T., Barnett-Moore, N., Hosseinpour, M., Bower, D. J., and Cannon, J. (2016). Ocean basin evolution and global-scale plate reorganization events since Pangea breakup. *Annual Review of Earth and Planetary Sciences* **44**, 107–138.

O'Neill, C., Müller, D., and Steinberger, B. (2005). On the uncertainties in hot spot reconstructions and the significance of moving hot spot reference frames. *Geochemistry, Geophysics, Geosystems* **6**, Q04003.

Panasyuk, S. V. and Hager, B. H. (2000). Inversion for mantle viscosity profiles constrained by dynamic topography and the geoid, and their estimated errors. *Geophysical Journal International* **143**, 821–836.

Panet, I., Pajot-Métivier, G., Greff-Lefftz, M., Métivier, L., Diament, M., and Mandea, M. (2014). Mapping the mass distribution of Earth's mantle using satellite-derived gravity gradients. *Nature Geoscience* **7**, 131–135.

Ritsema, J. (1999). Complex shear wave velocity structure imaged beneath Africa and Iceland. *Science* **286**, 1925–1928.

Ritsema, J., Deuss, A., van Heijst, H. J., and Woodhouse, J. H. (2011). S40RTS: A degree-40 shear-velocity model for the mantle from new Rayleigh wave dispersion, teleseismic traveltime and normal-mode splitting function measurements. *Geophysical Journal International* **184**, 1223–1236.

Ritsema, J., van Heijst, H. J., and Woodhouse, J. H. (2004). Global transition zone tomography. *Journal of Geophysical Research: Solid Earth* **109**, B02302.

Ritsema, J., McNamara, A. K., and Bull, A. L. (2007). Tomographic filtering of geodynamic models: Implications for model interpretation and large-scale mantle structure. *Journal of Geophysical Research: Solid Earth* **112**, B01303.

Rudolph, M. L., Leki, V., and Lithgow-Bertelloni, C. (2015). Viscosity jump in Earth's mid-mantle. *Science* **350**, 1349–1352.

Schubert, G., Turcotte, D. L., and Olson, P. (2001). Mantle convection in the Earth and planets. Cambridge University Press.

Schuberth, B. S. A., Bunge, H.-P., and Ritsema, J. (2009a). Tomographic filtering of high-resolution mantle circulation models: Can seismic heterogeneity be explained by temperature alone? *Geochemistry, Geophysics, Geosystems* **10**, Q05W03.

Schuberth, B. S. A., Bunge, H.-P., Steinle-Neumann, G., Moder, C., and Oeser, J. (2009b). Thermal versus elastic heterogeneity in high-resolution mantle circulation models with pyrolite composition: High plume excess temperatures in the lowermost mantle. *Geochemistry, Geophysics, Geosystems* **10**, Q01W01.

Serrin, J. (1959). Mathematical principles of classical fluid mechanics. In: *Encyclopedia of Physics / Handbuch der Physik*. Ed. by C. Truesdell. Springer Science & Business Media, 125–263.

Seton, M., Müller, R., Zahirovic, S., Gaina, C., Torsvik, T., Shephard, G., Talsma, A., Gurnis, M., Turner, M., Maus, S., and Chandler, M. (2012). Global continental and ocean basin reconstructions since 200Ma. *Earth-Science Reviews* **113**, 212–270.

Shephard, G. E., Müller, R. D., Liu, L., and Gurnis, M. (2010). Miocene drainage reversal of the Amazon River driven by plate–mantle interaction. *Nature Geoscience* **3**, 870–875.

Shephard, G., Bunge, H.-P., Schuberth, B., Müller, R., Talsma, A., Moder, C., and Landgrebe, T. (2012a). Testing absolute plate reference frames and the implications for the generation of geodynamic mantle heterogeneity structure. *Earth and Planetary Science Letters* **317-318**, 204–217.

Shephard, G., Liu, L., Müller, R., and Gurnis, M. (2012b). Dynamic topography and anomalously negative residual depth of the Argentine Basin. *Gondwana Research* **22**, 658–663.

Simmons, N. A., Forte, A. M., Boschi, L., and Grand, S. P. (2010). GyPSuM: A joint tomographic model of mantle density and seismic wave speeds. *Journal of Geophysical Research: Solid Earth* **115**, B12310.

Spasojevic, S., Liu, L., and Gurnis, M. (2009). Adjoint models of mantle convection with seismic, plate motion, and stratigraphic constraints: North America since the Late Cretaceous. *Geochemistry, Geophysics, Geosystems* **10**, Q05W02.

Stegman, D. R., Richards, M. A., and Baumgardner, J. R. (2002). Effects of depth-dependent viscosity and plate motions on maintaining a relatively uniform mid-ocean ridge basalt reservoir in whole mantle flow. *Journal of Geophysical Research: Solid Earth* **107**.

Steinberger, B. and Holme, R. (2008). Mantle flow models with core-mantle boundary constraints and chemical heterogeneities in the lowermost mantle. *Journal of Geophysical Research: Solid Earth* **113**, B05403.

Steinberger, B. and Calderwood, A. R. (2006). Models of large-scale viscous flow in the Earth's mantle with constraints from mineral physics and surface observations. *Geophysical Journal International* **167**, 1461–1481.

Steinberger, B. and O'Connell, R. J. (1997). Changes of the Earth's rotation axis owing to advection of mantle density heterogeneities. *Nature* **387**, 169–173.

Steinberger, B. and O'Connell, R. J. (1998). Advection of plumes in mantle flow: implications for hotspot motion, mantle viscosity and plume distribution. *Geophysical Journal International* **132**, 412–434.

Steinberger, B. and Torsvik, T. H. (2008). Absolute plate motions and true polar wander in the absence of hotspot tracks. *Nature* **452**, 620–623.

Steinberger, B. and Torsvik, T. H. (2012). A geodynamic model of plumes from the margins of Large Low Shear Velocity Provinces. *Geochemistry, Geophysics, Geosystems* **13**, Q01W09.

Stewart, C. A. and Turcotte, D. L. (1989). The route to chaos in thermal convection at infinite Prandtl number: 1. Some trajectories and bifurcations. *Journal of Geophysical Research: Solid Earth* **94**, 13707–13717.

Stixrude, L. and Lithgow-Bertelloni, C. (2011). Thermodynamics of mantle minerals - II. Phase equilibria. *Geophysical Journal International* **184**, 1180–1213.

Tackley, P. J. (1996). Effects of strongly variable viscosity on three-dimensional compressible convection in planetary mantles. *Journal of Geophysical Research: Solid Earth* **101**, 3311–3332.

Tackley, P. J. (1998). Three-dimensional simulations of mantle convection with a thermo-chemical basal boundary layer: D"? In: *The Core-Mantle Boundary Region*. Wiley-Blackwell, 231–253.

Tackley, P. J. (2008). Modelling compressible mantle convection with large viscosity contrasts in a three-dimensional spherical shell using the yin-yang grid. *Physics of the Earth and Planetary Interiors* **171**, 7–18.

Tackley, P. J. (2012). Dynamics and evolution of the deep mantle resulting from thermal, chemical, phase and melting effects. *Earth-Science Reviews* **110**, 1–25.

Talagrand, O. and Courtier, P. (1987). Variational assimilation of meteorological observations with the adjoint vorticity equation. I: Theory. *Quarterly Journal of the Royal Meteorological Society* **113**, 1311–1328.

Tan, E., Choi, E., Thoutireddy, P., Gurnis, M., and Aivazis, M. (2006). GeoFramework: Coupling multiple models of mantle convection within a computational framework. *Geochemistry, Geophysics, Geosystems* **7**, Q06001.

Tan, E., Gurnis, M., and Han, L. (2002). Slabs in the lower mantle and their modulation of plume formation. *Geochemistry, Geophysics, Geosystems* **3**, 1–24.

Tanaka, S., Suetsugu, D., Shiobara, H., Sugioka, H., Kanazawa, T., Fukao, Y., Barruol, G., and Reymond, D. (2009). On the vertical extent of the

large low shear velocity province beneath the South Pacific Superswell. *Geophysical Research Letters* **36**, L07305.

Tarantola, A. (1984). Inversion of seismic reflection data in the acoustic approximation. *Geophysics* **49**, 1259–1266.

Thompson, P. F. and Tackley, P. J. (1998). Generation of mega-plumes from the core-mantle boundary in a compressible mantle with temperature-dependent viscosity. *Geophysical Research Letters* **25**, 1999–2002.

Tolstikhin, I., Kramers, J., and Hofmann, A. (2006). A chemical Earth model with whole mantle convection: The importance of a core–mantle boundary layer (D'') and its early formation. *Chemical Geology* **226**, 79–99.

Torsvik, T. H., Müller, R. D., Van der Voo, R., Steinberger, B., and Gaina, C. (2008). Global plate motion frames: Toward a unified model. *Reviews of Geophysics* **46**, RG3004.

Torsvik, T. H., Smethurst, M. A., Burke, K., and Steinberger, B. (2006). Large igneous provinces generated from the margins of the large low-velocity provinces in the deep mantle. *Geophysical Journal International* **167**, 1447–1460.

Tosi, N., Stein, C., Noack, L., Hüttig, C., Maierová, P., Samuel, H., Davies, D. R., Wilson, C. R., Kramer, S. C., Thieulot, C., Glerum, A., Fraters, M., Spakman, W., Rozel, A., and Tackley, P. J. (2015). A community benchmark for viscoplastic thermal convection in a 2-D square box. *Geochemistry, Geophysics, Geosystems* **16**, 2175–2196.

Vynnytska, L. and Bunge, H.-P. (2014). Restoring past mantle convection structure through fluid dynamic inverse theory: Regularisation through surface velocity boundary conditions. *GEM - International Journal on Geomathematics* **6**, 83–100.

Wolstencroft, M., Davies, J., and Davies, D. (2009). Nusselt–Rayleigh number scaling for spherical shell Earth mantle simulation up to a Rayleigh number of 10^9. *Physics of the Earth and Planetary Interiors* **176**, 132–141.

Yang, W. S. (1997). Variable viscosity thermal convection at infinite Prandtl number in a thick spherical shell. University of Illinois.

Zahirovic, S., Müller, R. D., Seton, M., and Flament, N. (2015). Tectonic speed limits from plate kinematic reconstructions. *Earth and Planetary Science Letters* **418**, 40–52.

Zhang, N., Zhong, S., Leng, W., and Li, Z.-X. (2010). A model for the evolution of the Earth's mantle structure since the Early Paleozoic. *Journal of Geophysical Research: Solid Earth* **115**, B06401.

Zhong, S., Zuber, M. T., Moresi, L., and Gurnis, M. (2000). Role of temperature-dependent viscosity and surface plates in spherical shell models of mantle convection. *Journal of Geophysical Research: Solid Earth* **105**, 11063–11082.

Appendix A

Glossary

Forward model notation

These symbols are found in the forward model equations and may also be found in the adjoint equations.

Symbol	Description	Units
C_V	Specific heat at constant volume	$\mathrm{J\,kg^{-1}\,K^{-1}}$
$\boldsymbol{g}$	Gravitational acceleration	$\mathrm{m\,s^{-2}}$
H	Radiogenic heat production	$\mathrm{W\,m^{-3}}$
k	Thermal conductivity	$\mathrm{W\,m^{-1}\,K^{-1}}$
$\boldsymbol{n}$	Normal vector	–
P	Pressure	Pa
T	Temperature	K
t	Time	s
$\boldsymbol{u}$	Fluid flow	$\mathrm{m\,s^{-1}}$
α	Coefficient of thermal expansion	$\mathrm{K^{-1}}$
γ	Grüneisen parameter	–
η	Dynamic viscosity	Pa s
κ	Thermal diffusivity	$\mathrm{m^2\,s^{-1}}$
ρ	Density	$\mathrm{kg\,m^{-3}}$

Adjoint model specific notation

These symbols are found exclusively when using the adjoint equations.

Symbol	Description	Units
T_m	*Model* temperature	K
T_t	*True* temperature	K
τ	Adjoint temperature	K
$\boldsymbol{\phi}$	Adjoint fluid flow	$\mathrm{m\,s^{-1}}$
ψ	Adjoint pressure	Pa
χ	Misfit function of T_m and T_t	K

Other notation

Other notation found through this thesis.

Symbol	Description	Units
Ma	Million years ago	years
Myr	Millions of years	years
Ra_b	Bottom heated Rayleigh number	–
Ra_H	Internally heated Rayleigh number	–
V_s	S-wave velocity	$\mathrm{m\,s^{-1}}$
V_p	P-wave velocity	$\mathrm{m\,s^{-1}}$

APPENDIX B

DERIVATION OF THE ADJOINT EQUATIONS

The following derivation of the adjoint equations for mantle convection follows the general operator approach outlined in Horbach et al. (2014).

B.1 Mathematical requirements - the Fréchet derivative and inner products

In order to derive the adjoint equations we will utilise the Fréchet derivative; which is an extension of the formal definition of a derivative to general operators. While this derivation does not require calculation of the Fréchet derivative, knowledge of its concept and manipulation of terms involving it is required for determining the adjoint equations. To this end we take a small digression to outline the Fréchet derivative.

Let X and Y be Banach spaces and F be an operator such that $F : X \to Y$ for $x \in X$, $y \in Y$. F is said to be Fréchet differentiable at $x_0 \in X$ if and only if there exists a linear operator $L : X \to Y$ such that:

$$\lim_{h \to 0, h \in X} \frac{||F(x_0 + h) - F(x_0) - L(h)||_Y}{||h||_X} = 0$$

where $|| \cdot ||_X$ and $|| \cdot ||_Y$ are norms in X and Y respectively. If the linear operator L exists for all $x \in X$ then we say F is Fréchet differentiable with respect to x with $\mathcal{D}_x F = L$

Since the Fréchet derivative is an extension of the classic definition of a derivative it can be shown that these derivatives follow the standard rules of differentiation; namely the chain and product rules.

We also need to make use of the properties of inner product. The domain D for the mantle convection model is the time interval $I = [t_0, t_1]$ and the spatial domain being the spherical shell V, with $D = I \times V$. For two squared integrable vectorial functions (such as velocity) $f, g \in l^2(D)$

$$\langle f, g \rangle_{l^2} = \int_D f(z) \cdot g(z) \, \mathrm{d}z = \int_I \int_V f(x,t) \cdot g(x,t) \, \mathrm{d}^3x \, \mathrm{d}t$$

Similarly for two squared integrable scalar functions (e.g. pressure or temperature) $F, G \in L^2(D)$

$$\langle F, G \rangle_{L^2} = \int_D F(z)G(z) \, \mathrm{d}z = \int_I \int_V F(x,t)G(x,t) \, \mathrm{d}^3x \, \mathrm{d}t$$

Finally, if a linear and bounded operator $F : X \to Y$ where X, Y are Hilbert spaces, then there exists a unique *adjoint* operator F^* to F where $F^* : Y \to X$ with

$$\langle F(x), y \rangle_Y = \langle x, F^*(y) \rangle_X$$

While we can digress further to prove the properties of the operators we will omit these here, the derivation of the adjoint equations will require these adjoint operators to be explicitly identified for our mantle convection equations.

B.2 Method of optimising a model

In order to optimise our mantle convection models we can imagine the problem as such; we begin with our standard unrestricted model with its arbitrarily determined initial temperature structure at t_0. The trajectory of the initial condition then is corrected using known restraints such as the present day structure of the Earth as determined from a source such as seismic tomography, which yields an optimal fit of the initial temperature to the restraints. To state this mathematically then, the objective function $\chi(p)$ (also known as the misfit function) is a measure of the difference between the reference temperature field and the modelled temperature field. The objective function $\chi(p)$ is dependent on the vector p which consists of the parameters in the model which can affect the final answer of χ. These parameters include the boundary conditions, the initial condition, the data misfit and the mathematical model itself (Bunge et al. 2003). For our case, we

take p as a one-dimensional vector that consists only of our intial condition temperature field T_0, and we look to minimise χ to constrain this initial temperature field.

In order to minimise χ we look to compute the gradient of χ with respect to p. We also make note that we are not only looking for the dependency of χ on p, as χ can also be affected indirectly by the function $u(p)$ (i.e. p would be our initial temperature T_0 but the temperature field T at any given time is dependent on our initial temperature field). Since our model is built on the equations of conservation of mass, momentum and energy which are differential equations, computing their gradient is impractical since they are solved numerically on grid sizes of the order of tens of millions of grid points. With finite difference as a means of computing the gradient of χ ruled out, we turn to the adjoint method as a more efficient way to find the gradient of χ.

Coming back to the Fréchet derivative we now see that if we want to the change of χ by changing the parameter p by an infinitesimal amount Δp we are looking for the Fréchet derivative of χ. Since χ depends on both u and p we apply the chain rule and see

$$\mathcal{D}_p\chi(u,p)(\Delta p) = \frac{\partial\chi(u,p)}{\partial u}(\mathcal{D}_p u(\Delta p)) + \frac{\partial\chi(u,p)}{\partial p}(\Delta p). \tag{B.1}$$

Assuming that we can express χ using the L^2 scalar product and the function $\hat{\chi}$ we can rewrite our derivatives as

$$\mathcal{D}_p\chi(u,p)(\Delta p) = \frac{\partial\langle\hat{\chi}(u,p),1\rangle}{\partial u}(\mathcal{D}_p u(\Delta p)) + \frac{\partial\langle\hat{\chi}(u,p),1\rangle}{\partial p}(\Delta p) \tag{B.2}$$

$$\left\langle\partial_u\hat{\chi}(u,p)(\mathcal{D}_p u(\Delta p)),1\right\rangle + \left\langle\partial_p\hat{\chi}(u,p)(\Delta p),1\right\rangle. \tag{B.3}$$

The total derivative $\mathcal{D}_p u(\Delta p)$ measures the effect that our initial temperature $T_0 = p$ effects the temperature field $T(T_0) = u(p)$ at any point in time and is difficult to calculate by finite differencing. In order to calculate $\mathcal{D}_p\chi$ we look to eliminate the total derivatives from the right hand side of eq. (B.3) with help from our knowledge of the adjoint operator.

$$\mathcal{D}_p\chi(u,p)(\Delta p) = \left\langle(\mathcal{D}_p u(\Delta p)),(\partial_u\hat{\chi}(u,p))^*(1)\right\rangle + \left\langle\Delta p,(\partial_p\hat{\chi}(u,p))^*(1)\right\rangle. \tag{B.4}$$

We now recall the linear operator L found in the definition of the Fréchet derivative, where in this instance L is dependent on the parameters u and p and we assume $L(u,p) = 0$. L may be a combination of differential operators, and for our derivation involving the equations governing mantle convection, it is these equations which make up the function L. Using the chain rule to take the Fréchet derivative of L we obtain:

$$\begin{aligned} 0 &= \mathcal{D}_p L(u,p) && \text{(B.5)}\\ &= \partial_u L(u,p)(\mathcal{D}_p u(\Delta p)) + \partial_p L(u,p)(\Delta p) && \text{(B.6)}\\ &= \left\langle \partial_u L(u,p)(\mathcal{D}_p u(\Delta p)), v \right\rangle + \left\langle \partial_p L(u,p)(\Delta p), v \right\rangle && \text{(B.7)}\\ &= \left\langle (\mathcal{D}_p u(\Delta p)), (\partial_u L(u,p))^*(v) \right\rangle + \left\langle \Delta p, (\partial_p L(u,p))^*(v) \right\rangle && \text{(B.8)} \end{aligned}$$

where similar to before we apply the same idea of scalar products to convert to a weak formulation using a test function v, and the idea of adjoint operators to obtain an expression similar to eq. (B.4) which has isolated the total derivative.

We can now add eq. (B.4) and eq. (B.8) since the latter is homogeneous to give,

$$\begin{aligned} \mathcal{D}_p \chi(u,p)(\Delta p) = \left\langle (\mathcal{D}_p u(\Delta p)), (\partial_u \hat{\chi}(u,p))^*(1) + (\partial_u L(u,p))^*(v) \right\rangle \\ + \left\langle \Delta p, (\partial_p \hat{\chi}(u,p))^*(1) + (\partial_p L(u,p))^*(v) \right\rangle . \end{aligned} \quad \text{(B.9)}$$

If we determine the test function v such that

$$(\partial_u L(u,p))^*(v) = -\partial_u \hat{\chi}(u,p))^*(1) \quad \text{(B.10)}$$

the total derivative term is null and reducing the complexity of our problem. Thus we aim to find the adjoint operator L^* and the test function v that yields eq. (B.10) and allows us to simplify eq. (B.9) to

$$\mathcal{D}_p \chi(u,p)(\Delta p) = \left\langle \Delta p, (\partial_p \hat{\chi}(u,p))^*(1) + (\partial_p L(u,p))^*(v) \right\rangle . \quad \text{(B.11)}$$

We note the presence still of the adjoint operators and test function v, and so deriving these is the main part of this method. With the theory now outlined we can apply this directly to our problem of mantle convection.

B.3 The objective function

The objective function χ that we look to minimise for the mantle model measures the difference of the model temperature at present day $T_\mathrm{m} = T(T_0, x, t_1)$ which is dependent on the initial temperature field; and an observed temperature of the Earth T_t that is based on some external data reading. For our objective function, we will consider the same quadratic functional found in other derivations for adjoint data assimiliation models (Ismail-Zadeh et al. 2004; Liu and Gurnis 2008; Bunge et al. 2003)

$$\chi(T) = \frac{1}{2}\int_V (T_\mathrm{t}(x) - T_\mathrm{m}(x))^2 \,\mathrm{d}^3x \tag{B.12}$$

which we can express as a scalar inner product

$$\langle \hat{\chi}(T, x, t), 1\rangle_{L_2} \tag{B.13}$$

where $\hat{\chi} = \frac{1}{2}(T_\mathrm{t}(x) - T_\mathrm{m}(x))^2\delta(t - t_1)$ Setting $u = T$ and $p = T_0$ in eq. (B.4) we can find the total derivative of the objective function with respect to T_0. We note that our definition for the objective function does not depend on the primary paramater T_0 but indirectly through T which allows us to simplify our total derivative as follows:

$$\mathcal{D}_{T_0}\chi(T)(\Delta T_0) = \langle (\mathcal{D}_{T_0}T(\Delta T_0)), (\partial_T\hat{\chi}(T))^*(1)\rangle + \underbrace{\langle \Delta T_0, (\partial_{T_0}\hat{\chi}(T))^*(1)\rangle}_{=0} \tag{B.14}$$

$$= \langle (\mathcal{D}_{T_0}T(\Delta T_0)), \partial_T\hat{\chi}(T)\rangle\,. \tag{B.15}$$

As discussed previously we need to eliminate $\mathcal{D}_{T_0}T$, which can be achieved through determining the adjoint operators L^* of our underlying equations (eq. (B.18)) using the Fréchet derivative and a chosen test function. I.e. we need to determine the adjoint equation for each of the forward conservation equations.

B.4 Preliminaries

The approach we will employ on each of the conservation equations is to take the total derivative of each equation with respect to T_0 and applied in

the direction ΔT_0. We then look to convert this equation to its weak form by multiplying with a relevant test function and applying the inner product $\langle \cdot, \cdot \rangle_{L^2}$, at which point the aim is then to isolate all terms associated with the total derivative. For ease of reading the resulting equations we will substitute $\widetilde{\cdot} := (\mathcal{D}_{T_0}\widetilde{\cdot})$ to denote the derivative and omit the (ΔT_0) notation for the direction of the total derivative. Using this notation we can rewrite eq. (B.15) as

$$\mathcal{D}_{T_0}\chi(T)(\Delta T_0) = \left\langle \widetilde{T}, \partial_T \hat{\chi}(T) \right\rangle. \tag{B.16}$$

During the derivations we will also make use of a number of vector identities to manipulate equations. We will also make use of the divergence theorem which states the relationship between a volume and surface integral

$$\int_V \nabla \cdot \boldsymbol{u} \, \mathrm{d}V = \int_S \frac{\partial \boldsymbol{u}}{\partial \boldsymbol{n}} \, \mathrm{d}S = \int_S \boldsymbol{u} \cdot \boldsymbol{n} \, \mathrm{d}S \tag{B.17}$$

where $\boldsymbol{n}(x)$ is the outward facing normal vector for $x \in \partial V$.

B.5 Derivation for incompressible flow

With these preliminaries presented we know continue onwards and present a derivation of the adjoint equations for incompressible mantle flow.

B.5.1 The forward equations for incompressible flow

In section 2.2 we outlined the equations that describe incompressible mantle convection

$$\nabla \cdot \boldsymbol{u} = 0 \tag{B.18a}$$

$$\nabla \cdot \left(\eta \{ \nabla \boldsymbol{u} + (\nabla \boldsymbol{u})^T \} \right) - \nabla P + \alpha \rho (T_{\text{av}} - T) \boldsymbol{g} = 0 \tag{B.18b}$$

$$\frac{\partial T}{\partial t} + \boldsymbol{u} \nabla \cdot T - \kappa \nabla^2 T - H = 0. \tag{B.18c}$$

with necessary boundary conditions for the velocity $\boldsymbol{u}$

$$\boldsymbol{u}(x,t) = \boldsymbol{u}_P(x,t) \quad x \in S,\ t \in I \tag{B.19a}$$

$$\Big(\Big(\nabla \boldsymbol{u}(x,t) + (\nabla \boldsymbol{u}(x,t))^T\Big) \cdot \boldsymbol{n}(x)\Big)_{tan} = 0 \quad x \in C,\ t \in I \tag{B.19b}$$

$$\boldsymbol{u}(x,t) \cdot \boldsymbol{n}(x) = 0 \quad x \in \partial V,\ t \in I, \tag{B.19c}$$

pressure P

$$P(x,t) = 0 \quad x \in S, t \in I, \tag{B.20}$$

and temperature T

$$T(x,t) = T_S(x,t) \quad x \in S,\ t \in I \tag{B.21a}$$

$$T(x,t) = T_C(x,t) \quad x \in C,\ t \in I, \tag{B.21b}$$

together with the initial condition on T

$$T(x,t_0) = T_0(x) \quad x \in V. \tag{B.22}$$

As previously discussed it is from these equations and boundary conditions that we derive the set adjoint equations for mantle convection, which we will now proceed to do.

B.5.2 The continuity equation

Starting with the continuity equation when the flow is incompressible, eq. (B.18a), we take the total derivative of the equation with respect to T_0 and apply it in the direction ΔT_0. Doing so obtains the following

$$\nabla \cdot (\mathcal{D}_{T_0}\boldsymbol{u})(\Delta T_0) = 0 \tag{B.23}$$

We then look to convert this equation to its weak form by multiplying with a scalar test function ψ and applying the inner product $\langle \cdot, \cdot \rangle_{L^2}$.

$$\langle \psi, \nabla \cdot \widetilde{\boldsymbol{u}} \rangle_{L^2} = 0 \tag{B.24}$$

In order to isolate the total derivative $\widetilde{\boldsymbol{u}}$ we use the vector identity $f\nabla \cdot \boldsymbol{u} + \boldsymbol{u} \cdot \nabla f = \nabla \cdot (f\boldsymbol{u})$ together with the divergence theorem eq. (B.17) allows

eq. (B.24) to be rewritten as

$$\begin{aligned}\int_I \int_V \psi \nabla \cdot \widetilde{\boldsymbol{u}} \, \mathrm{d}^3x \, \mathrm{d}t &= \int_I \int_V \nabla \cdot (\psi \widetilde{\boldsymbol{u}}) \, \mathrm{d}^3x \, \mathrm{d}t - \int_I \int_V \widetilde{\boldsymbol{u}} \nabla \cdot \psi \, \mathrm{d}^3x \, \mathrm{d}t \\ &= \int_I \int_{\partial V} (\psi \widetilde{\boldsymbol{u}}) \cdot \boldsymbol{n} \, \mathrm{d}^2x \, \mathrm{d}t - \int_I \int_V \widetilde{\boldsymbol{u}} \nabla \cdot \psi \, \mathrm{d}^3x \, \mathrm{d}t \end{aligned} \tag{B.25}$$

If we prescribe $\psi(\boldsymbol{x}, t) = 0$ for $\boldsymbol{x} \in \partial V, t \in I$ the surface integral on ∂V is zero and we obtain the homogeneous weak formulation of eq. (B.23)

$$\langle \psi, \nabla \cdot \widetilde{\boldsymbol{u}} \rangle_{L^2} = -\langle \widetilde{\boldsymbol{u}}, \nabla \psi \rangle_{l^2} = 0. \tag{B.26}$$

B.5.3 The momentum equation

For the momentum equation eq. (B.18b), we follow the same approach taking the total derivative in ΔT_0

$$\begin{aligned}\nabla \cdot \left\{ \eta (\nabla (\mathcal{D}_{T_0} \boldsymbol{u})(\Delta T_0) + (\nabla (\mathcal{D}_{T_0} \boldsymbol{u})(\Delta T_0))^T) \right\} - \nabla (\mathcal{D}_{T_0} P)(\Delta T_0) \\ + \alpha \rho ((\mathcal{D}_{T_0} T_{av})(\Delta T_0) - (\mathcal{D}_{T_0} T)(\Delta T_0)) \boldsymbol{g} = 0. \end{aligned} \tag{B.27}$$

We note that the derivative of T_{av} with respect to T_0 vanishes since T_{av} is independent of T_0, before converting to its weak formulation by multiplying the equation by the vector test function $\boldsymbol{\phi}$ and taking the inner product giving

$$\left\langle \boldsymbol{\phi}, \nabla \cdot \eta ((\nabla \widetilde{\boldsymbol{u}}) + (\nabla \widetilde{\boldsymbol{u}})^T) \right\rangle_{l^2} - \left\langle \boldsymbol{\phi}, \nabla \widetilde{P} \right\rangle_{l^2} - \left\langle \boldsymbol{\phi}, \alpha \rho \widetilde{T} \boldsymbol{g} \right\rangle_{l^2} = 0. \tag{B.28}$$

Using the identity $\boldsymbol{v} \cdot (\nabla \cdot (f \nabla \boldsymbol{u})) - \boldsymbol{u} \cdot (\nabla \cdot (f \nabla \boldsymbol{v})) = \nabla \cdot (f(\nabla \boldsymbol{u})\boldsymbol{v}) - \nabla \cdot (f(\nabla \boldsymbol{v})\boldsymbol{u})$ (where $\boldsymbol{u} = \widetilde{\boldsymbol{u}}$, $\boldsymbol{v} = \boldsymbol{\phi}$ and $f = \eta$) on the first inner product we obtain the expression

$$\begin{aligned}\left\langle \boldsymbol{\phi}, \nabla \cdot \eta \left((\nabla \widetilde{\boldsymbol{u}}) + (\nabla \widetilde{\boldsymbol{u}})^T \right) \right\rangle_{l^2} &= \int_I \int_V \nabla \cdot \eta \left((\nabla \widetilde{\boldsymbol{u}}) + (\nabla \widetilde{\boldsymbol{u}})^T \right) \boldsymbol{\phi} \, \mathrm{d}^3x \, \mathrm{d}t \\ &\quad - \int_I \int_V \nabla \cdot \eta \left((\nabla \boldsymbol{\phi}) + (\nabla \boldsymbol{\phi})^T \right) \widetilde{\boldsymbol{u}} \, \mathrm{d}^3x \, \mathrm{d}t \\ &\quad + \int_I \int_V \widetilde{\boldsymbol{u}} \cdot \left(\nabla \cdot \eta \left((\nabla \boldsymbol{\phi}) + (\nabla \boldsymbol{\phi})^T \right) \right) \mathrm{d}^3x \, \mathrm{d}t \end{aligned} \tag{B.29}$$

Utilising the divergence theorem eq. (B.17) once more on the first two expressions on the right hand side

$$\begin{aligned}
&\int_I \int_V \nabla \cdot \eta \left((\nabla \widetilde{\boldsymbol{u}}) + (\nabla \widetilde{\boldsymbol{u}})^T \right) \boldsymbol{\phi} - \nabla \cdot \eta \left((\nabla \boldsymbol{\phi}) + (\nabla \boldsymbol{\phi})^T \right) \widetilde{\boldsymbol{u}} \, \mathrm{d}^3 x \, \mathrm{d}t \\
&= \int_I \int_{\partial V} \eta \left(\left(\nabla \widetilde{\boldsymbol{u}} + (\nabla \widetilde{\boldsymbol{u}})^T \right) \boldsymbol{\phi} \right) \cdot \boldsymbol{n}(x) - \eta \left(\left(\nabla \boldsymbol{\phi} + (\nabla \boldsymbol{\phi})^T \right) \widetilde{\boldsymbol{u}} \right) \cdot \boldsymbol{n}(x) \, \mathrm{d}^2 x \, \mathrm{d}t \\
&= \int_I \int_{\partial V} \eta \left\langle \boldsymbol{\phi}, \left(\nabla \widetilde{\boldsymbol{u}} + (\nabla \widetilde{\boldsymbol{u}})^T \right)^* \boldsymbol{n}(x) \right\rangle - \eta \left\langle \widetilde{\boldsymbol{u}}, \left(\nabla \boldsymbol{\phi} + (\nabla \boldsymbol{\phi})^T \right)^* \boldsymbol{n}(x) \right\rangle \mathrm{d}^2 x \, \mathrm{d}t \\
&= \int_I \int_{\partial V} \eta \boldsymbol{\phi} \cdot \left(\left((\nabla \widetilde{\boldsymbol{u}})^T + \nabla \widetilde{\boldsymbol{u}} \right) \boldsymbol{n}(x) \right) - \eta \widetilde{\boldsymbol{u}} \cdot \left(\left((\nabla \boldsymbol{\phi})^T + \nabla \boldsymbol{\phi} \right) \boldsymbol{n}(x) \right) \mathrm{d}^2 x \, \mathrm{d}t
\end{aligned} \tag{B.30}$$

Now we recall the various boundary conditions placed on the velocity $\boldsymbol{u}$. The zero outflow condition eq. (B.19c) implies the derivative for the radial velocity $\widetilde{\boldsymbol{u}}_r = 0$ for $x \in \partial V$, $t \in I$. On the CMB eq. (B.19b), the free-slip velocity condition, results in $\left(\left(\nabla \widetilde{\boldsymbol{u}} + (\nabla \widetilde{\boldsymbol{u}})^T \right) \boldsymbol{n}(x) \right)_{tan} = 0$ for $x \in C$, $t \in I$. Prescribing plate motion histories as the surface boundary condition eq. (B.19a), makes the derivative $\widetilde{\boldsymbol{u}}_{tan} = 0$ for $x \in S$, $t \in I$.

Taking these simplifications onboard we can now rewrite eq. (B.30) as

$$\begin{aligned}
\int_I \int_S \eta \boldsymbol{\phi} \cdot \left(\left((\nabla \widetilde{\boldsymbol{u}} + \nabla \widetilde{\boldsymbol{u}})^T \right) \boldsymbol{n}(x) \right) \mathrm{d}^2 x \, \mathrm{d}t \\
+ \int_I \int_C \eta \boldsymbol{\phi}_r \left(\left((\nabla \widetilde{\boldsymbol{u}} + \nabla \widetilde{\boldsymbol{u}})^T \right) \boldsymbol{n}(x) \right)_r \mathrm{d}^2 x \, \mathrm{d}t \\
- \int_I \int_C \eta \widetilde{\boldsymbol{u}} \cdot \left(\left((\nabla \boldsymbol{\phi} + \nabla \boldsymbol{\phi})^T \right) \boldsymbol{n}(x) \right) \mathrm{d}^2 x \, \mathrm{d}t \, .
\end{aligned} \tag{B.31}$$

Prescribing boundary conditions to the test function $\boldsymbol{\phi}$ we can force these three surface integrals to vanish. The similarity to the forward equations velocity boundary conditions eqs. (B.19a) to (B.19c) can be thought of as follows;

- $\boldsymbol{\phi}_{tan} = 0$ for $x \in S$, $t \in I$ related to the velocity condition at the surface eq. (B.19a)
- $\left(\left(\nabla \boldsymbol{\phi} + (\nabla \boldsymbol{\phi})^T \right) \boldsymbol{n}(x) \right)_{tan} = 0$ for $x \in C$, $t \in I$ analogous to free slip on the CMB eq. (B.19b)
- $\boldsymbol{\phi}_r = 0$ for $x \in \partial V$, $t \in I$ which parallels to the no-outflow condi-tioneq. (B.19c)

Note also, that the way in which these conditions were determined has the side result that a different choice in boundary conditions (e.g. free-slip/no-slip) for the S or C boundaries, would cause no change in the choice of the $\boldsymbol{\phi}$ boundary conditions.

With these boundary conditions imposed the first term of eq. (B.28) can be simplified to

$$\left\langle \boldsymbol{\phi}, \nabla \cdot \eta \left((\nabla \widetilde{\boldsymbol{u}}) + (\nabla \widetilde{\boldsymbol{u}})^T \right) \right\rangle_{l^2} = \left\langle \widetilde{\boldsymbol{u}}, \nabla \cdot \eta \left((\nabla \boldsymbol{\phi}) + (\nabla \boldsymbol{\phi})^T \right) \right\rangle_{l^2}. \quad \text{(B.32)}$$

The second term of eq. (B.28) contains the pressure term of the momentum equation. This time we apply the vector identity $\nabla \cdot (f\boldsymbol{u}) = f\nabla \cdot \boldsymbol{u} + \boldsymbol{u} \cdot f$ (where $\boldsymbol{u} = \boldsymbol{\phi}$ and $f = \widetilde{P}$) followed by the divergence theorem eq. (B.17) yielding

$$\begin{aligned} \left\langle \boldsymbol{\phi}, \nabla \widetilde{P} \right\rangle_{l^2} &= \int_I \int_V \nabla \cdot (\widetilde{P}\boldsymbol{\phi}) \, \mathrm{d}^3x - \int_I \int_V \widetilde{P} \nabla \cdot \boldsymbol{\phi} \, \mathrm{d}^3x \\ &= \int_I \int_{\partial V} (\widetilde{P}\boldsymbol{\phi}) \cdot \boldsymbol{n}(x) \, \mathrm{d}^2x - \left\langle \widetilde{P}, \nabla \cdot \boldsymbol{\phi} \right\rangle_{L^2}. \end{aligned} \quad \text{(B.33)}$$

Recalling in the previous step the boundary condition $\boldsymbol{\phi}_r = 0$ for $x \in \partial V$, $t \in I$, the surface integral becomes zero and

$$\left\langle \boldsymbol{\phi}, \nabla \widetilde{P} \right\rangle_{l^2} = - \left\langle \widetilde{P}, \nabla \cdot \boldsymbol{\phi} \right\rangle_{L^2}. \quad \text{(B.34)}$$

The final term that must be dealt with in eq. (B.28) is the buoyancy term which contains a total derivate of the temperature $\widetilde{T}$. We can isolate $\widetilde{T}$ by re-expressing the vectorial product l^2 as the scalar product L^2 which gives

$$\left\langle \boldsymbol{\phi}, \alpha\rho\widetilde{T}\boldsymbol{g} \right\rangle_{l^2} = \left\langle \widetilde{T}, \alpha\rho\boldsymbol{g} \cdot \boldsymbol{\phi} \right\rangle_{L^2} \quad \text{(B.35)}$$

which combining with the other terms we can rewrite eq. (B.28) as

$$\left\langle \widetilde{\boldsymbol{u}}, \nabla \cdot \eta \left(\nabla \boldsymbol{\phi} + (\nabla \boldsymbol{\phi})^T \right) \right\rangle_{l^2} + \left\langle \widetilde{P}, \nabla \cdot \boldsymbol{\phi} \right\rangle_{L^2} - \left\langle \widetilde{T}, \alpha\rho\boldsymbol{g} \cdot \boldsymbol{\phi} \right\rangle_{L^2} = 0. \quad \text{(B.36)}$$

B.5.4 The energy equation

Finally for conservation of energy eq. (B.18c) we again take the total derivative;

$$\frac{\partial(\mathcal{D}_{T_0}T)(\Delta T_0)}{\partial t} + (\mathcal{D}_{T_0}\boldsymbol{u})(\Delta T_0)\cdot\nabla T + \boldsymbol{u}\cdot\nabla(\mathcal{D}_{T_0}T)(\Delta T_0) - \kappa\nabla^2(\mathcal{D}_{T_0}T)(\Delta T_0) - \underbrace{(\mathcal{D}_{T_0}H)(\Delta T_0)}_{=0} = 0. \quad \text{(B.37)}$$

Before multiplying through this time by the scalar test function τ and taking the inner product we can eliminate any terms which are independent of the initial temperature T_0; i.e. the internal heating rate H. With this we obtain as the weak formulation for our energy equation

$$\left\langle \tau, \frac{\partial\widetilde{T}}{\partial t}\right\rangle_{L^2} + \langle \tau, \widetilde{\boldsymbol{u}}\cdot\nabla T\rangle_{L^2} + \left\langle \tau, \boldsymbol{u}\cdot\nabla\widetilde{T}\right\rangle_{L^2} - \left\langle \tau, \kappa\nabla^2\widetilde{T}\right\rangle_{L^2} = 0. \quad \text{(B.38)}$$

Once more we look to isolate any terms containing total derivative $\widetilde{\boldsymbol{u}}$ or $\widetilde{T}$, and again we will work left to right through the terms present in eq. (B.38).

By partially integrating our first term we see that

$$\begin{aligned}\left\langle \tau, \frac{\partial\widetilde{T}}{\partial t}\right\rangle_{L^2} &= \int_I\int_V \tau\frac{\partial\widetilde{T}}{\partial t}\,\mathrm{d}^3x\,\mathrm{d}t \\ &= \int_V \left(\tau\widetilde{T}\right)|_{t_0}^{t_1}\mathrm{d}^3x - \int_I\int_V \widetilde{T}\frac{\partial\tau}{\partial t}\,\mathrm{d}^3x\,\mathrm{d}t \\ &= \int_V \left(\underbrace{\tau(x,t_1)\widetilde{T}(x,t_1)}_{\tau(x,t_1)=0} - \tau(x,t_0)\underbrace{\widetilde{T}(x,t_0)}_{=\Delta T_0}\right)\mathrm{d}^3x - \left\langle \widetilde{T}, \frac{\partial\tau}{\partial t}\right\rangle_{L^2}.\end{aligned} \quad \text{(B.39)}$$

The first part of the partially evaluated integral vanishes if we apply the constraint $\tau(x,t_1)=0$ for $x\in V$. In the second term of this integral we note that $\widetilde{T}(x,t_0)$ is the derivative of the temperature in the direction T_0 at t_0 and so is infact our search direction ΔT_0, which leaves us with the following:

$$\left\langle \tau, \frac{\partial\widetilde{T}}{\partial t}\right\rangle_{L^2} = -\int_V \tau(x,t_0)\Delta T_0(x)\,\mathrm{d}^3x - \left\langle \widetilde{T}, \frac{\partial\tau}{\partial t}\right\rangle_{L^2} \quad \text{(B.40)}$$

The second term contains the total derivative of $\boldsymbol{u}, \widetilde{\boldsymbol{u}}$. This is again trivial to isolate by once again re-expressing the scalar product L^2 as the vectorial product l^2 to give

$$\langle \tau, \widetilde{\boldsymbol{u}} \cdot \nabla T \rangle_{L^2} = \langle \widetilde{\boldsymbol{u}}, \tau \nabla T \rangle_{l^2} \,. \tag{B.41}$$

For the third term we make use of the vector identity $f(\nabla g \cdot \boldsymbol{u}) + g(\nabla f \cdot \boldsymbol{u}) = \nabla \cdot (fg\boldsymbol{u}) - fg(\nabla \cdot \boldsymbol{u})$ (with $f = \tau$, $g = \widetilde{T}$ and $\boldsymbol{u} = \boldsymbol{u}$) to expand the term such that

$$\begin{aligned}\left\langle \tau, \boldsymbol{u} \cdot \nabla \widetilde{T} \right\rangle_{L^2} = &\int_I \int_V \nabla \cdot \left(\tau \widetilde{T} \boldsymbol{u} \right) \mathrm{d}^3 x \, \mathrm{d}t \\ &- \int_I \int_V \tau \widetilde{T} \underbrace{(\nabla \cdot \boldsymbol{u})}_{=0} \mathrm{d}^3 x \, \mathrm{d}t - \int_I \int_V \widetilde{T} (\nabla \tau \cdot \boldsymbol{u}) \, \mathrm{d}^3 x \, \mathrm{d}t \,.\end{aligned} \tag{B.42}$$

Since $\nabla \cdot \boldsymbol{u}$ is our conservation of mass we know its value is 0 and so can be eliminated. Furthermore the application of the divergence theorem eq. (B.17) again allows us to simplify the volume integral such that

$$\left\langle \tau, \boldsymbol{u} \cdot \nabla \widetilde{T} \right\rangle_{L^2} = \int_I \int_V \tau \widetilde{T} \underbrace{(\boldsymbol{u} \cdot \boldsymbol{n})}_{=0} \mathrm{d}^2 x \, \mathrm{d}t - \left\langle \widetilde{T}, \boldsymbol{u} \cdot \nabla \tau \right\rangle_{L^2} \,. \tag{B.43}$$

From our no-outflow boundary condition, eq. (B.19c), our surface integral also vanishes leaving only the one term

$$\left\langle \tau, \boldsymbol{u} \cdot \nabla \widetilde{T} \right\rangle_{L^2} = - \left\langle \widetilde{T}, \boldsymbol{u} \cdot \nabla \tau \right\rangle_{L^2} \,. \tag{B.44}$$

The final term in which a total derivative needs to be isolated contains the laplacian, and so we will make use of Green's second identity $\int_V f \nabla^2 g - g \nabla^2 f \, \mathrm{d}V = \int_{\partial V} f \nabla g \cdot \boldsymbol{n} - g \nabla f \cdot \boldsymbol{n} \, \mathrm{d}\partial V$ (where $f = \tau$ and $g = \widetilde{T}$) in order to obtain the following

$$\begin{aligned}\left\langle \tau, \kappa \nabla^2 \widetilde{T} \right\rangle_{L^2} = &\kappa \int_I \int_{\partial V} \underbrace{\tau}_{=0} \left(\nabla \widetilde{T} \cdot \boldsymbol{n} \right) \mathrm{d}^2 x \, \mathrm{d}t \\ &- \kappa \int_I \int_{\partial V} \underbrace{\widetilde{T}}_{=0} (\nabla \tau \cdot \boldsymbol{n}) \, \mathrm{d}^2 x \, \mathrm{d}t + \kappa \int_I \int_V \widetilde{T} \nabla^2 \tau \, \mathrm{d}^3 x \, \mathrm{d}t \,.\end{aligned} \tag{B.45}$$

Since $\nabla \widetilde{T} \cdot \boldsymbol{n}$ is not necessarily zero, by defining the boundary condition $\tau = 0$ for $x \in \partial V$, $t \in I$ the first surface integral is forced to vanish. Secondly since T has fixed boundary conditions, eqs. (B.21a) and (B.21b), the total

derivative $\widetilde{T} = 0$ at the boundaries and the second surface integral also vanishes. This leaves only the final volume integral which we can see has $\widetilde{T}$ isolated as desired, hence

$$\left\langle \tau, \kappa\nabla^2\widetilde{T} \right\rangle_{L^2} = \left\langle \widetilde{T}, \kappa\nabla^2\tau \right\rangle_{L^2}. \tag{B.46}$$

Combining each term we arrive at the following expression:

$$\langle \widetilde{\boldsymbol{u}}, \tau\nabla T\rangle_{l^2} - \int_V \tau(x,t_0)\Delta T_0(x)\,\mathrm{d}^3x - \left\langle \widetilde{T}, \frac{\partial\tau}{\partial t} \right\rangle_{L^2} - \left\langle \widetilde{T}, \boldsymbol{u}\cdot\nabla\tau \right\rangle_{L^2} - \left\langle \widetilde{T}, \kappa\nabla^2\tau \right\rangle_{L^2} = 0. \tag{B.47}$$

B.6 The adjoint equations for incompressible flow

As eqs. (B.26), (B.36) and (B.47) are all homogeneous (i.e. $= 0$) we can add these terms to the total derivative of our misfit function χ (eq. (B.15)) Combining inner products containing the same isolated variable we arrive at:

$$\begin{aligned}\mathcal{D}_{T_0}\chi(T)(\Delta T_0) = &\left\langle \widetilde{P}, \nabla\cdot\boldsymbol{\phi} \right\rangle_{L^2} \\ &+ \left\langle \widetilde{\boldsymbol{u}}, \nabla\cdot(\eta\{\nabla\boldsymbol{\phi} + (\nabla\boldsymbol{\phi})^T\}) - \nabla\psi + \tau\nabla T \right\rangle_{l^2} \\ &+ \left\langle \widetilde{T}, \partial_T\hat{\chi} - \frac{\partial\tau}{\partial t} - \boldsymbol{u}\cdot\nabla\tau - \kappa\nabla^2\tau - \alpha\rho\boldsymbol{g}\cdot\boldsymbol{\phi} \right\rangle_{L^2} \\ &- \int_V \tau(x,t_0)\Delta T_0(x)\,\mathrm{d}^3x.\end{aligned} \tag{B.48}$$

From this we can deduce that the scaler/vector products involving each total derivative $\widetilde{\boldsymbol{u}}$, $\widetilde{P}$, $\widetilde{T}$ will vanish if our test functions $\boldsymbol{\phi}$, ψ, τ satisfy the following equations:

$$\nabla\cdot\boldsymbol{\phi} = 0 \tag{B.49a}$$

$$\nabla\cdot\left(\eta\{\nabla\boldsymbol{\phi} + (\nabla\boldsymbol{\phi})^T\}\right) - \nabla\psi + \tau\nabla T = 0 \tag{B.49b}$$

$$\frac{\partial\tau}{\partial t} + \boldsymbol{u}\cdot\nabla\tau + \kappa\nabla^2\tau + \alpha\rho\boldsymbol{g}\cdot\boldsymbol{\phi} = \frac{\partial\hat{\chi}(T)}{\partial T} \tag{B.49c}$$

where $\partial_T\chi(T) = (T_\mathrm{t} - T_\mathrm{m})\delta(t - t_1)$. We will from here on refer to these as the adjoint equations for incompressible mantle circulation. This set of equations have their own boundary and initial condition as outlined during

the derivations. Collecting these together now we see that

$$\boldsymbol{\phi}_{tan}(x,t) = 0, \quad x \in S, t \in I \tag{B.50a}$$

$$\left(\left(\nabla\boldsymbol{\phi} + (\nabla\boldsymbol{\phi})^T\right) \cdot \boldsymbol{n}(x)\right)_{tan} = 0, \quad x \in C, t \in I \tag{B.50b}$$

$$\boldsymbol{\phi}_r(x,t) = \boldsymbol{\phi}(x,t) \cdot \boldsymbol{n}(x) = 0, \quad x \in \partial V, t \in I \tag{B.50c}$$

$$\psi(x,t) = 0, \quad x \in \partial V, t \in I \tag{B.50d}$$

$$\tau(x,t) = 0, \quad x \in \partial V, t \in I \tag{B.50e}$$

are our boundary conditions, together with the initial condition

$$\tau(x,t_1) = 0, \quad x \in V. \tag{B.51}$$

Once the solutions to the adjoint equations are found, eq. (B.48) is reduced to

$$\mathcal{D}_{T_0}\chi(T)(\Delta T_0) = -\int_V \tau(x,t_0)\Delta T_0(x)\,\mathrm{d}^3x, \tag{B.52}$$

which now only depends on the adjoint temperature at t_0, $\tau(x,t_0)$ and the differentiation direction ΔT_0. For this instance, the appropriate differentiation direction for $y \in V$ is

$$\Delta T_0(x) = \beta\delta(y-x), x \in V, \tag{B.53}$$

where $\beta \in \mathbb{R}$ is a step length determined by a conjugate gradient method (Fletcher and Reeves 1964). It is using the conjugate gradient method that we update our initial condition guess T_0^n using eq. (B.53) to yield the following equation to update our initial condition guess

$$T_0^{n+1}(x) = T_0^n(x) - \beta\tau(x,t_0). \tag{B.54}$$

B.7 The adjoint equations for compressible models

We recall from section 2.2 that if we consider the mantle to be compressible then the equations describing mantle convection are instead

$$\nabla \cdot (\rho \boldsymbol{u}) = 0 \tag{B.55a}$$

$$\nabla \cdot \left(\eta \left\{ \nabla \boldsymbol{u} + (\nabla \boldsymbol{u})^T - \frac{2}{3} \mathbb{I} (\nabla \cdot \boldsymbol{u}) \right\} \right) - \nabla P + \Delta \rho \boldsymbol{g} = 0 \tag{B.55b}$$

$$\frac{\partial T}{\partial t} + \boldsymbol{u} \cdot \nabla T + \gamma T \nabla \cdot \boldsymbol{u} - \frac{1}{\rho c_V} (\bar{\tau} : \nabla \boldsymbol{u} + \nabla \cdot (k \nabla T)) + H = 0. \tag{B.55c}$$

where $\bar{\tau}$ is the deviatoric stress given by

$$\bar{\tau} = \eta \left\{ \nabla \boldsymbol{u} + (\nabla \boldsymbol{u})^T - \frac{2}{3} \mathbb{I} (\nabla \cdot \boldsymbol{u}) \right\}.$$

Since this is a different set of equations than the incompressible case just presented, a new derivation is required here. Ghelichkhan and Bunge (2016) use the same method of derivation by operator formulations in Hilbert spaces as used for the incompressible equations, and obtain the following set of equations which describe the adjoint equations for compressible mantle flow.

$$\nabla \cdot \boldsymbol{\phi} = 0 \tag{B.56a}$$

$$\nabla \cdot \left(\eta \{ \nabla \boldsymbol{\phi} + (\nabla \boldsymbol{\phi})^T \} \right) - \rho_r \nabla \psi + \tau \nabla T - 2 \nabla \cdot \left(\frac{\tau}{\rho_r c_v} \bar{\tau} \right) = 0 \tag{B.56b}$$

$$\frac{\partial \tau}{\partial t} + \boldsymbol{u} \cdot \nabla \tau - (\gamma - 1) \tau \nabla \cdot \boldsymbol{u} + \nabla \cdot \left(k \nabla \left(\frac{\tau}{\rho_r c_v} \right) \right) + \alpha \rho \boldsymbol{g} \cdot \boldsymbol{\phi} = \frac{\partial \hat{\chi}(T)}{\partial T} \tag{B.56c}$$

and their corresponding boundary conditions

$$\boldsymbol{\phi}_{tan}(x,t) = 0, \quad x \in S, t \in I \tag{B.57a}$$

$$\left(\left(\nabla\boldsymbol{\phi} + (\nabla\boldsymbol{\phi})^T\right) \cdot \boldsymbol{n}(x)\right)_{tan} = 0, \quad x \in C, t \in I \tag{B.57b}$$

$$\boldsymbol{\phi}(x,t) \cdot \boldsymbol{n}(x) = 0, \quad x \in \partial V, t \in I \tag{B.57c}$$

$$\psi(x,t) = 0, \quad x \in \partial V, t \in I \tag{B.57d}$$

$$\tau(x,t) = 0, \quad x \in \partial V, t \in I \tag{B.57e}$$

and initial condition

$$\tau(x,t_1) = 0, \quad x \in V. \tag{B.58}$$

The presence of the term $(\gamma - 1)$ in eq. (B.56c), effectively the adjoint compressibility term, is minimal as γ is typically taken $\mathcal{O}(1)$. Because of this using compressible or incompressible adjoint equations with a compressible forward model yields very similar results. Therefore it is not necessary to use the compressible adjoint equations.

B.8 Thoughts on the adjoint equations for thermochemical models

The equations outlining a thermochemical model vary from a purely thermal model as follows;

$$\nabla \cdot \boldsymbol{u} = 0 \tag{B.59a}$$

$$\nabla \cdot \left(\eta\{\nabla\boldsymbol{u} + (\nabla\boldsymbol{u})^T\}\right) - \nabla P + \alpha\rho(T_{av} - T)\boldsymbol{g} + \Delta\rho C\boldsymbol{g} = 0 \tag{B.59b}$$

$$\frac{\partial T}{\partial t} + \boldsymbol{u} \cdot \nabla T - \kappa\nabla^2 T + H = 0 \tag{B.59c}$$

$$\frac{\partial C}{\partial t} + \boldsymbol{u} \cdot \nabla C = 0. \tag{B.59d}$$

Here C represents composition and $\Delta\rho$ is the density difference between the light ($C = 0$) and dense ($C = 1$) material with boundary conditions for the

velocity $\boldsymbol{u}$

$$\boldsymbol{u}(x,t)\cdot\boldsymbol{n}(x)=0, \quad x\in\partial V, t\in I \tag{B.60}$$
$$\nabla\boldsymbol{u}(x,t)\cdot\boldsymbol{n}(x)=0, \quad x\in C, t\in I \tag{B.61}$$
$$\boldsymbol{u}(x,t)=u_P(x,t), \quad x\in S, t\in I \tag{B.62}$$

and temperature T

$$T(x,t)=T_S, \quad x\in S, t\in I \tag{B.63}$$
$$T(x,t)=T_C, \quad x\in C, t\in I \tag{B.64}$$

with initial conditions

$$T(x,t_0)=T_0(x), \quad x\in V. \tag{B.65}$$
$$C(x,t_0)=C_0(x), \quad x\in V. \tag{B.66}$$

Boundary conditions on C are not immediately obvious, as unlike the temperature field where we presume our boundary conditions are perfect, we would hope to use the adjoint method to improve our estimate of C which varies over the CMB boundary. Because of this we cannot perform the same simplifications as seen in the previous derivations. Furthermore, we see that eq. (B.59d) is also time-dependent like the heat equation (eq. (B.59c)). This introduces an extra complexity with additional assumptions needed. The implications of the boundary conditions for C is that a more complete reevaluation of the adjoint derivation is required.